

**INTEGRAL ACCURACY AND THE STABILITY OF TIME DOMAIN  
INTEGRAL EQUATIONS FOR ELECTROMAGNETIC SCATTERING**

by

Jielin Li

A dissertation submitted to the Faculty of the University of Delaware in partial fulfillment of the requirements for the degree of Doctor of Philosophy in Electrical and Computer Engineering

Fall 2018

© 2018 Jielin Li  
All Rights Reserved

INTEGRAL ACCURACY AND THE STABILITY OF TIME DOMAIN  
INTEGRAL EQUATIONS FOR ELECTROMAGNETIC SCATTERING

by

Jielin Li

Approved: \_\_\_\_\_  
Kenneth E. Barner, Ph.D.  
Chair of the Department of Electrical and Computer Engineering

Approved: \_\_\_\_\_  
Levi T. Thompson, Ph.D.  
Dean of the College of Engineering

Approved: \_\_\_\_\_  
Douglas J. Doren, Ph.D.  
Interim Vice Provost for Graduate and Professional Education

I certify that I have read this dissertation and that in my opinion it meets the academic and professional standard required by the University as a dissertation for the degree of Doctor of Philosophy.

Signed: \_\_\_\_\_  
Daniel S. Weile, Ph.D.  
Professor in charge of dissertation

I certify that I have read this dissertation and that in my opinion it meets the academic and professional standard required by the University as a dissertation for the degree of Doctor of Philosophy.

Signed: \_\_\_\_\_  
Keith W. Goossen, Ph.D.  
Member of dissertation committee

I certify that I have read this dissertation and that in my opinion it meets the academic and professional standard required by the University as a dissertation for the degree of Doctor of Philosophy.

Signed: \_\_\_\_\_  
Mark S. Mirotznik, Ph.D.  
Member of dissertation committee

I certify that I have read this dissertation and that in my opinion it meets the academic and professional standard required by the University as a dissertation for the degree of Doctor of Philosophy.

Signed: \_\_\_\_\_  
Peter B. Monk, Ph.D.  
Member of dissertation committee

I certify that I have read this dissertation and that in my opinion it meets the academic and professional standard required by the University as a dissertation for the degree of Doctor of Philosophy.

Signed: \_\_\_\_\_

Tobin A. Driscoll, Ph.D.

Member of dissertation committee

## **ACKNOWLEDGEMENTS**

I wish to thank all of the people who helped me during my Ph.D. study in U.S., especially my adviser, Prof. Daniel Weile, and my research groupmates David Hopkins and Chris Kerwien. I must also thank my parents in China, without whom none of this would ever have been possible.

## TABLE OF CONTENTS

<b>LIST OF TABLES</b> . . . . .	<b>viii</b>
<b>LIST OF FIGURES</b> . . . . .	<b>ix</b>
<b>ABSTRACT</b> . . . . .	<b>xiii</b>
 <b>Chapter</b>	
<b>1 INTRODUCTION</b> . . . . .	<b>1</b>
1.1 Background . . . . .	1
1.1.1 Why Use Time Domain Integral Equation Approaches . . . . .	1
1.1.2 The Development of Time Domain Integral Equation Techniques . . . . .	7
1.1.3 The Main Problems of Time Domain Integral Equation Solvers . . . . .	10
1.2 Purpose and Method . . . . .	13
<b>2 FORMULATION</b> . . . . .	<b>15</b>
2.1 Time Domain Integral Equations . . . . .	15
2.1.1 Maxwell Equations . . . . .	15
2.1.2 Auxiliary Potentials . . . . .	18
2.1.3 Green Function Solutions . . . . .	19
2.1.4 Formulation of Time Domain Integral Equations . . . . .	20
2.2 Spatial Discretization . . . . .	25
2.2.1 Method of Moments . . . . .	25
2.2.2 Spatial Basis Functions . . . . .	28
2.3 Temporal Discretization . . . . .	35
2.3.1 Convolution Quadrature Method . . . . .	36

2.3.2	Bandlimited Interpolation Function Method . . . . .	47
2.4	Other Related Numerical Algorithms . . . . .	50
2.4.1	Gaussian Quadrature for One Dimension . . . . .	50
2.4.2	Gaussian Quadrature for Triangles . . . . .	52
2.4.3	Duffy Transform . . . . .	54
2.4.4	Adaptive Integral Method . . . . .	55
2.4.5	Adaptive Quadrature . . . . .	57
<b>3</b>	<b>TDIE STABILITY COMPUTATIONS FOR PEC SCATTERERS</b>	<b>60</b>
3.1	Ogive . . . . .	61
3.2	NASA Almond . . . . .	62
3.3	Tank . . . . .	63
3.4	Sphere . . . . .	64
3.5	Flat Square . . . . .	65
<b>4</b>	<b>TDIE STABILITY COMPUTATIONS FOR DIELECTRIC SCATTERERS</b>	<b>81</b>
4.1	Ogive . . . . .	82
4.2	Dielectric Sphere . . . . .	83
4.3	Dielectric Sphere with Conductor Core . . . . .	84
<b>5</b>	<b>CONCLUSION</b>	<b>91</b>
	<b>BIBLIOGRAPHY</b>	<b>92</b>

## LIST OF FIGURES

1.1	A partially illuminated patch . . . . .	11
2.1	A classic scattering problem. . . . .	20
2.2	A classic scattering problem for PEC. . . . .	24
2.3	Edge vectors on a triangle. . . . .	31
2.4	Interpolating nodes with a triangle for bases in which $s = 2$ and $\beta = 1$ . . . . .	32
2.5	A zeroth-order divergence-conforming vector functions associated with the hypotenuse. . . . .	33
2.6	A zeroth-order GWP basis functions associated with the horizontal side. . . . .	34
2.7	A zeroth-order GWP basis functions associated with the vertical side. . . . .	35
2.8	A first-order GWP basis function interpolating a node on the bottom edge. . . . .	36
2.9	A first-order GWP basis function interpolating a node on the bottom edge. . . . .	37
2.10	A first-order GWP basis function interpolating a node on the right edge. . . . .	38
2.11	A first-order GWP basis function interpolating a node on the right edge. . . . .	39
2.12	A first-order GWP basis function interpolating a node on the left edge. . . . .	40

2.13	A first-order GWP basis function interpolating a node on the left edge. . . . .	41
2.14	A first-order GWP basis function interpolating a node within a triangle. . . . .	42
2.15	A first-order GWP basis function interpolating a node within a triangle. . . . .	43
2.16	Structure of the time domain AIM operator. . . . .	58
2.17	A triangle division scheme. . . . .	59
3.1	A perfectly conducting ogive. . . . .	66
3.2	Late time current behavior of a stable simulation. . . . .	67
3.3	Late time current behavior of an unstable simulation. . . . .	68
3.4	Bistatic RCS of the ogive computed at (a) 200MHz, (b) 220MHz, and (c) 240MHz, and (d) the monostatic RCS between 200 and 240 MHz. . . . .	69
3.5	Stability of the simulation versus integration accuracy for a perfect conducting ogive for CQ. . . . .	70
3.6	Stability of the simulation versus integration accuracy for a perfect conduction ogive for BLIF. . . . .	70
3.7	A NASA almond. . . . .	71
3.8	Comparison of RCS results. Subfigures (a), (b) and (c) show the bistatic RCS results at the lowest frequency, center frequency, and highest frequency in the range. Subfigure (d) shows the monostatic RCS obtained at elevation angle $\theta = 0$ . . . . .	72
3.9	Stability of the simulation versus integration accuracy for a perfect conducting NASA almond for CQ. . . . .	73
3.10	Stability of the simulation versus integration accuracy for a perfect conducting NASA almond for BLIF. . . . .	73
3.11	A perfectly conducting scatterer approximating a tank. . . . .	74

3.12	Bistatic RCS of the tank computed at (a) 100MHz, (b) 120MHz, and (c) 140MHz, and (d) the monostatic RCS between 200 and 240 MHz.	75
3.13	Stability of the simulation versus integration accuracy for a perfect conducting tank for CQ.	76
3.14	Stability of the simulation versus integration accuracy for a perfect conducting tank for BLIF.	76
3.15	Comparison of RCS results of a sphere. The bistatic RCS results at start point, middle point and the end point of the frequency range are shown in (a), (b) and (c). The monostatic RCS vs. frequency at elevation angle $\theta = 0$ is shown in (d).	77
3.16	Stability of the simulation versus integration accuracy for a perfect conducting sphere for CQ.	78
3.17	Stability of the simulation versus integration accuracy for a perfect conducting sphere for BLIF.	78
3.18	Comparison of RCS results. The bistatic RCS results at start point, middle point and the end point of the frequency range are shown in (a), (b) and (c). The monostatic RCS vs. frequency at elevation angle $\theta = 0$ is shown in (d).	79
3.19	Stability of the simulation versus integration accuracy for a perfect conducting square for CQ.	80
3.20	Stability of the simulation versus integration accuracy for a perfect conducting square for BLIF.	80
4.1	Stability of the simulation versus integration accuracy for a dielectric ogive for CQ.	82
4.2	Stability of the simulation versus integration accuracy for a dielectric ogive for BLIF.	83
4.3	Comparison of RCS results for a dielectric ogive. The bistatic RCS results at start point, middle point and the end point of the frequency range are shown in (a), (b) and (c). The monostatic RCS vs. frequency at elevation angle $\theta = 0$ is shown in (d).	86

4.4	Comparison of RCS results of a dielectric sphere. The bistatic RCS results at start point, middle point and the end point of the frequency range are shown in (a), (b) and (c). The monostatic RCS vs. frequency at elevation angle $\theta = 0$ is shown in (d). . . . .	87
4.5	Stability of the simulation versus integration accuracy for a homogeneous dielectric sphere for CQ. . . . .	88
4.6	Stability of the simulation versus integration accuracy for a homogeneous dielectric sphere for BLIF. . . . .	88
4.7	Comparison of RCS results of a dielectric sphere with a conductor core. The bistatic RCS results at start point, middle point and the end point of the frequency range are shown in (a), (b) and (c). The monostatic RCS vs. frequency at elevation angle $\theta = 0$ is shown in (d). . . . .	89
4.8	Stability of the simulation versus integration accuracy for a dielectric sphere with a perfect conducting core for CQ. . . . .	90
4.9	Stability of the simulation versus integration accuracy for a dielectric sphere with a perfect conducting core for BLIF. . . . .	90

## ABSTRACT

Stability of time domain integral equation approaches to the computation of electromagnetic scattering is profoundly affected by the accuracy of the underlying numerical integration methods used for computation of the kernel elements. In most publications, numerical integrals are assumed exact and higher integral orders are assumed to deliver higher accuracy. The lack of attention to this detail has led to inaccurate conclusions about the stability of different solution methods. In this work, we examine the complicated relationship between the actual accuracy of integral computation and the resulting stability of integral equations. Numerical results show that numerical integrals are not as exact as expected, and that stability may be improved for a higher integral accuracy. Moreover, while integral accuracy is not always improved by higher order integration rules, more careful integration (as delivered by adaptive integration methods) is often helpful. Numerical results for a range of problems demonstrate these contentions.

# Chapter 1

## INTRODUCTION

Time domain integral equation (TDIE) solvers are indispensable to the computational electromagnetics (CEM) community and to the community of electromagnetic device designers who use their products. TDIE methods have important potential applications in ensuring electromagnetic compatibility in the design of consumer goods, and in determining the radar cross sections of objects in motion. Despite these applications, and the urgency of the work, TDIE stability remains only partially understood, and TDIEs remain without commercial implementation. This thesis aims to thoroughly understand one important factor contributing to this state of affairs.

In this chapter, we will review the background of this work, explain its meaning and purpose, as well as the methods the community has developed for the numerical discretization of TDIEs. Section 1.1 discusses the development of TDIE solvers and some problems they have. Section 1.2 describes the meaning, the purpose and the methods of this research.

### 1.1 Background

#### 1.1.1 Why Use Time Domain Integral Equation Approaches

Since Guglielmo Marconi's successful radio work, modern society has become more reliant on the use of electromagnetic fields. The development of our material life is driven by our ubiquitous electromagnetic systems. From satellite communication systems and radars to cellphones and microwave ovens, electromagnetic devices and our daily life are tightly interweaved.

Despite the fact that the Maxwell Equations, which govern the world of electromagnetics, were established as early as 1864, their analytical solutions in closed form are known only for a few cases of highly regular shapes. The applications of the Maxwell equations in engineering practice, such as electromagnetic scattering, antenna radiation and waveguide design, always involve arbitrary geometry structures. Since these problems could not be solved analytically, people immediately started researching approximate solutions to deal with real-world problems more than a century ago. One well-known example is the use of the method of moments (MoM) to solve Pocklington's integral equation for the radiation from thin wire antennas [38].

With the advent of modern computer technology, people began studying the use of more efficient computational methods to numerically solve electromagnetic problems, which gave rise to a multi-disciplinary field of study called computational electromagnetics (CEM). Researchers in the CEM community employ the knowledge of electromagnetics, mathematics, and computer science, to develop computer-based electromagnetic solvers. By adapting computationally efficient approximations, it is possible for those solvers to solve arbitrary electromagnetic problems by computing the electrical fields and magnetic fields across a problem domain, or by finding electric and magnetic currents in inhomogeneities and on boundaries. They are able to calculate antenna radiation patterns for given antenna structures, the radar cross section (RCS) of almost any object, and the normal modes of waveguides. Such abilities make CEM solvers crucial to contemporary electrical engineering.

Although like all physical laws, the Maxwell Equations were proposed first in time domain, they can also be written in the frequency domain by assuming time harmonic behavior [2]. Based on this distinction, electromagnetic solvers can be classified into two domains: the time domain and the frequency domain.

In each domain, the solution of the Maxwell Equations be reduced to the solution of an integral or differential equation or a set of equations. Note that the equation solved may not be the Maxwell Equations themselves, but some other equivalent formulation derived from the Maxwell equations. Some differential equation methods

are based on the hyperbolic partial differential equations obtained on combining the Maxwell Curl Equations. Integral equations are formulated using the Green's function method applied to these hyperbolic partial differential equations [2]. Hence in both time domain and frequency domains, electromagnetic solvers can further be categorized into two types: differential equation based ones and integral equation based ones. Differential equation based solvers use numerical methods to solve either the differential form Maxwell Equations themselves, or the hyperbolic partial differential equations derived from them involving only or electric fields and magnetic fields. Integral equation based solvers solve for currents by using a formal inverse of the operator appearing in the single variable differential equation formulation. In summary, electromagnetic solvers can be classified into four distinct types, based on domain and equation type: frequency domain differential equation, frequency domain integral equation, time domain differential equation and time domain.

In the early phase of the development of CEM, most of the research took place in frequency domain so that time dependence could be eliminated as an unknown, thus reducing the dimensionality of the unknown. The boundary element method (BEM), which is usually called the method of moments (MoM) in the CEM community, was introduced to solve integral equations for the currents on, and hence radiation from, thin wire antennas. Roger Harrington popularized the MoM with his book in 1968 [21]. Since then, a lot of effort has been made to develop efficient and accurate frequency domain integral equation (FDIE) based solvers using the MoM. FDIE solvers solve dense matrix equations in the frequency domain to compute the equivalent electric and magnetic current sources on the boundaries between homogeneous regions, or throughout inhomogeneous regions. In other words, the equivalence principle requires only surface discretization for homogeneous objects, further reducing the dimensionality of the unknown. Note that when inhomogeneous materials are involved, these solvers will face computational disadvantages, as they give up their surface-based formulation. Another obvious benefit of FDIE formulations is that the radiation condition is automatically

imposed, so implementations do not need to cut off the simulation domain with carefully implemented numerical boundary conditions [18] [37]. These features make FDIE solvers better for radiation and scattering problems.

The finite element method (FEM) was introduced to computational science even before the BEM, to solve frequency domain partial differential equations. Before its (rather late) introduction to CEM, FEM was already used to solve complex elasticity and structural analysis problems in civil and aeronautical engineering in 1940s [23]. Although the FEM based frequency domain differential equation solvers still need to solve matrix equations to compute the electrical and magnetic fields, the matrices are sparse, which means less memory is required and iterative methods can be used efficiently with ease. FEM is also very effective when inhomogeneous materials are involved, since the sparsity of its formulation is unaffected. But for most problems involving large swaths of homogeneous materials, the spatial discretization of the whole problem domain makes it less effective than the MoM. Besides, the boundary of simulation region also needs to be explicitly modeled with properly implemented boundary conditions. These properties are especially undesirable when an electrically large homogeneous object is involved [25] [37]. Based on these features, FEM based solvers are better for closed region problems such as microwave circuit simulation, or highly inhomogeneous problems, as would be encountered in biological simulation. MoM and FEM are the two most widely used methods today for CEM in the frequency domain.

Although frequency domain solvers have seen success in a lot of places, the increasing use of broadband signals, such as short pulses used in digital communication systems, in the 1960s brought clear difficulties to them [27] [33]. To get the broadband frequency response, the frequency domain simulation needs to compute the behavior of the system at enough frequency points to cover the band, which may cost a tremendous amount of computational resources and time. On top of this problem which is not actually prohibitive, non-linear and time-varying systems disallow spatial superposition, creating even greater difficulties [6].

To cope with these problems, researchers turned to time domain solvers. Contrary to frequency domain solvers, time domain solvers can return broadband information in one simulation, and are very good at dealing with time-varying and nonlinear problems [6]. The finite-difference time-domain (FDTD) method was proposed by Yee in 1967 [65]; it uses a finite difference technique to solve the time domain differential Maxwell Equations. The traditional FDTD scheme is very easy to implement and doesn't need to solve any matrix equations. Yet the explicit finite difference technique upon which FDTD is based brings the stability problem. To achieve stability, FDTD must meet a stability condition in which the size of the time step is proscribed by the size of the spatial grid. When simulating scattering from large objects with intricate substructure, the very small spatial intervals resulting from discretization in both time and space will require a lot of computation. The FDTD discretization scheme in time and space also causes dispersion and anisotropy. Moreover, as in the case of FEM, the simulation region in FDTD also needs to be cut off artificially with proper numerical boundary conditions, which also introduces more errors [17] [37].

Many of these difficulties can be alleviated, but not without fundamentally altering the properties that made FDTD so popular. As one example, consider ADI-FDTD [35]. It achieves unconditional stability, but only by introducing the solution of (admittedly sparse) matrix equations. Other important improvements in FDTD include non-uniform grid schemes [34] and higher order FDTD [53]. Any implementation of these inevitably achieves these appealing features at the cost of losing others. In any case, today, FDTD based solvers have been among the most popular time domain solvers.

Though MoM, FEM, and FDTD methods are unquestionably the most popular CEM schemes deployed today, other schemes are occasionally quite useful and bear mentioning here. When the objects are extremely electrically large, ray-optics and edge diffraction based approximation methods are often used, such as geometrical theory of diffraction method [26], physical optics method [2], physical theory of diffraction method [55] and shooting and bouncing ray method [8].

FEM and MoM have also been deployed in the time domain for various reasons [31] [1]. Time domain FEM based solvers combine the advantages of FEM and time domain methods. They are a good choice where inhomogeneous materials and broadband simulations are involved. Unfortunately, efficient boundary conditions for time domain FEM are hard to implement, so some people have developed FEM-FDTD hybrid solvers. For a scattering problem, a FEM-FDTD hybrid solver would divide the computational domain into two parts: a relatively small part in the vicinity of the scatterer's boundary to be treated by the FEM, and the remaining region to be treated by FDTD [47].

Time domain MoM based solvers use the MoM to solve time domain integral equations (TDIEs). Compared with FDTD based and time domain FEM based solvers, they have the following advantages:

1. Higher accuracy. In TDIEs, the time domain Green's function accurately and directly represents the interaction between a source point and an observation point [2]. In FDTD and time domain FEM, the interaction between a source point and an observation point separated by a large distance is negotiated through the step-by-step propagation of the wave through the grid. Because of grid dispersion and anisotropy, greater distance means more errors [17] [25]. TDIE solvers do not suffer from dispersion and anisotropy, since the time lag of interaction is computed directly for every interaction. In general, TDIE solvers have higher accuracy than time domain FEM based solvers, and time domain FEM based solvers have higher accuracy than FDTD solvers.
2. More efficiency for homogeneous materials. For time domain MoM based solvers, only surface discretization is required for homogeneous objects [18] [37]. FDTD solvers and time domain FEM based solvers need to discretize the whole problem domain. For radiation and scattering problems, FEM and FDTD generally need volumetric discretization not only of the scatterer, but a buffer around the scatterer to ease the implementation of artificial boundary conditions [17] [25] [37] [25].

This will add more spatial unknowns and lower the efficiency, especially when the object is electrically large. Although both time domain MoM and time domain FEM need to solve matrix equation systems, most implementation schemes for these methods result in the inversion of sparse matrices.

3. Radiation condition automatically imposed [18] [37]. On the contrary, both FDTD and FETD must carefully impose the proper artificial boundary conditions [17] [25] [37].

In short, TDIE solvers are the best choice for radiation and scattering problems when a time domain method is required. Unfortunately, developing useful TDIE solution schemes has been difficult, historically.

### 1.1.2 The Development of Time Domain Integral Equation Techniques

As mentioned above, real world challenges such as short pulse radar design for high-resolution target identification problems made researchers turn to TDIE solvers. Researches show electromagnetic impulse response could be used to characterize a radar target. It is related to the geometry of a scatter and can be used to compute the response to any transient incident wave by a convolution [27]. As early as the 1960s, some researchers already studied the scattering from electromagnetic pulse using TDIE methods [63] [45] [4]. To solve the convolution in time domain, marching-on-in-time (MoT) method was proposed [3] [51]. Today, most of TDIE solvers still use MoT to solve the convolution in time domain.

From the 1970s to the 1980s, some primitive TDIE-based methods were developed to analysis radiation and scattering problems of wires [33], open surfaces [5] and relatively simple closed objects [7] [24]. Despite their relative success, none of them got widely adaptation due to the constraints of computer technologies and stability difficulties. During that time, due to the availability of circuit solvers, people tried to use the approximate circuit models representing the original electromagnetic problem as a method for the solution of low frequency problems. One example is the partial element equivalent circuit (PEEC) method developed by A. Ruehli at IBM [46].

In 1991, S. M. Rao and D. R. Wilton published their work using an MoM-like approach for the solution of TDIEs [43]. They chose the divergence conforming Rao-Wilton-Glisson (RWG) functions as spatial basis functions, and triangle (chapeau) functions as temporal basis functions to compute the scattering from conducting objects modeled by triangular patches. Prior to that, temporal basis functions had not been explicitly used in the research. The discretization resulted in an equation system which could be solved by MoT method. Meanwhile, the late time instability also got attention from researchers. Some criterions were proposed to reduce the accumulation of discretization errors in the course of MoT [54] [49] [48]. In 1992, D. A. Vechinski and S. M. Rao proposed to eliminate the late-time oscillations by a simple time averaging procedure [56]. In 1993, A. Sadigh and E. Arvas developed a finite impulse response (FIR) filter with a constant group delay during the course of MoT to stabilize the TDIE solvers [50]. Despite their relative success, the filter-like methods provided very limited improvement to the stability, especially in electrically large objects. In 1993, S. M. Rao and T. K. Sarkar proposed an improved method which used the undifferentiated TDIEs for arbitrary shaped conductors [42]. Still using the RWG spatial basis and triangle temporal basis, the typical “expansion” and “testing” processes in MoM were applied. The integral over time representing the collection of charge due to an influx of current was first introduced in their work since they used the undifferentiated TDIEs.

These early works in 1990s marked the beginning of the adoption of TDIE solvers as practical electromagnetic analysis tools. They also revealed the two largest obstacles that slowed the widespread adoption of TDIE solvers: computational complexity and instability.

Since then, researchers have devoted themselves to developing TDIE solvers which can be fast and stable. In 1996, P. J. Davies found that the late time instability may be caused by the unstable modes rising from the expansion of currents by basis [13]. In 1997, G. Manara, A. Monorchio, and R. Reggiannini introduced a heuristic criterion to determine the time sampling step size for triangle patches [32]. Since the early time

information corresponds to the high frequency information and the late time information corresponds to the low frequency information, in 1999, M. M. Rao and T. K. Sarkar proposed using early time and low-frequency-domain response data to reproduce the missing response information [41].

In 2002, S. P. Walker, M. J. Bluck, and I. Chatzis published their work on stability analysis [57]. They suggested that the long term stability is determined by the eigenvalues of the matrices computed through a temporal Fourier transform of the kernel. Other research on temporal basis functions also revealed the importance of the computation of the kernel elements in the matrices to achieve stability. In 2002, Y. S. Chung and T. K. Sarkar first used full domain functions to solve TDIEs [11]. The full domain basis functions they use are weighted Laguerre polynomials, which are orthogonal and vanish at infinite time. To avoid using full domain functions, in 2004, D. S. Weile, *et al.* proposed the bandlimited interpolation function (BLIF) method, which uses very smooth basis functions to achieve an accurate and stable solution [60]. Their scheme combined approximate prolate spheroidal wave functions (APSWFs) and loop-tree decomposition. Since the temporal basis functions are not casual, an extrapolation technique is applied. This brings extra computation, as well as possible computational errors. Besides, the choice for the length of time steps must be chosen very carefully. To compute the kernel elements more accurately, T. Ha-Duong developed an “exact” method based on the analytical computation of almost all of the integrals required for the computation of kernel elements in 2003 [20]. It constructs the TDIEs in a variational formulation and then does the “exact” computation of kernel elements, but is limited to flat patch models [20]. In 2008, X. B. Wang, R. A. Wildman, D. S. Weile, and P. Monk proposed the convolution quadrature (CQ) method that relies on transform domain formulations to avoid temporal basis functions [59]. Finally, in 2012, A. J. Pray, N. V. Nair, and B. Shanker proposed a series expansion method [39]. In this method, for a better computation of the kernel element, the spatial integral is performed by first expanding the field radiated to the testing patch in a series of functions with support in space larger than the patch.

Progress was also made in the development of fast methods. These are discussed only briefly here, as this thesis does not concern itself with fast method development. In 1999, inspired by the fast multipole method (FMM) and the multi-level fast multiple algorithm (MLFMA) in frequency domain, A. A. Ergin, B. Shanker, and E. Michielssen developed the plane wave time-domain (PWTD) method [16]. PWTD reduces the computational complexity of traditional MoT from  $O(N_t N_s^2)$  to  $O(N_t N_s \log(N_s N_t))$ , where  $N_t$  represents time steps and  $N_s$  represents spatial unknowns. Later, based on the frequency domain AIM method, a conjugate gradient FFT-like method, time domain AIM (TD-AIM), were also proposed [66]. Over the last decades, a lot of work has been done to stabilize and accelerate the TDIE solvers. The state of the art of the research on TDIE solvers can make them widely applicable to a range of electromagnetic simulations.

### 1.1.3 The Main Problems of Time Domain Integral Equation Solvers

From its beginning, research on TDIE solvers has focused on its two most important obstacles: the lack of fast methods to make their application practical, and stabilizations to ensure they render usable results in the first place. Phenomenal progress has been made by researchers over recent decades in the development of fast methods. On the other hand, due to this and the relative importance and difficulty of the stability problem, this thesis concentrates on stability.

Compared with the development in fast methods, the progress in stability analysis has been slow. Historically, researchers implementing TDIE-based numerical methods have had difficulty finding the source of the instabilities that plagued their simulations. The byzantine nature of computer programs for the numerical simulation of electromagnetic phenomena makes it difficult to locate the precise causes of any mysterious behavior they exhibit. Because the causes of instability were unexplained, researchers looked merely to mitigate instability, for instance, by filtering out unstable modes. Unfortunately, rather than eliminating the instability, filtering techniques just delayed its onset. While later work has shed a great deal more light on the instability,

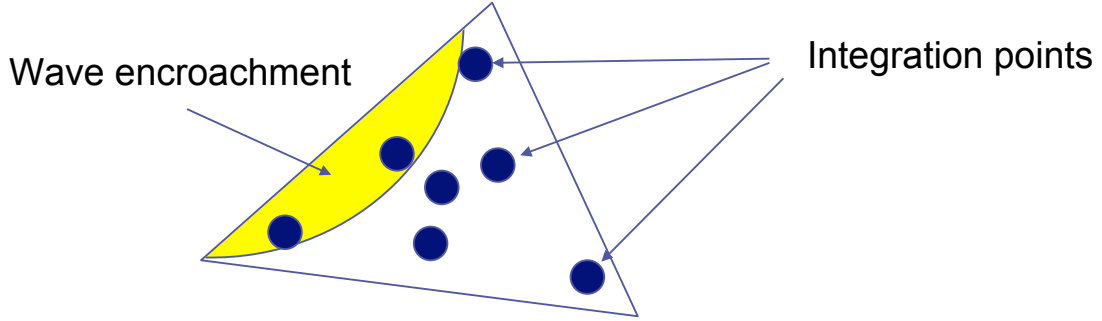


**Figure 1.1:** A partially illuminated patch

results are implementation dependent and hence still imperfectly understood.

Despite its obvious potential effect on the stability, the influence of numerical integration accuracy on the accuracy and stability of the overall method has never been deeply investigated. In fact, the so called “shadow region” issue, one important factor directly contributing to the instability, is deeply rooted in this oversight.

When the MoM is applied to solve TDIEs, a patch-wise testing process is often used to compute the kernel elements. To integrate the field received by a testing patch due to radiation from another patch, early implementations integrated over the whole testing patch with numerical quadratures designed for functions with support over the entire testing patch. This seemingly straightforward approach is complicated by the realization that in TDIE simulation, continuous time is necessarily discretized into many time steps. This leads to a partially illuminated patch at a given time step, as shown in Fig. 1.1. The discontinuity in the field (or its derivatives) frustrates standard integration schemes and leads to inaccurate kernel entries.

Several schemes widely used now have been developed to overcome this issue as mentioned in last subsection. The “exact” method finds these shadow areas exactly [20]. The key to this exact computation of kernel elements is to determining the topology of the domain of integration. For example, to test the field received by a triangular patch due to a point source when the time is piecewise continuous, one has to find the corresponding domains in the triangle where the integrands are piecewise

continuous. While this method seems stable in all cases studied, its application is limited to flat patches.

The full domain function method, as proposed by Y.S. Chung and T.K. Sarkar [11] in 2002, chooses weighted Laguerre polynomials as full domain temporal basis functions. The weighting functions are chosen as weighted Laguerre polynomials of different orders because they are orthogonal. The unknown currents are expanded into a set of weighted Laguerre polynomials of different orders combined with unknown coefficients. Because the recursive relation between the different orders for the weighted Laguerre polynomials, this temporal discretization scheme leads to a system of marching-on-in-degree (MoD) of the Laguerre polynomials, instead of a MoT system. The use of full domain temporal basis functions enhances the late time stability but requires high memory consumption, since it also leads to dense matrices, compared with the sparse matrices from MoT. Because of this, the computational complexity of this scheme is  $O(N_s^2 N_t^2)$ , compared to  $O(N_s^2 N_t)$  for MoT schemes.

The CQ method mentioned in last subsection, starts with the Laplace domain form of the TDIE in question, without introducing temporal basis functions, and uses the finite difference approximation in Z-domain and inverse Z-transform to get an MoT procedure. This method avoids the shadow region problem by working in transform domain.

The BLIF method, as suggested by D. S. Weile *et al.* [60], uses very smooth temporal basis functions to ease the integration. We will discuss both BLIF and CQ methods in the next chapter in detail.

The fifth method, proposed by A. J. Pray, N. V. Nair, and B. Shanker, expands a conventional causal temporal Galerkin basis function into a series of functions that span the patch spatially, thus avoiding the shadow region entirely. It is based on the undifferentiated form of the TDIEs, and relies on deriving an alternate representation of convolution between the retarded potential and the space-time basis function [39].

## 1.2 Purpose and Method

The “shadow region” integration problem demonstrates that the stability of time domain integral equation approaches to the computation of electromagnetic scattering is profoundly affected by the accuracy of the underlying numerical integration methods used for computation of the kernel elements. While the nature of all five of these schemes discussed in the last subsection suggest that the accuracy of kernel element computations is paramount in governing their stability, integral computation is discussed briefly if at all in most of them. (Indeed, the papers most obsessed with integration accuracy are those using “exact” integrals, and even these schemes are forced to do some numerical quadrature computations [52] [67] [64].)

In most publications, numerical integrals are assumed exact, and higher integral orders are assumed to deliver higher accuracy. To the author’s knowledge, among all the papers discussing TDIE solvers, there is no paper specifically mentioning the absolute or relative error of the numerical integrals, and relating them to the stability. The accuracy of integrals is never quantified, and its effect on stability is understood in a nebulous manner at best.

In this paper, we examine the nature of the relationship between numerical integration accuracy and the stability in the context of the CQ approach of [59] and BLIF approach of [60]. During the course of the discussion, we will see that the stability of these methods can be improved by increasing the accuracy of the numerical integrals involved, and that in many cases integral accuracy in the near field is more important than far field.

That the result presented in this work is trivial is belied largely by the current confusion in the literature: the stability of different methods in the current estimation of the community depends essentially on the reportage of the authors who first developed the method. As far as the author knows, all the information about the stability of certain methods on different geometries are in the papers where authors first developed these methods. Researchers use numerical results to support the algorithms developed in their papers. The stability information only comes from the numerical result part

of a paper which follows the mathematical derivations.

In this thesis, adaptive quadrature is used to quantify the accuracy of key integrals in the time domain integral equation formulation. By adjusting the accuracy setting of the integration rules, we can investigate the impact of integration accuracy on the stability of time domain integral equation solvers. We ultimately conclude that these methods are more reliable than previously thought, and that researchers should be more careful in discussing their results.

The stability and the computational complexity are two focus points in the research of TDIE approaches. Yet unlike computational complexity, the stability of TDIE solvers is never quantified. We hope this work will demonstrate that the five approaches currently available in the literature simply make possible integrals accurate enough to achieve a stable method, and that stability hinges critically on the implementation of the integrals computed.

## Chapter 2

### FORMULATION

This chapter discusses the TDIEs and numerical algorithms used in this paper. Subsection 2.1 describes the formulation of TDIEs. Then, Section 2.2 discusses the spatial discretization using MoM. The typical MoM process is described in Section 2.2.1 and spatial basis functions are discussed in Subsections 2.2.2. Section 2.3 discusses the temporal discretization methods used to solve TDIEs. The formulation of CQ is discussed in Subsection 2.3.1 and the formulation of BLIF is discussed in Subsection 2.3.2. Section 2.4 discusses other numerical algorithms used in our work. Subsection 2.4.1 introduces one dimension Gaussian quadratures. Subsection 2.4.2 discusses two dimension Gaussian quadratures on triangles. Subsection 2.4.3 describes the method we use to deal with singular integrals. Subsection 2.4.4 discusses the adaptive integral method (AIM), which is used here so that moderately large problems may be analyzed to ensure that our results are not biased to small problems. Finally, Subsection 2.4.5 describes the adaptive quadrature technique used in numerical integrations in this paper so that the accuracy can be set with some precision.

#### 2.1 Time Domain Integral Equations

##### 2.1.1 Maxwell Equations

Electromagnetic phenomena are governed by the Maxwell Equations. These are a set of four equations developed by different researchers between the end of the

eighteenth and mid-nineteenth centuries. In differential form, Maxwell equations can be written as:

$$\nabla \times \mathbf{E} = -\frac{\partial \mathbf{B}}{\partial t} - \mathbf{M} \quad (2.1)$$

$$\nabla \times \mathbf{H} = \frac{\partial \mathbf{D}}{\partial t} + \mathbf{J} \quad (2.2)$$

$$\nabla \cdot \mathbf{D} = q_e \quad (2.3)$$

$$\nabla \cdot \mathbf{B} = q_m. \quad (2.4)$$

Here, we use SI units throughout. Thus,  $q_e$  is the electric charge density in  $\text{C}/\text{m}^3$ , and  $q_m$  is the magnetic charge density in  $\text{Wb}/\text{m}^3$ . (Magnetic charge is, of course, fictitious, but can be used through the equivalence principles of electromagnetics to represent the effects of fields created by sources outside a given region of space on that region of space.) The electric current  $\mathbf{J}$  and the magnetic field  $\mathbf{H}$  are measured in  $\text{A}/\text{m}$  while the magnetic current  $\mathbf{M}$  and electric field  $\mathbf{E}$  are measured in  $\text{V}/\text{m}$ . Finally,  $\mathbf{D}$  is the electric flux density measured in  $\text{C}/\text{m}^2$ , and  $\mathbf{B}$  is the magnetic flux density measured in T.

Although not independent, the continuity equation is often used to relate the current density  $\mathbf{J}$  and the charge density  $q_e$ . It is given by

$$\nabla \cdot \mathbf{J} = -\frac{\partial q_e}{\partial t}. \quad (2.5)$$

A similar equation can be derived relating magnetic charges to magnetic currents.

When electromagnetic fields are applied to dielectric materials, the electromagnetic waves propagated in these materials will be different from those in free space because of the effect of electrons in the material. We use a set of three equations to represent this effect at the macroscopic scale. These equations are referred as the *constitutive relations*. In general, in a linear, isotropic medium, they take the form

$$\mathbf{D} = \hat{\epsilon} * \mathbf{E} \quad (2.6)$$

$$\mathbf{B} = \hat{\mu} * \mathbf{H} \quad (2.7)$$

$$\mathbf{J} = \hat{\sigma} * \mathbf{E} \quad (2.8)$$

where  $*$  represents convolution,  $\hat{\epsilon}$  is the time varying permittivity (F/m),  $\hat{\mu}$  is the time varying permeability (H/m), and  $\hat{\sigma}$  is the time varying conductivity of the medium (S/m), For free space,

$$\hat{\epsilon} = \epsilon_0 \delta(t) \text{ where } \epsilon_0 \approx 8.854 \times 10^{-12} \approx \frac{10^{-9}}{36\pi} \text{ (F/m)} \quad (2.9)$$

$$\hat{\mu} = \mu_0 \delta(t) \text{ where } \mu_0 = 4\pi \times 10^{-7} \text{ (H/m), and} \quad (2.10)$$

$$\hat{\sigma} = 0, \quad (2.11)$$

where,  $\delta(t)$  is the Dirac delta function. For isotropic, linear, time-invariant, frequency-independent dielectrics, the constitutive relations can be simplified to read

$$\mathbf{D} = \epsilon_r \epsilon_0 \mathbf{E} \quad (2.12)$$

$$\mathbf{B} = \mu_r \mu_0 \mathbf{H} \text{ and} \quad (2.13)$$

$$\mathbf{J} = \sigma \mathbf{E}, \quad (2.14)$$

where  $\epsilon_r$  and  $\mu_r$  are unitless relative permittivity and relative permeability. They and  $\sigma$  depend on the material itself.

Electromagnetic fields across interfaces between different media can have abrupt changes in charge and current densities. Discontinuous charge and current densities are related to electromagnetic fields by boundary conditions. For dielectrics of finite conductivity, the boundary condition for the tangential components of electromagnetic fields across the interface can be written as

$$(\mathbf{E}_2 - \mathbf{E}_1) \times \hat{\mathbf{n}} = 0 \quad (2.15)$$

$$\hat{\mathbf{n}} \times (\mathbf{H}_2 - \mathbf{H}_1) = 0, \quad (2.16)$$

where the interface in question divides space into two regions called 1 and 2,  $\hat{\mathbf{n}}$  is a unit normal defined on the interface pointing from region 1 into region 2, and the subscripts on the field variables denote the field value just inside the given region.

For boundaries between materials of finite loss and perfect electric conductors (PECs), the boundary conditions for the tangential components of the fields just outside the PEC take the form

$$\mathbf{E} \times \hat{\mathbf{n}} = 0 \quad (2.17)$$

$$\hat{\mathbf{n}} \times \mathbf{H} = \mathbf{J}. \quad (2.18)$$

### 2.1.2 Auxiliary Potentials

In a magnetic source free region, (2.4) indicates  $\nabla \cdot \mathbf{B} = 0$ . Since the curl of a vector has no divergence, in a homogeneous, source-free region we can define  $\mathbf{H}$  as the curl of an auxiliary vector potential function  $\mathbf{A}$ . Thus, we write  $\mathbf{H}$  as

$$\mathbf{H} = \nabla \times \mathbf{A}. \quad (2.19)$$

Substituting (2.19) into (2.1), we get

$$\nabla \times \left( \mathbf{E} + \mu \frac{\partial \mathbf{A}}{\partial t} \right) = 0. \quad (2.20)$$

Since the gradient of a scalar has no curl, we can define a scalar electric potential  $\phi_e$  as

$$\nabla \phi_e = - \left( \mathbf{E} + \mu \frac{\partial \mathbf{A}}{\partial t} \right). \quad (2.21)$$

Substituting (2.21) into (2.2), we get

$$\nabla^2 \mathbf{A} - \epsilon \mu \frac{\partial^2 \mathbf{A}}{\partial t^2} = \nabla (\nabla \cdot \mathbf{A}) + \nabla \left( \epsilon \frac{\partial \phi_e}{\partial t} \right) - \mathbf{J}. \quad (2.22)$$

Up to this point, we have only defined the magnetic vector potential  $\mathbf{A}$  through its curl; that is to say through its mixed, first-order derivatives. This leaves us able to define the derivative of each component of  $\mathbf{A}$  with respect to its own variable; that is to say the *divergence* of  $\mathbf{A}$ . To simplify (2.22), we define the divergence of  $\mathbf{A}$  to be

$$\nabla \cdot \mathbf{A} = -\epsilon \frac{\partial \phi_e}{\partial t}. \quad (2.23)$$

We then substitute (2.23) into (2.21) and take the temporal derivative of  $\mathbf{E}$  to get

$$\frac{\partial \mathbf{E}}{\partial t} = \frac{1}{\epsilon} \nabla (\nabla \cdot \mathbf{A}) - \mu \frac{\partial^2 \mathbf{A}}{\partial t^2} \quad (2.24)$$

Similarly, in a region free of electrical sources, we can define

$$\mathbf{E} = -\nabla \times \mathbf{F}. \quad (2.25)$$

The divergence of the *electric vector potential*  $\mathbf{F}$ , as it is undefined by this curl equation, can be taken to be

$$\nabla \cdot \mathbf{F} = -\mu \frac{\partial \phi_m}{\partial t}. \quad (2.26)$$

Thus, the temporal derivative of  $\mathbf{H}$  in terms of  $\mathbf{F}$  can be written as

$$\frac{\partial \mathbf{H}}{\partial t} = \frac{1}{\mu} \nabla(\nabla \cdot \mathbf{F}) - \epsilon \frac{\partial^2 \mathbf{F}}{\partial t^2}. \quad (2.27)$$

Using  $\mathbf{A}$  and  $\mathbf{F}$ , the temporal derivative of  $\mathbf{E}$  created by any combination of sources can be written as

$$\frac{\partial \mathbf{E}}{\partial t} = -\frac{1}{\epsilon} \nabla(\nabla \cdot \mathbf{A}) - \mu \frac{\partial^2 \mathbf{A}}{\partial t^2} - \nabla \times \frac{\partial \mathbf{F}}{\partial t}, \quad (2.28)$$

and the temporal derivative of  $\mathbf{H}$  can be written in terms of  $\mathbf{A}$  and  $\mathbf{F}$  as

$$\frac{\partial \mathbf{H}}{\partial t} = \frac{1}{\mu} \nabla(\nabla \cdot \mathbf{F}) - \epsilon \frac{\partial^2 \mathbf{F}}{\partial t^2} + \nabla \times \frac{\partial \mathbf{A}}{\partial t}. \quad (2.29)$$

### 2.1.3 Green Function Solutions

With the previous gauge in (2.23) for  $\mathbf{A}$ , (2.22) can be simplified to

$$\nabla^2 \mathbf{A} - \epsilon \mu \frac{\partial^2 \mathbf{A}}{\partial t^2} = -\mathbf{J}. \quad (2.30)$$

Using the Green's function method,  $\mathbf{A}$  can be shown to be given by

$$\mathbf{A}(\mathbf{r}, t) = \iint_S \frac{\mathbf{J}\left(\mathbf{r}', t - \frac{|\mathbf{r}-\mathbf{r}'|}{c}\right)}{4\pi|\mathbf{r}-\mathbf{r}'|} d\mathbf{r}', \quad (2.31)$$

where  $c = (\sqrt{\epsilon\mu})^{-1}$  is the light velocity in the isotropic, homogeneous medium in question.

Similarly,  $\mathbf{F}$  can be written as

$$\mathbf{F}(\mathbf{r}, t) = \iint_S \frac{\mathbf{M}\left(\mathbf{r}', t - \frac{|\mathbf{r}-\mathbf{r}'|}{c}\right)}{4\pi|\mathbf{r}-\mathbf{r}'|} d\mathbf{r}' \quad (2.32)$$

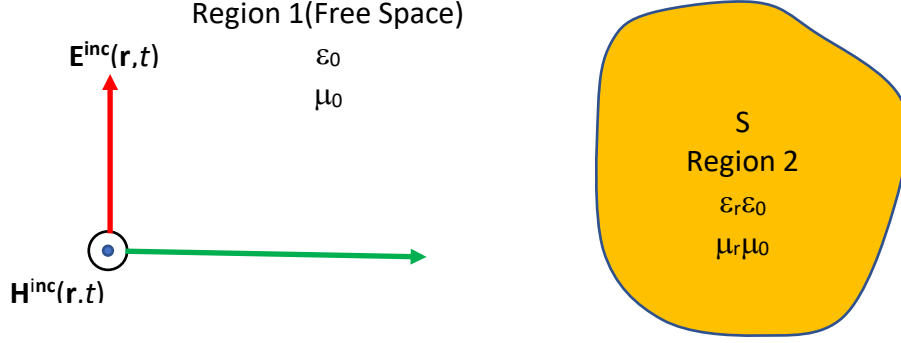


**Figure 2.1:** A classic scattering problem.

under the same conditions.

To simplify the remaining exposition, we define an operator  $\mathcal{L}_c$  as:

$$\mathcal{L}_c(\mathbf{f}(\mathbf{r}, t)) = \iint_S \frac{\mathbf{f}\left(\mathbf{r}', t - \frac{|\mathbf{r}-\mathbf{r}'|}{c}\right)}{4\pi|\mathbf{r}-\mathbf{r}'|} d\mathbf{r}'. \quad (2.33)$$

Note that the subscript “ $c$ ” denotes the wave speed in the medium in question, and appears in the operator definition as shown.

### 2.1.4 Formulation of Time Domain Integral Equations

Fig. 2.1 shows an isotropic, homogenous, penetrable object  $S$  placed in free space being illuminated by an incident electromagnetic wave with electric field  $\mathbf{E}^{\text{inc}}(\mathbf{r}, t)$  and magnetic field  $\mathbf{H}^{\text{inc}}(\mathbf{r}, t)$ . Region 1 is free space. Region 2 is characterized by a constant, frequency-independent relative permeability  $\mu_r$  and a constant, frequency-independent relative permittivity  $\epsilon_r$ .

According to the surface equivalence principle, we can define a equivalent electric currents  $\mathbf{J}(\mathbf{r}, t)$  and magnetic currents  $\mathbf{M}(\mathbf{r}, t)$  on  $S$  which replicate the scattered electromagnetic fields  $\mathbf{E}^{\text{sca}}(\mathbf{r}, t)$  and  $\mathbf{H}^{\text{sca}}(\mathbf{r}, t)$  in region 1, and internal electric fields  $\mathbf{E}^2(\mathbf{r}, t)$  and  $\mathbf{H}^2(\mathbf{r}, t)$  in region 2.

The temporal derivatives of the scattered fields in region 1 can be written as

$$\dot{\mathbf{E}}^{\text{sca}}(\mathbf{r}, t) = -\mu_0 \mathcal{L}_{c_0}(\ddot{\mathbf{J}}) + \frac{1}{\epsilon_0} \nabla \mathcal{L}_{c_0}(\nabla' \cdot \mathbf{J}) - \nabla \times \mathcal{L}_{c_0}(\dot{\mathbf{M}}) \quad (2.34)$$

and

$$\dot{\mathbf{H}}^{\text{sca}}(\mathbf{r}, t) = -\epsilon_0 \mathcal{L}_{c_0}(\ddot{\mathbf{M}}) + \frac{1}{\epsilon_0} \nabla \mathcal{L}_{c_0}(\nabla' \cdot \mathbf{M}) + \nabla \times \mathcal{L}_{c_0}(\dot{\mathbf{J}}) \quad (2.35)$$

where  $c_0 = (\mu_0 \epsilon_0)^{-\frac{1}{2}}$  is the free space velocity of electromagnetic waves. A dot above a variable means the value of temporal derivative of the variable evaluated at its temporal argument, i.e.,

$$\dot{\mathbf{f}}(\mathbf{r}, T) = \left. \frac{\partial \mathbf{f}(\mathbf{r}, t)}{\partial t} \right|_{t=T}, \quad (2.36)$$

and multiple dots generalize this rule in the obvious way.

The superposition of the incident and scattered fields yields the original fields in region 1 in the presence of the scatter. Therefore the temporal derivatives of the original fields in region 1 in the presence of the scatter are given by

$$\dot{\mathbf{E}}^1(\mathbf{r}, t) = \dot{\mathbf{E}}^{\text{inc}}(\mathbf{r}, t) + \dot{\mathbf{E}}^{\text{sca}}(\mathbf{r}, t) \quad (2.37)$$

and

$$\dot{\mathbf{H}}^1(\mathbf{r}, t) = \dot{\mathbf{H}}^{\text{inc}}(\mathbf{r}, t) + \dot{\mathbf{H}}^{\text{sca}}(\mathbf{r}, t). \quad (2.38)$$

By substituting Equation (2.34) into Equation (2.37) and Equation (2.35) into Equation (2.38), the temporal derivatives of the total fields in region 1 can be written as

$$\dot{\mathbf{E}}^1(\mathbf{r}, t) = \dot{\mathbf{E}}^{\text{inc}}(\mathbf{r}, t) - \mu_0 \mathcal{L}_{c_0}(\ddot{\mathbf{J}}) + \frac{1}{\epsilon_0} \nabla \mathcal{L}_{c_0}(\nabla' \cdot \mathbf{J}) - \nabla \times \mathcal{L}_{c_0}(\dot{\mathbf{M}}) \quad (2.39)$$

and

$$\dot{\mathbf{H}}^1(\mathbf{r}, t) = \dot{\mathbf{H}}^{\text{inc}}(\mathbf{r}, t) - \epsilon_0 \mathcal{L}_{c_0}(\ddot{\mathbf{M}}) - \frac{1}{\epsilon_0} \nabla \mathcal{L}_{c_0}(\nabla' \cdot \mathbf{M}) + \nabla \times \mathcal{L}_{c_0}(\dot{\mathbf{J}}). \quad (2.40)$$

By a nearly identical argument, the temporal derivatives of the internal fields in region 2 radiated by the surface currents can be written as

$$\dot{\mathbf{E}}^2(\mathbf{r}, t) = \mu_r \mu_0 \mathcal{L}_{c_r}(\ddot{\mathbf{J}}) - \frac{1}{\epsilon_r \epsilon_0} \nabla \mathcal{L}_{c_r}(\nabla' \cdot \mathbf{J}) + \nabla \times \mathcal{L}_{c_r}(\dot{\mathbf{M}}) \quad (2.41)$$

and

$$\dot{\mathbf{H}}^2(\mathbf{r}, t) = \epsilon_r \epsilon_0 \mathcal{L}_{c_r}(\ddot{\mathbf{M}}) - \frac{1}{\mu_r \mu_0} \nabla \mathcal{L}_{c_r}(\nabla' \cdot \mathbf{M}) - \nabla \times \mathcal{L}_{c_r}(\dot{\mathbf{J}}) \quad (2.42)$$

where  $c_r = (\mu_r \mu_0 \epsilon_r \epsilon_0)^{-\frac{1}{2}}$  is the velocity of electromagnetic waves in the dielectric.

In the dielectric case, the tangential components of electrical fields and magnetic fields are continuous across the material boundary. Hence the boundary condition, which relates the total electromagnetic fields in region 1 with those in region 2, can be written as

$$\hat{\mathbf{n}} \times \hat{\mathbf{n}} \times [\dot{\mathbf{E}}^1(\mathbf{r}, t) - \dot{\mathbf{E}}^2(\mathbf{r}, t)] = \mathbf{0}, \quad (2.43)$$

and

$$\hat{\mathbf{n}} \times \hat{\mathbf{n}} \times [\dot{\mathbf{H}}^1(\mathbf{r}, t) - \dot{\mathbf{H}}^2(\mathbf{r}, t)] = \mathbf{0}, \quad (2.44)$$

where  $\hat{\mathbf{n}}$  is the outward pointing normal to the surface  $S$  at  $\mathbf{r}$ . By substituting Equation (2.39) and Equation (2.41) into Equation (2.43), we derive a time domain integral equation of the form

$$\begin{aligned} \dot{\mathbf{E}}^{\text{inc}}(\mathbf{r}, t) = & \mu_0 \mathcal{L}_{c_0}(\ddot{\mathbf{J}}) - \frac{1}{\epsilon_0} \nabla \mathcal{L}_{c_0}(\nabla' \cdot \mathbf{J}) + \nabla \times \mathcal{L}_{c_0}(\dot{\mathbf{M}}) \\ & + \mu_r \mu_0 \mathcal{L}_{c_r}(\ddot{\mathbf{J}}) - \frac{1}{\epsilon_r \epsilon_0} \nabla \mathcal{L}_{c_r}(\nabla' \cdot \mathbf{J}) + \nabla \times \mathcal{L}_{c_r}(\dot{\mathbf{M}}). \end{aligned} \quad (2.45)$$

Similarly, by substituting Equation (2.40) and Equation (2.42) into Equation (2.44), we write the time domain integral equation forcing continuity of the magnetic field as

$$\begin{aligned} \dot{\mathbf{H}}^{\text{inc}}(\mathbf{r}, t) = & \epsilon_0 \mathcal{L}_{c_0}(\ddot{\mathbf{M}}) - \frac{1}{\mu_0} \nabla \mathcal{L}_{c_0}(\nabla' \cdot \mathbf{M}) - \nabla \times \mathcal{L}_{c_0}(\dot{\mathbf{J}}) \\ & + \epsilon_r \epsilon_0 \mathcal{L}_{c_r}(\ddot{\mathbf{M}}) - \frac{1}{\mu_r \mu_0} \nabla \mathcal{L}_{c_r}(\nabla' \cdot \mathbf{M}) - \nabla \times \mathcal{L}_{c_r}(\dot{\mathbf{J}}). \end{aligned} \quad (2.46)$$

We can also write the above two equations in non-differential form in time domain by integrating them over time from an initial time we denote a  $t = 0$  until the current time. (Of course in doing this we assume that the scatterer is quiescent at the initial time; that is all fields and sources vanish at  $t = 0$ .) The non-differential integral equation for the electric field takes the form

$$\begin{aligned} \mathbf{E}^{\text{inc}}(\mathbf{r}, t) = & \mu_0 \mathcal{L}_{c_0}(\dot{\mathbf{J}}) - \frac{1}{\epsilon_0} \int_0^t \nabla \mathcal{L}_{c_0}(\nabla' \cdot \mathbf{J}) dt + \nabla \times \mathcal{L}_{c_0}(\mathbf{M}) \\ & + \mu_r \mu_0 \mathcal{L}_{c_r}(\dot{\mathbf{J}}) - \frac{1}{\epsilon_r \epsilon_0} \int_0^t \nabla \mathcal{L}_{c_r}(\nabla' \cdot \mathbf{J}) dt + \nabla \times \mathcal{L}_{c_r}(\mathbf{M}). \end{aligned} \quad (2.47)$$

And that for the magnetic field can be written as

$$\begin{aligned} \mathbf{H}^{\text{inc}}(\mathbf{r}, t) &= \epsilon_0 \mathcal{L}_{c_0}(\dot{\mathbf{M}}) - \frac{1}{\mu_0} \int_0^t \nabla \mathcal{L}_{c_0}(\nabla' \cdot \mathbf{M}) dt - \nabla \times \mathcal{L}_{c_0}(\mathbf{J}) \\ &+ \epsilon_r \epsilon_0 \mathcal{L}_{c_r}(\dot{\mathbf{M}}) - \frac{1}{\mu_r \mu_0} \int_0^t \nabla \mathcal{L}_{c_r}(\nabla' \cdot \mathbf{M}) dt - \nabla \times \mathcal{L}_{c_r}(\mathbf{J}). \end{aligned} \quad (2.48)$$

The most important differences between the differentiated and undifferentiated forms of the integral equations are:

- The differential form of the TDIEs require that the incident waves must be differentiable. If the incident fields are square waves or some other discontinuous form, the differentiated TDIEs are undefined at points of discontinuity.
- Numerical integration is in general more accurate than numerical differentiation since differentiation inevitably involves subtraction and hence flirts with catastrophic cancellation.
- The strong differential form requires the temporal basis functions to be second-order differentiable.

We can also develop TDIEs for PEC scatters. Consider a perfectly conducting surface  $S$  in free space excited by an incident electromagnetic wave with electric field  $\mathbf{E}^{\text{inc}}(\mathbf{r}, t)$  and magnetic field  $\mathbf{H}^{\text{inc}}(\mathbf{r}, t)$  as shown in Fig. 2.2.

This excitation will create induced surface currents  $\mathbf{J}(\mathbf{r}, t)$  on  $S$  that will radiate scattered electric fields  $\mathbf{E}^{\text{sca}}(\mathbf{r}, t)$  and magnetic fields  $\mathbf{H}^{\text{sca}}(\mathbf{r}, t)$ . The temporal derivatives of these scattered fields on the surface are given by [31]

$$\begin{aligned} \dot{\mathbf{E}}^{\text{sca}}(\mathbf{r}, t) &= -\mu_0 \iint_S \frac{\ddot{\mathbf{J}}\left(\mathbf{r}', t - \frac{|\mathbf{r}-\mathbf{r}'|}{c_0}\right)}{4\pi|\mathbf{r}-\mathbf{r}'|} d\mathbf{r}' + \frac{1}{\epsilon_0} \nabla \iint_S \frac{\nabla' \cdot \mathbf{J}\left(\mathbf{r}', t - \frac{|\mathbf{r}-\mathbf{r}'|}{c_0}\right)}{4\pi|\mathbf{r}-\mathbf{r}'|} d\mathbf{r}' \\ &= -\mu_0 \mathcal{L}_{c_0}(\ddot{\mathbf{J}}) + \frac{1}{\epsilon_0} \nabla \mathcal{L}_{c_0}(\nabla' \cdot \mathbf{J}) \end{aligned} \quad (2.49)$$

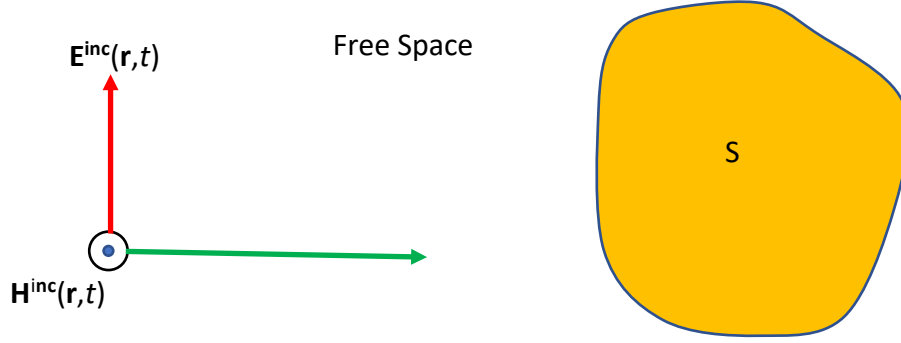


**Figure 2.2:** A classic scattering problem for PEC.

and

$$\begin{aligned}
 \dot{\mathbf{H}}^{\text{sca}}(\mathbf{r}, t) &= \frac{1}{2} \mathbf{J}(\mathbf{r}, t) \times \hat{\mathbf{n}} + \nabla \times \iint_S \frac{\dot{\mathbf{J}}\left(\mathbf{r}', t - \frac{|\mathbf{r}-\mathbf{r}'|}{c_0}\right)}{4\pi|\mathbf{r}-\mathbf{r}'|} d\mathbf{r}' \\
 &= \frac{1}{2} \mathbf{J} + \nabla \times \mathcal{L}_{c_0}(\dot{\mathbf{J}}).
 \end{aligned} \tag{2.50}$$

The boundary condition in (2.17) which relates the incident and scattered electrical fields can be rewritten as

$$-\hat{\mathbf{n}} \times (\hat{\mathbf{n}} \times [\dot{\mathbf{E}}^{\text{inc}}(\mathbf{r}, t) + \dot{\mathbf{E}}^{\text{sca}}(\mathbf{r}, t)]) = 0. \tag{2.51}$$

The magnetic field condition (2.18) similarly becomes can be

$$\hat{\mathbf{n}} \times [\dot{\mathbf{H}}^{\text{inc}}(\mathbf{r}, t) + \dot{\mathbf{H}}^{\text{sca}}(\mathbf{r}, t)] = \dot{\mathbf{J}}(\mathbf{r}, t). \tag{2.52}$$

By substituting (2.49) into (2.51), we derive the time domain EFIE (TD-EFIE):

$$\begin{aligned}
 \dot{\mathbf{E}}^{\text{inc}}(\mathbf{r}, t) &= \mu_0 \iint_S \frac{\ddot{\mathbf{J}}\left(\mathbf{r}', t - \frac{\|\mathbf{r}-\mathbf{r}'\|}{c_0}\right)}{4\pi|\mathbf{r}-\mathbf{r}'|} d\mathbf{r}' - \frac{1}{\epsilon_0} \nabla \iint_S \frac{\nabla' \cdot \mathbf{J}\left(\mathbf{r}', t - \frac{\|\mathbf{r}-\mathbf{r}'\|}{c_0}\right)}{4\pi(\mathbf{r}-\mathbf{r}')} d\mathbf{r}' \\
 &= \mu_0 \mathcal{L}_{c_0}(\ddot{\mathbf{J}}) - \frac{1}{\epsilon_0} \nabla \mathcal{L}_{c_0}(\nabla' \cdot \mathbf{J})
 \end{aligned} \tag{2.53}$$

Similarly, using Equation (2.52), we write the time domain MFIE (TD-MFIE) as

$$\begin{aligned}\hat{\mathbf{n}} \times \dot{\mathbf{H}}^{\text{inc}}(\mathbf{r}, t) &= -\frac{1}{2}\dot{\mathbf{J}}(\mathbf{r}, t) - \hat{\mathbf{n}} \times \nabla \times \iint_S \frac{\dot{\mathbf{J}}(\mathbf{r}', t - \frac{|\mathbf{r}-\mathbf{r}'|}{c_0})}{4\pi|\mathbf{r}-\mathbf{r}'|} d\mathbf{r}' \\ &= -\frac{1}{2}\dot{\mathbf{J}} - \nabla \times \mathcal{L}_{c_0}(\dot{\mathbf{J}}).\end{aligned}\quad (2.54)$$

The corresponding undifferentiated forms are given by

$$\mathbf{E}^{\text{inc}}(\mathbf{r}, t) = \mu_0 \mathcal{L}_{c_0}(\dot{\mathbf{J}}) - \frac{1}{\epsilon_0} \int_0^t \nabla \mathcal{L}_{c_0}(\nabla' \cdot \mathbf{J}) dt, \quad (2.55)$$

and

$$\mathbf{H}^{\text{inc}}(\mathbf{r}, t) \times \hat{\mathbf{n}} = -\nabla \times \mathcal{L}_{c_0}(\mathbf{J}) - \frac{1}{2}\mathbf{J}. \quad (2.56)$$

Note that the TD-MFIEs apply only to closed surfaces, since the boundary condition upon which they are based becomes ill-defined for open surfaces.

For closed PEC objects, time domain combined field integral equations (TD-CFIEs) are used to avoid ill-posedness of the equations near internal resonances. By taking a weighted average of the TD-EFIE and TD-MFIE, we formulate a time-differentiated TD-CFIE as

$$\begin{aligned}\hat{\mathbf{n}} \times \left[ \frac{\alpha}{\eta_0} \dot{\mathbf{E}}^{\text{inc}}(\mathbf{r}, t) + (1 - \alpha) \dot{\mathbf{H}}^{\text{inc}}(\mathbf{r}, t) \right] &= (1 - \alpha) \dot{\mathbf{J}}(\mathbf{r}, t) - \\ \hat{\mathbf{n}} \times \left[ -\frac{\alpha}{\eta_0} \mu_0 \mathcal{L}_{c_0}(\ddot{\mathbf{J}}) + \frac{1}{\epsilon_0} \nabla \mathcal{L}_{c_0}(\nabla' \cdot \mathbf{J}) + (1 - \alpha) \nabla \times \mathcal{L}_{c_0}(\dot{\mathbf{J}})(\mathbf{r}, t) \right],\end{aligned}\quad (2.57)$$

where  $0 \leq \alpha \leq 1$ . Integrating this result, the non-differentiated TD-CFIE can be written as:

$$\begin{aligned}\hat{\mathbf{n}} \times \left[ \frac{\alpha}{\eta_0} \mathbf{E}^{\text{inc}}(\mathbf{r}, t) + (1 - \alpha) \mathbf{H}^{\text{inc}}(\mathbf{r}, t) \right] &= (1 - \alpha) \mathbf{J}(\mathbf{r}, t) - \\ \hat{\mathbf{n}} \times \left[ -\frac{\alpha}{\eta_0} \mu_0 \mathcal{L}_{c_0}(\dot{\mathbf{J}}) + \frac{1}{\epsilon_0} \int_0^t \nabla \mathcal{L}_{c_0}(\nabla' \cdot \mathbf{J}) + (1 - \alpha) \nabla \times \mathcal{L}_{c_0}(\mathbf{J})(\mathbf{r}, t) \right].\end{aligned}\quad (2.58)$$

## 2.2 Spatial Discretization

### 2.2.1 Method of Moments

The objective of formulating integral equations in both the time and frequency domains is to create numerical methods capable of efficiently and accurately discretizing

them to solve for the unknown function in the integrand. Though other methods exist, in CEM practice, the integral equation is most often numerically solved for the unknown induced current density using method of moments (MoM). To demonstrate this process, consider the abstract equation

$$\mathcal{L}(f) = g \tag{2.59}$$

where  $\mathcal{L}$  is a linear operator,  $f$  is the unknown function to be found, and  $g$  is a known function. Since  $f$  and  $g$  are generally functions supported over some region of space or time, this represents an infinity of unknowns (as  $f$  is usually defined over a region of continuous space) and an infinity of conditions (as the equation must be true over the continuous support of  $g$ .) The MoM is a method for constructing a finite approximation to  $f$ .

First, we construct a linear combination of well-defined functions  $S_n$ , weighted by unknown coefficients  $a_n$ , to approximate the unknown function as

$$f \approx \sum_{n=1}^N a_n S_n. \tag{2.60}$$

Substituting (2.60) into (2.59), we find.

$$\sum_{n=1}^N a_n (\mathcal{L}(S_n)) = g. \tag{2.61}$$

This equation still represents an infinity of conditions, but it has a finite number of unknowns.

To reduce the dimensionality of the condition space, we introduce a process called “testing” (or “computing an inner product”). The inner product of two functions  $a(\tau)$  and  $b(\tau)$  defined over a support set  $S$  is given by

$$\langle a, b \rangle = \int_S a(\tau) \cdot b(\tau) d\tau. \tag{2.62}$$

Note that in writing this, we assume that  $\tau$  any dimension, so the integral may be multidimensional. Similarly,  $a$  and  $b$  may be vectors, in which case the “dot” (“.”) has its conventional meaning. To obtain the unknown coefficients, we use a set of well

defined functions  $T_m$ , ( $m = 1, 2, \dots, N$ ) called “testing functions” to test both sides of the equation (2.61):

$$\sum_{m=1}^N \sum_{n=1}^N a_n \langle T_m, \mathcal{L}(S_n) \rangle = \sum_{m=1}^N \langle T_m, g \rangle. \quad (2.63)$$

This equation is often rendered in matrix form as

$$\mathbf{Z}\mathbf{I} = \mathbf{V} \quad (2.64)$$

Matrix  $\mathbf{Z}$  is of size  $N \times N$ . The  $(m, n)$ <sup>th</sup> element ( $1 \leq m \leq N, 1 \leq n \leq N$ ) of  $\mathbf{Z}$  is given by

$$Z_{mn} = \langle T_m, \mathcal{L}(S_n) \rangle. \quad (2.65)$$

The vector  $\mathbf{V}$  is a vector of  $N$  elements. Its  $m$ <sup>th</sup> element ( $1 \leq m \leq M$ ) is:

$$V_m = \langle T_m, g \rangle. \quad (2.66)$$

The vector  $\mathbf{I}$  is a vector of the unknown coefficients  $a_n, n = 1, 2, \dots, N$ . Solving this matrix equation yields the unknown coefficients and hence an approximation to the unknown through (2.60). In practice, we often use Galerkin methods in which the testing functions are the same as the basis functions.

In the frequency domain, we directly use this process to discretize integral equations in space and then solve for the current density at each value of the frequency. In time domain, we also use this process for spatial discretization. We consider the time domain here. In this case, spatial discretization is accomplished with the approximation

$$\mathbf{J}(\mathbf{r}, t) \approx \sum_{n=1}^{N_s} \iota_n(t) \mathbf{S}_n(\mathbf{r}). \quad (2.67)$$

(In the frequency domain, we may take  $\iota_n(t) = I_n e^{j\omega t}$ , and note that every value of  $\omega$  will lead to an independent set of equations.) This is substituted into (2.53), the

TD-EFIE, multiplied by the  $\mathbf{S}_m(\mathbf{r})$ ,  $m = 1, 2, \dots, N_s$ , and integrated over  $S$  yielding

$$\begin{aligned} \iint_S \mathbf{S}_m(\mathbf{r}) \cdot \mathbf{E}(\mathbf{r}, t) d\mathbf{r} &= \sum_{n=0}^{N_s} \iint_S \iint_S \mu_0 \frac{\mathbf{S}_m(\mathbf{r}) \cdot \mathbf{S}_n(\mathbf{r}')}{4\pi R} \ddot{i}_n(\tau) d\mathbf{r}' d\mathbf{r} \\ &\quad - \sum_{n=0}^{N_s} \iint_S \iint_S \frac{[\nabla \cdot \mathbf{S}_m(\mathbf{r})][\nabla' \cdot \mathbf{S}_n(\mathbf{r}')] \iota_n(\tau)}{4\pi\epsilon_0 R} d\mathbf{r}' d\mathbf{r}. \end{aligned} \quad (2.68)$$

### 2.2.2 Spatial Basis Functions

The spatial basis functions used here are high order interpolatory divergence-conforming vector bases. They are called ‘‘GWP’’ basis functions in this work because they were proposed by R. Graglia, D. Wilton, and A. Peterson [19]. They are essentially high-order generalizations of the older RWG bases [44], that are now the zeroth-order GWP bases. In our work, we used the zeroth-order and first-order GWP functions. Without losing generality, here we use a flat triangle to show how they work. (Curvilinear generalizations are remarkably easy to create given this description; see [19] for details. Essentially, edge vectors are replaced by local derivatives, and areas are replaced by Jacobians.)

Flat triangles are often used in computer modeling to mesh the surfaces of 3-D objects in the real world, yet they are 2-D surfaces in essence. Modeling the current on the surface of an arbitrary oriented triangle in a 3-D world can be difficult using Cartesian coordinates; hence, area coordinates are introduced. Under an area coordinate system, the position of a point is denoted by its position relative to the vertices of the triangle and thus in a manner totally independent from the position of the triangle itself in 3-D space.

Area coordinates on triangles are also called barycentric coordinates and were introduced by August Ferdinand M6obius in 1827 [22]. Consider a triangle with three vertices located at the points  $\mathbf{r}_1$ ,  $\mathbf{r}_2$ , and  $\mathbf{r}_3$ , and a point  $\mathbf{r}$  with normalized area coordinates  $(\xi_1, \xi_2, \xi_3)$ . The point  $\mathbf{r}$  is located by the formula

$$\mathbf{r} = \xi_1 \mathbf{r}_1 + \xi_2 \mathbf{r}_2 + \xi_3 \mathbf{r}_3. \quad (2.69)$$

The coordinate  $\xi_i$ ,  $i \in \{1, 2, 3\}$ , is the ratio of two areas. The numerator is the area of the sub-triangle specified by the point  $\mathbf{r}$  and the edge opposite to vertex  $\mathbf{r}_i$ . The denominator is the area of the triangle with vertices  $\mathbf{r}_1$ ,  $\mathbf{r}_2$ , and  $\mathbf{r}_3$ . Clearly, This definition implies

$$\xi_1 + \xi_2 + \xi_3 = 1. \quad (2.70)$$

Note that when one of the variables  $\xi_i = 0, i \in \{1, 2, 3\}$ , the point in question is on the edge opposite the node  $\mathbf{r}_i$ . When two of the barycentric coordinates vanish, the third (call it  $\xi_k$ ) is necessarily unity, and the point in question is  $\mathbf{r}_k$ .

For the interpolation on the canonical elements such as flat triangles, Lagrangian interpolation methods are often used. To begin our exposition, we examine the Silvester form of the Lagrange interpolation polynomials. We divide the unit interval  $[0, 1]$  into  $s$  uniform subintervals, which results in  $s + 1$  nodes. A  $s^{\text{th}}$ -degree polynomial can interpolate these points. Now the Silvester(-Lagrange) polynomial of degree  $i$  can be written as

$$P_i(s, \xi) = \begin{cases} \frac{1}{i!} \prod_{k=0}^{i-1} (s\xi - k), & 1 \leq i \leq s. \\ 1, & i = 0 \end{cases} \quad (2.71)$$

Note that the zeroth-degree Silvester polynomial is 1 at  $\xi = 0$ . The Silvester polynomial of degree  $i > 0$  is 1 at  $\xi = i/s$  and 0 at  $\xi = 0, 1/s, 2/s, \dots, (i - 1)/s$ .

We can also define a shifted Silvester polynomial as

$$\hat{P}_i(s, \xi) = \begin{cases} \frac{1}{(i-1)!} \prod_{k=1}^{i-1} (s\xi - k), & 2 \leq i \leq s + 1. \\ 1, & i = 1. \end{cases} \quad (2.72)$$

The above shifted Silvester polynomial is 1 at  $\xi = i/s$  and 0 at  $\xi = 1/s, 2/s, \dots, (i - 1)/s$ . Note that the polynomial above is actually of degree  $i - 1$ . For this reason, when  $i$  is 0, we define

$$\lim_{i \rightarrow 0} \frac{\hat{P}_i(s, \xi)}{i} = \frac{1}{s\xi}. \quad (2.73)$$

Within a triangle whose normalized area coordinates are  $(\xi_1, \xi_2, \xi_3)$ , we define a  $s^{\text{th}}$  order Lagrange polynomial as

$$\alpha_{ijk}(\xi_1, \xi_2, \xi_3) = P_i(s, \xi_1)P_j(s, \xi_2)P_k(s, \xi_3), \quad (2.74)$$

where  $i, j$ , and  $k$  are integers with  $0 \leq i, j, k \leq s$  and  $i + j + k = s$ . This polynomial is useful because

$$\alpha_{ijk}\left(\frac{m}{s}, \frac{n}{s}, \frac{p}{s}\right) = \delta_{im}\delta_{jn}\delta_{kp}, \quad (2.75)$$

where  $m, n$ , and  $p$  also satisfy  $m, n$ , and  $p$  are integers with  $0 \leq m, n, p \leq s$  and  $m + n + p = s$ , and  $\delta_{ij}$  is the Kroenecker delta, defined by

$$\delta_{ij} = \begin{cases} 1 & \text{if } i = j, \\ 0 & \text{if } i \neq j. \end{cases} \quad (2.76)$$

We also define a shifted Silvester polynomial of three variables with the formula

$$\hat{\alpha}_{ijk}(\xi_1, \xi_2, \xi_3) = \hat{P}_i(s+2, \xi_1)\hat{P}_j(s+2, \xi_2)\hat{P}_k(s+2, \xi_3), \quad (2.77)$$

where  $i + j + k = s + 2$ . Note that it actually has degree  $s - 1$ . This function will be useful in defining GWP bases below.

To define the GWP basis functions on a flat triangle, we define three edge vectors  $\mathbf{l}_1, \mathbf{l}_2$  and  $\mathbf{l}_3$ , between the corner nodes as shown in Fig. 2.3. Vertex  $\mathbf{r}_i$  is opposite to edge vector  $\mathbf{l}_i$ . The direction of the edge vector is cyclically increasing; that is,  $\mathbf{l}_1$  points from  $\mathbf{r}_2$  to  $\mathbf{r}_3$ ,  $\mathbf{l}_2$  points from  $\mathbf{r}_3$  to  $\mathbf{r}_1$ , and  $\mathbf{l}_3$  points from  $\mathbf{r}_1$  to  $\mathbf{r}_2$ . Let  $\hat{\mathbf{n}}$  be the unit normal vector of the triangle, i.e.

$$\hat{\mathbf{n}} = \frac{\mathbf{l}_1 \times \mathbf{l}_2}{|\mathbf{l}_1 \times \mathbf{l}_2|} = \frac{\mathbf{l}_2 \times \mathbf{l}_3}{|\mathbf{l}_2 \times \mathbf{l}_3|} = \frac{\mathbf{l}_3 \times \mathbf{l}_1}{|\mathbf{l}_3 \times \mathbf{l}_1|}. \quad (2.78)$$

The Jacobian  $J$  is given by

$$J = \mathbf{l}_1 \times \mathbf{l}_2 \cdot \hat{\mathbf{n}}. \quad (2.79)$$

We define the *unnormalized* zeroth-order GWP basis function as

$$\Lambda_\beta(\mathbf{r}) = \frac{\xi_{\beta+1}\mathbf{l}_{\beta-1} - \xi_{\beta-1}\mathbf{l}_{\beta+1}}{J}, \quad (2.80)$$

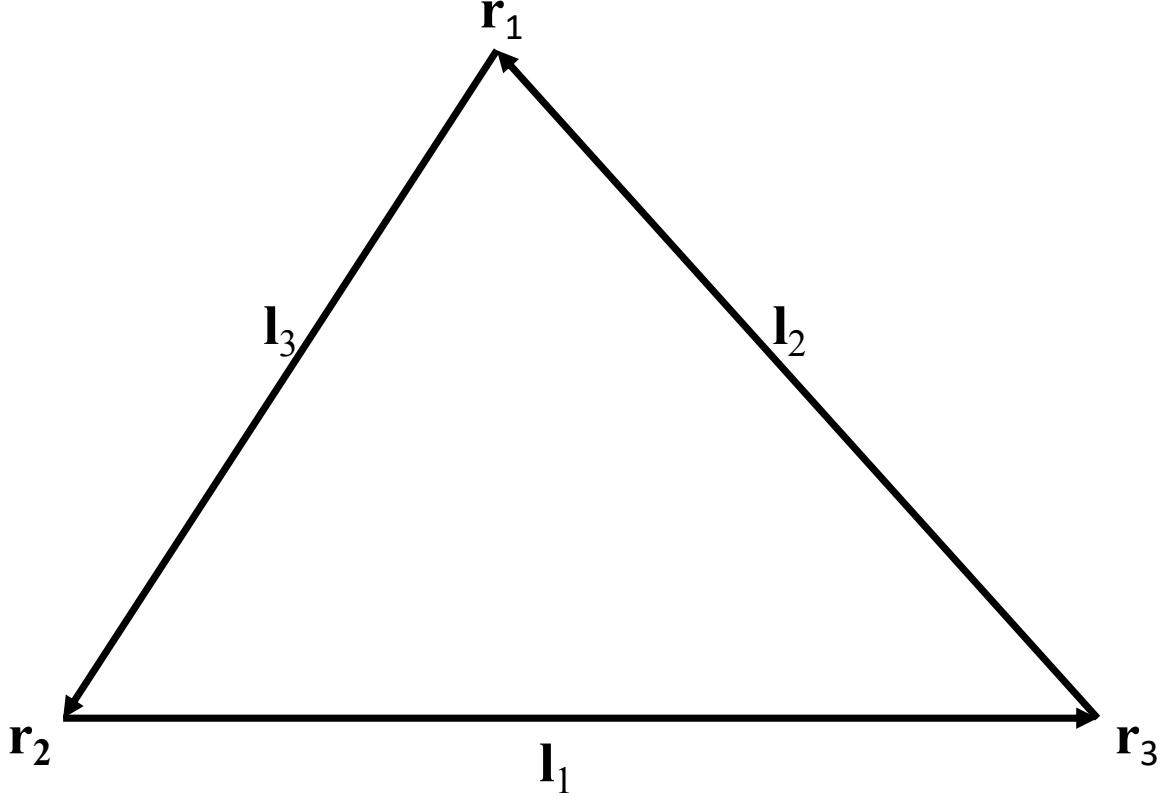


**Figure 2.3:** Edge vectors on a triangle.

for  $\beta \in \{1, 2, 3\}$  where  $J$  is the Jacobian, and indexes computations are understood cyclically, so that as  $\beta - 1 = 3$  for  $\beta = 1$  and  $\beta + 1 = 1$  for  $\beta = 3$ . (This convention for  $\beta$  will be in force for the rest of the chapter.) The “zeroth-order” means that the divergence is complete to zeroth order.

Combining this unnormalized vector basis function with the scalar shifted Silvester polynomials of (2.77), we define an  $s^{\text{th}}$ -order GWP basis function associated with the edge  $\mathbf{l}_\beta$  as

$$\mathbf{\Lambda}_\beta^{(i,j,k)}(\mathbf{r}) = N_\beta^{(i,j,k)} \frac{(s+2) \xi_\beta \hat{\alpha}_{ijk}(\mathbf{r})}{i_\beta} \mathbf{\Lambda}_\beta(\mathbf{r}). \quad (2.81)$$

Here,  $s$  must be a nonnegative integer and  $i_\beta = i$  for  $\beta = 1$ ,  $i_\beta = j$  for  $\beta = 2$ , and  $i_\beta = k$  for  $\beta = 3$ . Index  $i_\beta \in \{0, 1, \dots, p\}$ , whereas  $i_{\beta-1}, i_{\beta+1} \in \{1, 2, \dots, p+1\}$ . Of

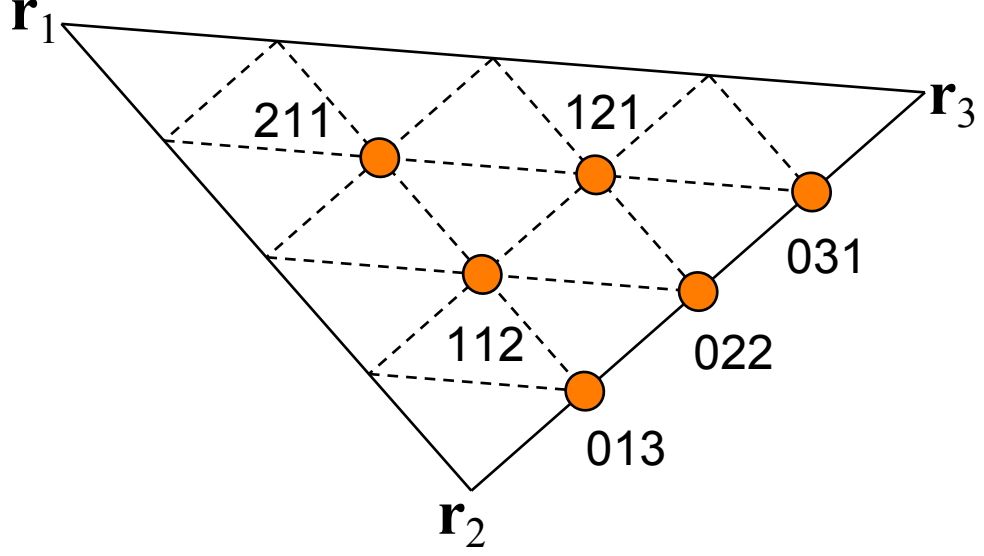


**Figure 2.4:** Interpolating nodes with a triangle for bases in which  $s = 2$  and  $\beta = 1$ .

course,  $i + j + k = s + 2$ , by the definition of  $\hat{\alpha}_{ijk}$  given in (2.77). The normalization coefficient is given by

$$N_{\beta}^{(i,j,k)} = \frac{p+2}{p+2-i_{\beta}} |\mathbf{l}_{\beta}|. \quad (2.82)$$

For bases in which  $i_{\beta} = 0$ , this coefficient assures that the component of the current normal to  $\mathbf{l}_{\beta}$  at the interpolation point is exactly one. Note also that when  $i_{\beta} = 0$ , (2.73) must be used to evaluate the basis function. Fig. 2.4 demonstrates the interpolation nodes of (2.81) on a flat triangle when  $s = 2$  respect to edge  $\mathbf{l}_1$ .

To illustrate how these GWP basis functions work on a triangle further, consider an isosceles right triangle with unit leg length in canonical Cartesian coordinate system. Assume that  $\mathbf{r}_1 = \hat{\mathbf{x}}$ , for  $\mathbf{r}_2 = \hat{\mathbf{y}}$  and  $\mathbf{r}_3 = \mathbf{0}$ , where  $\hat{\mathbf{x}}$  and  $\hat{\mathbf{y}}$  are the unit vectors along  $x$ - and  $y$ -axes, respectively. This implies immediately that  $\mathbf{l}_1 = -\hat{\mathbf{y}}$ ,  $\mathbf{l}_2 = \hat{\mathbf{x}}$ , and  $\mathbf{l}_3 = \hat{\mathbf{y}} - \hat{\mathbf{x}}$ . Hence,  $\xi_1 = x$ ,  $\xi_2 = y$ ,  $\xi_3 = 1 - x - y$ , and  $J = 1$ . The normalization coefficient  $N_3^{(0,0,1)} = \sqrt{2}$ . The zeroth-order GWP basis function associated with the hypotenuse then takes the form:

$$\Lambda_3(\mathbf{r}) = \sqrt{2}(x\hat{\mathbf{x}} + y\hat{\mathbf{y}}). \quad (2.83)$$

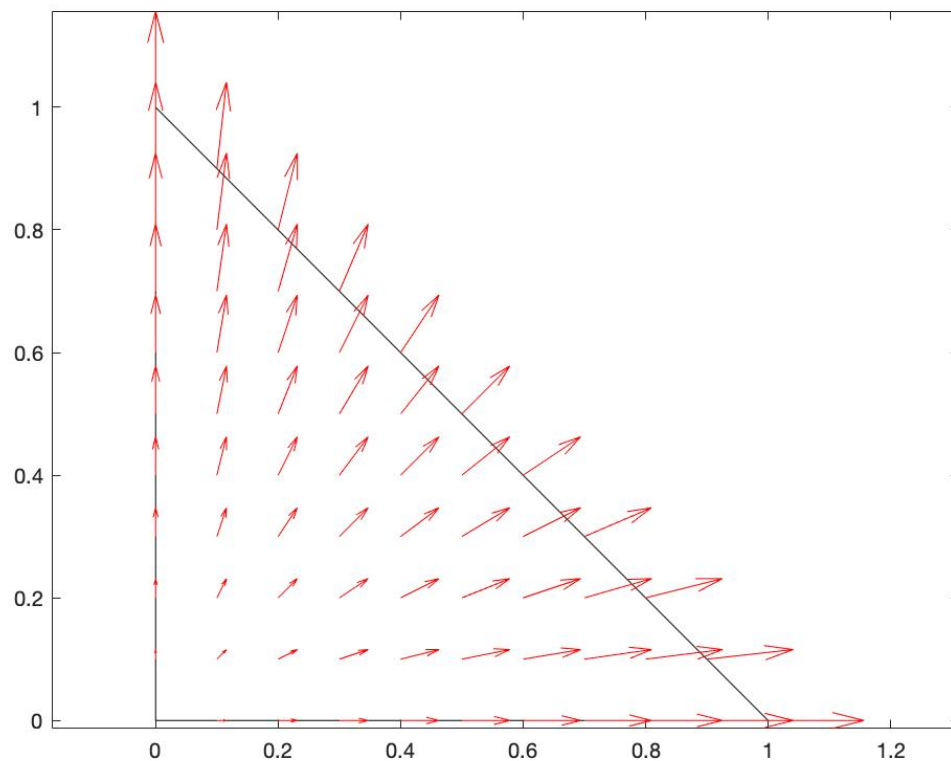


**Figure 2.5:** A zeroth-order divergence-conforming vector functions associated with the hypotenuse.

Fig. 2.5 shows the distribution of this vector function in the triangle. Note that there is no normal component along the two legs, demonstrating that no current flows out of these sides.

Similar pictures can be drawn for the other two edges. Figs. 2.6 and 2.7 show the other zeroth-order GWP bases associated with this isosceles right triangle.

Further, we want to illustrate the first-order GWP basis functions on an acute scalene triangle. Let  $\mathbf{r}_1 = \hat{\mathbf{x}} + \hat{\mathbf{y}}/10$ ,  $\mathbf{r}_2 = \hat{\mathbf{x}}/2 + \hat{\mathbf{y}}$  and  $\mathbf{r}_3 = \mathbf{0}$ . From (2.81) we know there are eight unique, linearly independent basis functions. Six of them (two per edge) interpolate currents on edges, and two interpolate components at interior nodes.

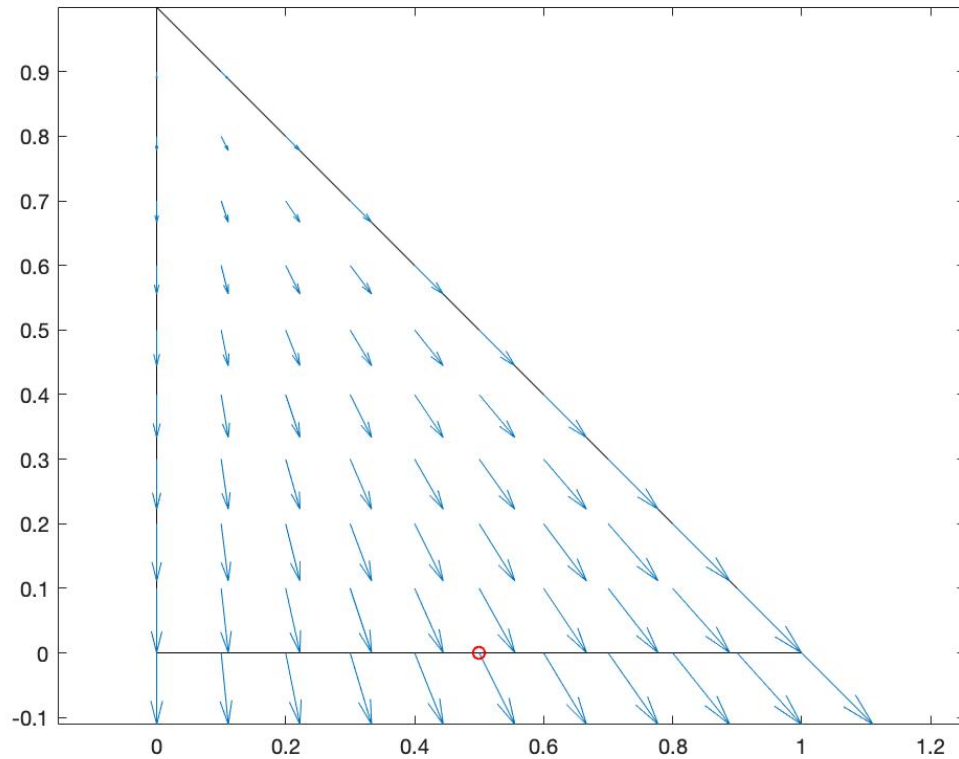


**Figure 2.6:** A zeroth-order GWP basis functions associated with the horizontal side.

Figs. 2.8 and 2.9 illustrate the two edge node bases associated with the bottom edge. The red circles show the positions of the interpolation nodes on the bottom edge.

Fig. 2.10 and Fig. 2.11 show the two bases associated with the right edge. Fig. 2.12, Fig. 2.13 show the two associated with the left edge. Note that the vectors on the edges changed their direction from flowing outward to flowing inward. This is because the dependence of each vector component on each independent variable is quadratic.

Although there is only one interior interpolation node within the triangle, there are two basis associated with it. No current flows out of the triangle in either of these bases, but there need to be two of them since the current exists on a two dimensional

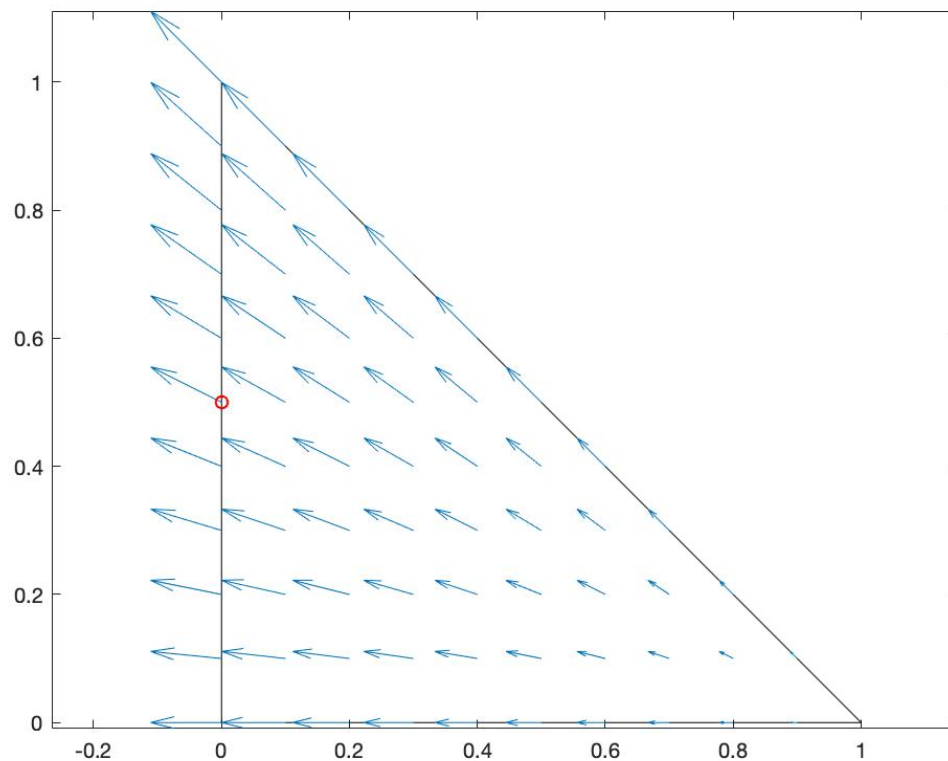


**Figure 2.7:** A zeroth-order GWP basis functions associated with the vertical side.

manifold. Figs. 2.14 and 2.15 show these two functions.

With proper modification, these interpolatory basis functions can be developed on other 2-D or 3-D elements and curvilinear elements. They can also be modified into “curl-conforming” forms to model fields for use in the finite element method [19].

### 2.3 Temporal Discretization

In this section, we describe how the spatially discretized equations are discretized in time. The temporal discretization schemes are demonstrated through application to PEC scattering. A similar analysis can be applied to dielectric scatters.

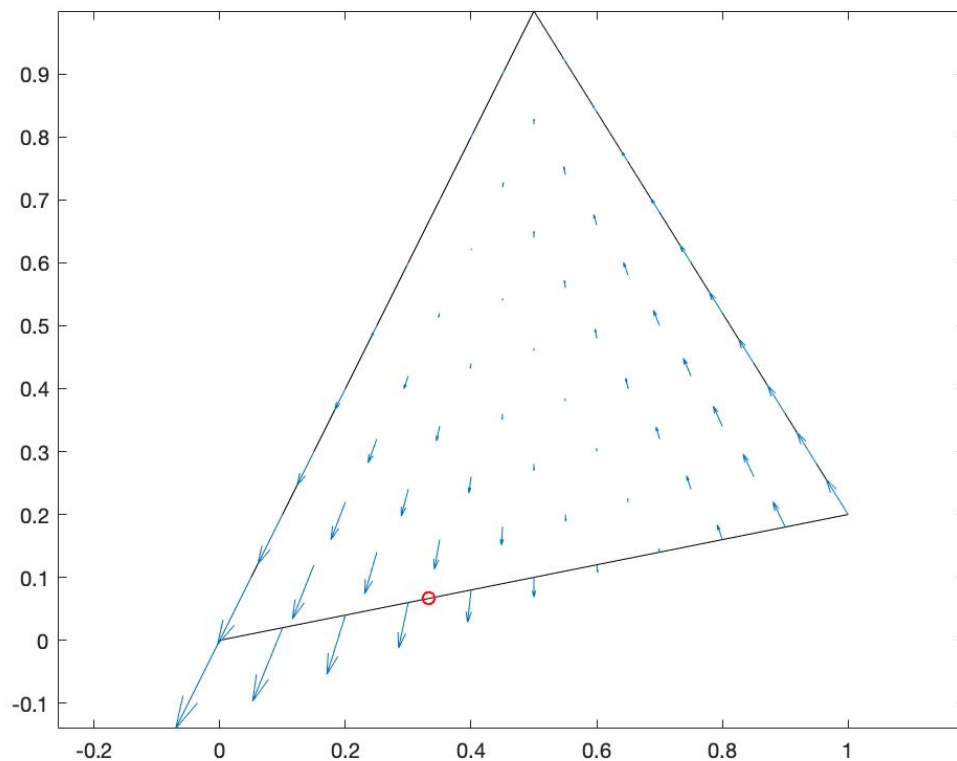


**Figure 2.8:** A first-order GWP basis function interpolating a node on the bottom edge.

### 2.3.1 Convolution Quadrature Method

One method of discretizing any TDIE in time is convolution quadrature (CQ), which we illustrate with the TD-EFIE. The process is based on the continuous time Laplace transform and the discrete time  $\mathcal{Z}$ -transform. Given a function  $f(t)$ , its Laplace transform  $\tilde{f}(s)$  can be computed from

$$\tilde{f}(s) = \int_0^{\infty} f(t)e^{-st} dt. \quad (2.84)$$

Given this formula, multiplication of the Laplace transform of a function by the Laplace parameter  $s$  gives rise to time-domain differentiation [30]. The (two-sided)  $\mathcal{Z}$ -transform

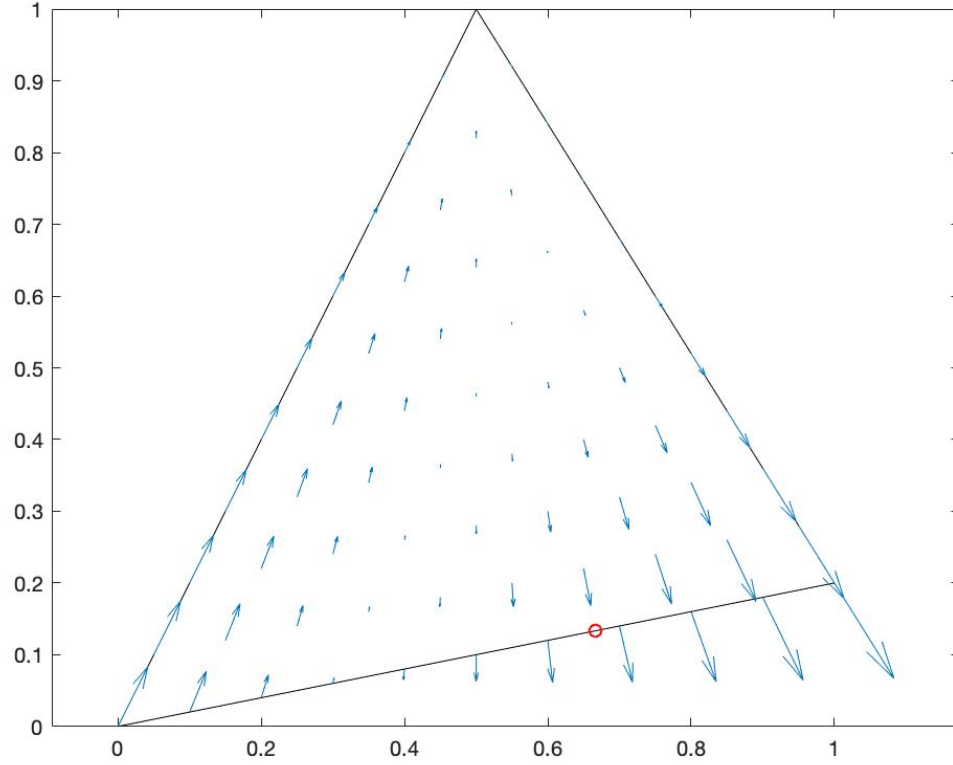


**Figure 2.9:** A first-order GWP basis function interpolating a node on the bottom edge.

of a series  $x_k$ ,  $k = \dots, -1, 0, 1, \dots$  is given by

$$X(z) = \sum_{k=-\infty}^{\infty} x_k z^{-k}, \quad (2.85)$$

for whatever values of the parameter  $z$  the sum converges [36]. From this, one can easily show that multiplication by  $z^{-1}$  in the  $\mathcal{Z}$ -domain is tantamount to a single step delay, and that the original series can be recovered from the  $\mathcal{Z}$ -transform using residue theory [10, 36] via the integral

$$x_k = \frac{1}{2\pi j} \oint_C X(z) z^{k-1} dz \quad (2.86)$$

where  $C$  is any contour enveloping the origin.

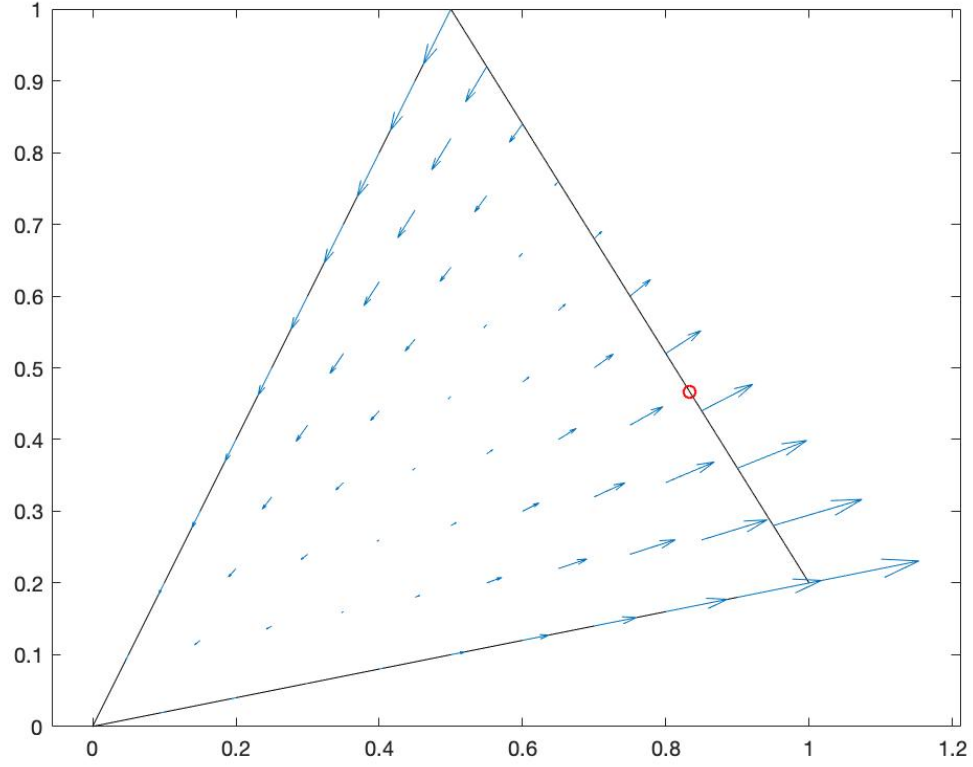


**Figure 2.10:** A first-order GWP basis function interpolating a node on the right edge.

The discretization begins by computing the Laplace transform of Equation (2.53), resulting in

$$\begin{aligned}
 s\tilde{\mathbf{E}}^{\text{inc}}(\mathbf{r}, s) &= \frac{s^2\mu_0}{4\pi} \iint_S \tilde{\mathbf{J}}(\mathbf{r}', s) \frac{e^{-j\frac{s|\mathbf{r}-\mathbf{r}'|}{c}}}{|\mathbf{r}-\mathbf{r}'|} d\mathbf{r}' \\
 &\quad - \frac{1}{4\pi\epsilon_0} \iint_S \nabla' \cdot \tilde{\mathbf{J}}(\mathbf{r}', s) \frac{e^{-j\frac{s|\mathbf{r}-\mathbf{r}'|}{c}}}{|\mathbf{r}-\mathbf{r}'|} d\mathbf{r}'.
 \end{aligned} \tag{2.87}$$

This equation can be discretized in space using the usual MoM approximation

$$\tilde{\mathbf{J}}(\mathbf{r}, s) = \sum_{n=0}^{N_s} \tilde{I}_n(s) \mathbf{S}_n(\mathbf{r}), \tag{2.88}$$

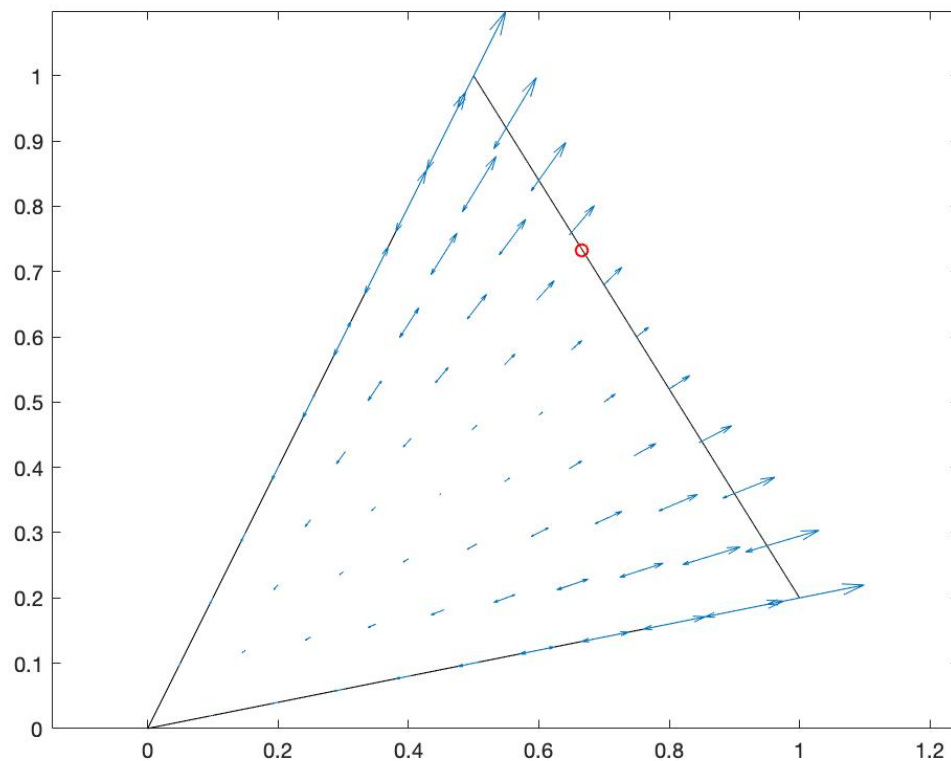


**Figure 2.11:** A first-order GWP basis function interpolating a node on the right edge.

where  $N_s$  is the number of spatial bases used for the discretization. The spatial basis functions  $\mathbf{S}_n(\mathbf{r})$  used here are GWP bases described in the last section. Our implementation also uses the GWP basis functions as testing functions, so the equation resulting from the substitution of (2.88) into (2.87) is tested in space by multiplying it by the  $\mathbf{S}_m(\mathbf{r})$  for  $m = 1, \dots, N_s$  and integrating over  $S$ .

Motivated by the observation that direct differentiation in the time domain transforms into multiplication by the Laplace parameter  $s$  in the Laplace domain, we replace  $s$  with a finite difference approximation in the  $\mathcal{Z}$ -domain [59]. A first-order backward difference (or Backward Euler (BE)) approximation to  $s$  is

$$s = \frac{1 - z^{-1}}{\Delta t}, \quad (2.89)$$

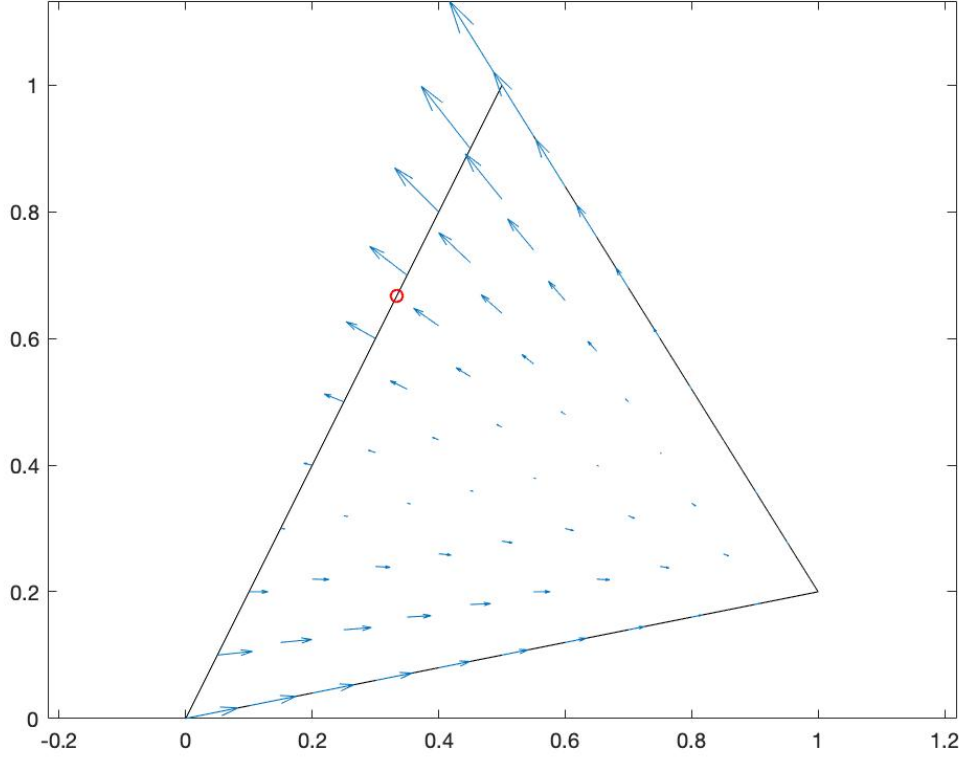


**Figure 2.12:** A first-order GWP basis function interpolating a node on the left edge.

and a second-order backward difference formula (BDF2) is given by

$$s = \frac{3 - 4z^{-1} + z^{-2}}{2\Delta t}. \quad (2.90)$$

This process results in a simple algebraic equation depending on  $z$ . By computing the inverse  $\mathcal{Z}$ -transform of this equation (which can even be done efficiently numerically using Equation (2.86); see [59]) we finally arrive at a set of equations for the currents in the discrete time domain. Denoting the current at time  $i\Delta t$  on spatial basis function  $n$  by  $I_{ni}$ , and the set of all  $N_s$  currents at time step  $i$  by the vector  $\mathbf{I}_i$ , we finally find

$$\mathbf{Z}_0 \mathbf{I}_i = \mathbf{V}_i - \sum_{j=0}^{i-1} \mathbf{Z}_{i-j} \mathbf{I}_j, \quad (2.91)$$

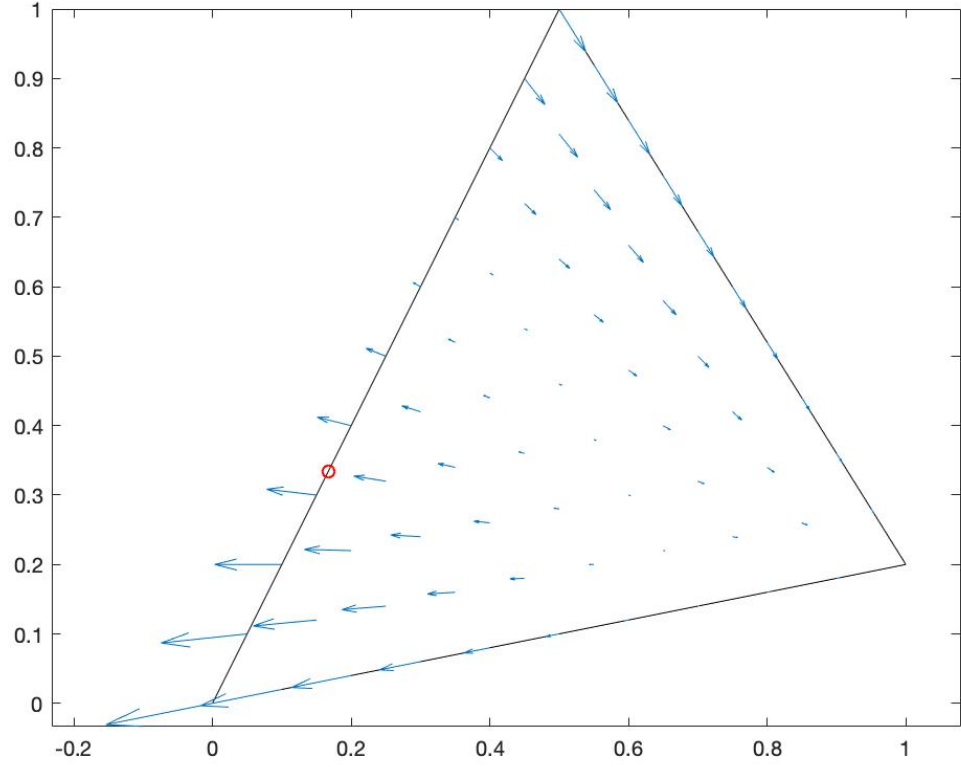


**Figure 2.13:** A first-order GWP basis function interpolating a node on the left edge.

which can be solved iteratively for the currents by MoT. The computational complexity of MoT is  $O(N_t N_s^2)$  since the length of kernel  $\mathbf{Z}$  in (2.91) is determined only by the geometry size of the scatterer, the wave speed in the medium, and the length of time step  $\Delta t$ . The elements of the vectors  $\mathbf{V}_i$  are given by

$$[\mathbf{V}_i]_n = \iint_S \dot{\mathbf{E}}^{\text{inc}}(\mathbf{r}, i\Delta t) \mathbf{S}_n(\mathbf{r}) d\mathbf{r}, \quad (2.92)$$

where  $\dot{\mathbf{E}}^{\text{inc}}(\mathbf{r}, t)$  is the derivative of the incident field with respect to time. If BDF2 is

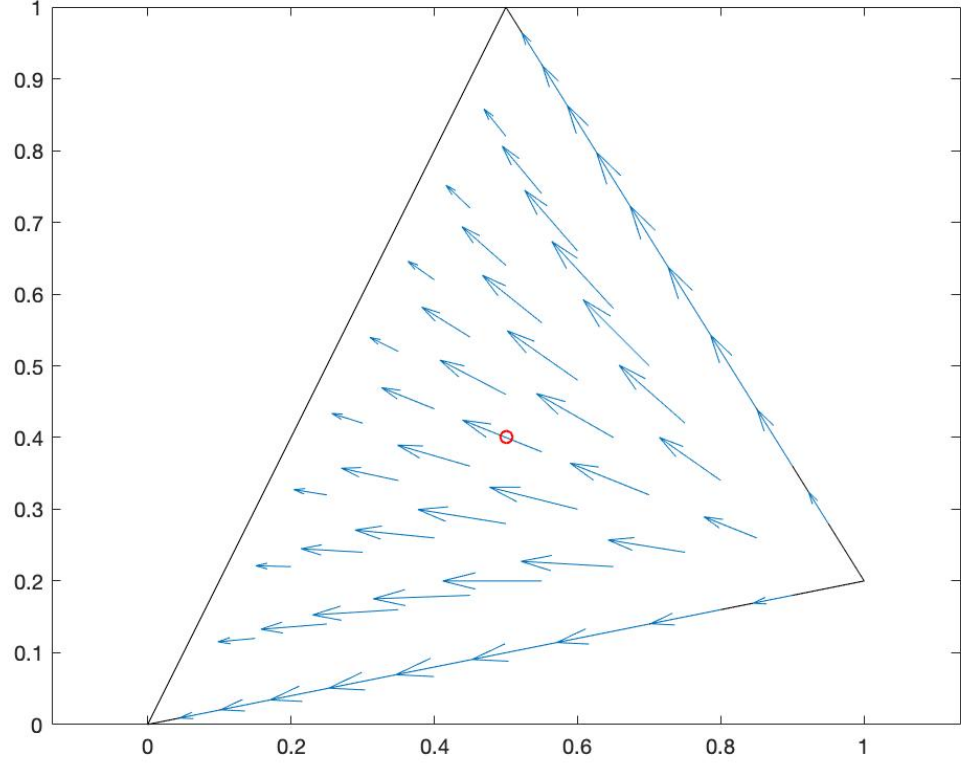


**Figure 2.14:** A first-order GWP basis function interpolating a node within a triangle.

chosen for the temporal discretization, the elements of the matrices  $\mathbf{Z}_k$  are given by

$$\begin{aligned}
 [\mathbf{Z}_k]_{mn} = & \iint_S \iint_S \frac{\mu_0 \mathbf{S}_m(\mathbf{r}) \cdot \mathbf{S}_n(\mathbf{r}')}{4\pi |\mathbf{r} - \mathbf{r}'|} \beta_k(|\mathbf{r} - \mathbf{r}'|) d\mathbf{r}' d\mathbf{r} \\
 & - \iint_S \iint_S \frac{\nabla \cdot \mathbf{S}_m(\mathbf{r}) \nabla' \cdot \mathbf{S}_n(\mathbf{r}')}{4\pi\epsilon_0 |\mathbf{r} - \mathbf{r}'|} \alpha_k(|\mathbf{r} - \mathbf{r}'|) d\mathbf{r}' d\mathbf{r}. \quad (2.93)
 \end{aligned}$$

In this equation,

$$\alpha_k(t) = \frac{1}{k!} \left(\frac{t}{2}\right)^{\frac{k}{2}} e^{-\frac{3}{2}t} H_k(\sqrt{2t}) \quad (2.94)$$

for  $k \geq 0$ ,  $\alpha_k = 0$  for  $k < 0$ ,  $H_k(\cdot)$  is the  $k^{\text{th}}$  order Hermite polynomial, and

$$\beta_k(t) = \frac{\alpha_{k-4} - 8\alpha_{k-3} + 22\alpha_{k-2} - 24\alpha_{k-1} + 3\alpha_k}{4(\Delta t)^2}. \quad (2.95)$$

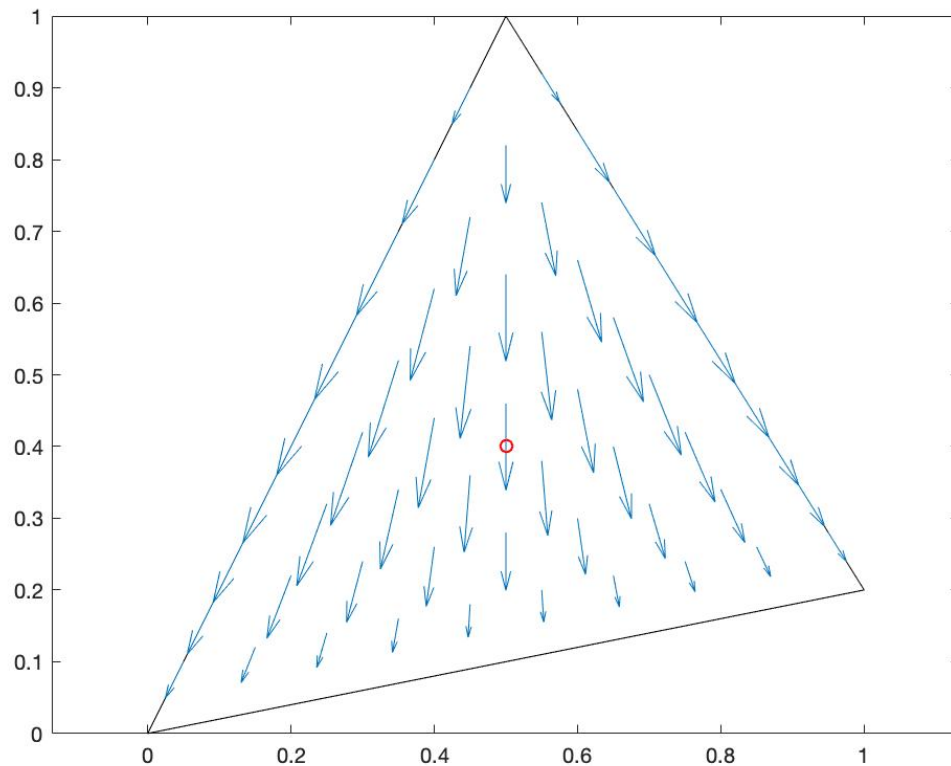


**Figure 2.15:** A first-order GWP basis function interpolating a node within a triangle.

(Of course, in all of these equations, variables with negative indices may be taken to vanish.)

The temporal discretization in CQ is achieved by substituting the  $s$  variable with a function of  $z$  variable to get the equations in  $z$  domain and subsequently taking the inverse  $z$ -transform. We know that stable continuous functions have poles only in the left half of the  $s$ -plane, and respectively in the interior of the unit circle in the  $z$ -plane. So a substitution for  $s$  can be A-stable if it maps the left half  $s$ -plane into the unit circle in the  $z$ -plane. (Here, A-stable is mathematical jargon for stable for all complex frequencies of excitation, hence the claim.) BE and BDF 2 are A-stable and they automatically preserve system stability. But BDF2 is unfortunately the highest

order stable discretization of this form possible, since any rational  $s$  to  $z$  mapping of order greater than two isn't A-stable as shown by Dahlquist [12]. Higher order different A-stable substitution for  $s$  in terms of  $z$  are only possible by invoking Runge-Kutta methods [58].

To develop a substitution for  $s$  using a Runge-Kutta method, we first show how such methods are used to solve ordinary differential equations. Consider the canonical first order ordinary differential equation

$$\frac{dx(t)}{dt} = f(t, x(t)). \quad (2.96)$$

By integrating both sides between a fixed time  $t_0$  and a variable point  $t$ , we derive

$$x(t) = x(t_0) + \int_{t_0}^t f(\tau, x(\tau)) d\tau. \quad (2.97)$$

Assuming  $t_0 = n\Delta t$  and  $t = (n+1)\Delta t$  for a non-negative integer  $n$ , we can re-write the equation above as

$$x_{n+1} = x_n + \int_{t_0}^t f(\tau, x(\tau)) d\tau, \quad (2.98)$$

where  $x_{n+1} = x((n+1)\Delta t)$ , and  $x_n = x(n\Delta t)$ . The integral on the right hand side can be done numerically by some predetermined quadrature technique. We define  $p$  interpolation nodes  $t_{nj} = n\Delta t + d_j\Delta t$  for  $j = 1, \dots, p$  on the interval  $[t_n, t_{n+1}]$ , where  $d_j$  is the position of the  $j^{\text{th}}$  interpolation node of the quadrature rule on the interval  $[0, 1]$ . Denote the  $p^{\text{th}}$ -order Lagrange interpolation polynomial on interval  $n$  that has vanishes at the  $p-1$  quadrature nodes excluding node  $j$  by  $P_{nj}$ . The integrand  $f(t, x(t))$  can then be approximated by the interpolation

$$f(t, x(t)) = \sum_{j=1}^p f(t_{nj}, h_{nj}) P_{nj}(t), \quad (2.99)$$

where  $h_{nj} = x(t_{nj})$  is the value of  $x$  at the  $j^{\text{th}}$  interpolation node. Since  $f(t, x(t))$  is approximated by a Lagrange interpolation polynomial, at a given interpolation node  $i$  we have

$$h_{ni} = x_n + \Delta t \sum_{j=1}^p a_{ij} f(t_{nj}, h_{nj}), \quad (2.100)$$

where

$$a_{ij} = \frac{1}{\Delta t} \int_{t_n}^{t_{ni}} P_{nj}(\tau) d\tau. \quad (2.101)$$

Applying this equation on all of the  $p$  interpolation nodes leads to a set of equations taking the form

$$\mathbf{h}_n = \mathbf{1}x_n + \Delta t \mathbf{A} \mathbf{f}_n, \quad (2.102)$$

where  $\mathbf{1}$  is a  $p$ -vector of all ones,  $\mathbf{h}_n^T = [h_{n1}, \dots, h_{np}]$ ,  $\mathbf{f}_n^T = [f(t_{n1}, h_{n1}), \dots, f(t_{np}, h_{np})]$ , and  $\mathbf{A}$  is a  $p \times p$  matrix whose elements are the  $a_{ij}$ . Note that in general, these are non-linear, transcendental equations, since  $\mathbf{f}_n$  is an arbitrary function of  $\mathbf{h}_n$ . Assuming we can solve these equations for  $f_{nj}$  with  $j = 1, \dots, p$ , we can compute the approximation of  $x_{n+1}$  as

$$x_{n+1} = x_n + \Delta t \sum_{j=1}^p b_j f(t_{nj}, h_{nj}), \quad (2.103)$$

where

$$b_j = \frac{1}{\Delta t} \int_{t_n}^{t_{n+1}} P_{nj}(\tau) d\tau. \quad (2.104)$$

We can write this equation more succinctly as

$$x_{n+1} = x_n + \Delta t \mathbf{b}^T \mathbf{f}_n, \quad (2.105)$$

where the vector  $\mathbf{b}$  contains the  $b_j$  above.

The method described above is a  $p$ -stage Runge-Kutta method. If  $a_{ij} = 0$  for  $i \geq j$  it is called an *explicit* Runge-Kutta method, otherwise, it is called an *implicit* Runge-Kutta method. Note that explicit Runge-Kutta methods are never A-stable.

To describe a particular Runge-Kutta method, the coefficients in the vector  $\mathbf{b}$  and the matrix  $\mathbf{A}$ , as well as the interpolation node positions  $d_j$  can be arranged into an array called a Butcher Tableau as

	$\mathbf{d}$	$\mathbf{A}$
		$\mathbf{b}^t$

where  $\mathbf{d}^T = [d_1, \dots, d_p]$ . The common 4th order 4-stage Runge-Kutta method is often called “the” Runge-Kutta method, has a Butcher Tableau given by

0	0	0	0	0
1/2	1/2	0	0	0
1/2	0	1/2	0	0
1	0	0	1	0
	1/6	1/3	1/3	1/6

The Radau IIA method is an implicit Runge-Kutta method which uses Radau quadrature rules to determine the position vector  $\mathbf{d}$ . Radau rules are a type of Gaussian integration rule incorporating one endpoint as an integration node; i.e.,  $d_p = 1$  and  $h_{np} = x_{n+1}$ . A Butcher Tableau for a 2-stage Radau IIA rule is

1/3	5/12	-1/12
1	3/4	1/4
	3/4	1/4

A Butcher Tableau for a 3-stage Radau IIA takes the following form:

$\frac{4-\sqrt{6}}{10}$	$\frac{88-7\sqrt{6}}{360}$	$\frac{296-169\sqrt{6}}{1800}$	$-\frac{2-3\sqrt{6}}{225}$
$\frac{4+\sqrt{6}}{10}$	$\frac{296+169\sqrt{6}}{1800}$	$\frac{88+7\sqrt{6}}{360}$	$-\frac{2+3\sqrt{6}}{225}$
1	$\frac{16-\sqrt{6}}{360}$	$\frac{16+\sqrt{6}}{360}$	$\frac{1}{9}$
	$\frac{16-\sqrt{6}}{360}$	$\frac{16+\sqrt{6}}{360}$	$\frac{1}{9}$

To use all of this information about Runge-Kutta methods for CQ, we need to create an approximation to the Laplace parameter  $s$  as a function of the  $\mathcal{Z}$ -domain  $z$ . To do this, we start with the differential equation

$$\frac{dx}{dt} = sx, \tag{2.106}$$

which succinctly encodes the idea that differentiation in the time domain is multiplication by  $s$  in the Laplace domain. Applying our Runge-Kutta method to this special differential equation yields

$$\mathbf{H}(z) = \mathbf{1}X_n(z) + s\Delta t\mathbf{A}\mathbf{H}(z), \text{ and} \tag{2.107}$$

$$zX(z) = X(z) + s\Delta t\mathbf{b}^T\mathbf{H}(z). \tag{2.108}$$

Solving the system equations for  $s\mathbf{H}(z)$  yields

$$s\mathbf{H}(z) = \frac{1}{\Delta t} \left( \mathbf{A} + \frac{\mathbf{1} \cdot \mathbf{b}^T}{z-1} \right)^{-1} \mathbf{H}(z) \quad (2.109)$$

Because the vector  $\mathbf{h}$  merely contains values of the unknown function  $x$ , we derive the following substitution for  $s$ :

$$s = \frac{1}{\Delta t} \left( \mathbf{A} + \frac{\mathbf{1} \cdot \mathbf{b}^T}{z-1} \right)^{-1}. \quad (2.110)$$

CQ only requires the knowledge of the convolution kernel (Green's functions) in the frequency domain, and gives rise to stable approximations under easily tested conditions. For some arbitrarily dispersive materials such as Debye materials, it is difficult to directly get their time convolution kernels in time domain, yet their frequency domain green functions are well defined. CQ works easily for such dispersive media, unlike other methods such as BLIF (described in the next section and MoD [11] do not.

### 2.3.2 Bandlimited Interpolation Function Method

Unlike CQ, the bandlimited interpolation function (BLIF) method of temporal discretization is a Petrov-Galerkin method; that is, it uses temporal basis functions and a testing process [60]. The basis functions used (the BLIFs themselves) are very smooth to ensure that spatial integration can be carried out accurately without locating the boundary of the illuminated region. This degree of smoothness, however, ensures that the BLIFs cannot be causal, complicating a straightforward description of the method. We therefore review the method here.

Given any temporal basis function  $T(t)$ , a Petrov-Galerkin method begins by discretizing the current as

$$\tilde{\mathbf{J}}(\mathbf{r}, t) = \sum_{j=1}^{N_t} \sum_{n=0}^{N_s} I_{jn} T(t - j\Delta t) \mathbf{S}_n(\mathbf{r}) \quad (2.111)$$

where the  $I_{jn}$  are the unknown basis function weighting coefficients. As before, we let  $N_s$  denote the total number of spatial basis functions, and discretize time into  $N_t$  time

steps of duration  $\Delta t$ . With these definitions in place, the matrices  $\mathbf{Z}_k$  resulting from the discretization of the TD-EFIE in (2.91) can be written as

$$[\mathbf{Z}_k]_{mn} = \iint_S \iint_S \frac{\mu_0 \mathbf{S}_m(\mathbf{r}) \cdot \mathbf{S}_n(\mathbf{r}')}{4\pi |\mathbf{r} - \mathbf{r}'|} \ddot{T} \left( k\Delta t - \frac{|\mathbf{r} - \mathbf{r}'|}{c_0} \right) d\mathbf{r}' d\mathbf{r} \\ - \iint_S \iint_S \frac{\nabla \cdot \mathbf{S}_m(\mathbf{r}) \nabla' \cdot \mathbf{S}_n(\mathbf{r}')}{4\pi \epsilon_0 |\mathbf{r} - \mathbf{r}'|} T \left( k\Delta t - \frac{|\mathbf{r} - \mathbf{r}'|}{c_0} \right) d\mathbf{r}' d\mathbf{r}. \quad (2.112)$$

For temporal basis functions, we use the eponymous BLIFs, which are formulated in terms of the approximate prolate spheroidal wave functions (APSWFs) of Knab [29]. These functions were designed to interpolate a function bandlimited to an angular frequency  $\omega_0$ , and sampled with a time step less than the Nyquist step  $\pi/\omega_0$ . Defining the time step

$$\Delta t = \frac{\pi}{\psi \omega_0}, \quad (2.113)$$

in terms of an oversampling rate  $\psi > 1$ , the BLIFs have the form

$$T(t) = \frac{\sin(\psi \omega_0 t)}{\psi \omega_0 t} \frac{\sin[a \sqrt{(\frac{t}{N\Delta t})^2 - 1}]}{\sinh(a) \sqrt{(\frac{t}{N\Delta t})^2 - 1}}, \quad (2.114)$$

$N$  is the *APSWF (half-)width parameter*, so-called because the function has approximate temporal support over an interval of length  $(2N + 1)\Delta t$ , and  $a = \pi N \Delta t$  is called the *time-bandwidth* product of the APSWF.

These functions are chosen for the numerical representation of currents for a number of cogent reasons: First, they are interpolatory; that is,  $T(k\Delta t) = 0$  for all nonzero integers  $k$ , and  $T(0) = 1$ . They are also bandlimited to a highest angular frequency  $(2\psi - 1)\omega_0$ , ensuring that the radiation produced by the discretized currents is bandlimited as well. Most importantly, they were concocted to efficiently represent bandlimited functions through their samples [29]. Specifically, given a function  $f(t)$  bandlimited to  $\omega_0$  and bounded in amplitude by a value  $M$ , a BLIF interpolant has the property

$$\left| f(t) - \sum_{k=-N}^N f(k\Delta t) T(t - k\Delta t) \right| \leq \frac{M}{\sinh(a)}, \quad (2.115)$$

for  $2|t| \leq \Delta t$ . From (2.115) we see the interpolation provided by APSWFs has an exponential convergence so long as the proper number of contributing terms is retained, which means a truncation at  $|t| > (N + 0.5)\Delta t$  will not significantly effect the resulting interpolation.

Unfortunately, the use of BLIFs as temporal basis functions destroys the causality which ensures the MoT algorithm works properly. Specifically, because the BLIFs do not vanish for  $t \leq -\Delta t$ , (2.91) takes the form

$$\sum_{j=0}^N \mathbf{Z}_{-j} \mathbf{I}_{i+j} = \mathbf{V}_i - \sum_{j=0}^{i-1} \mathbf{Z}_{i-j} \mathbf{I}_j. \quad (2.116)$$

This equation makes MoT impossible, since the values of currents at future times  $(i + j)\Delta t, j = 0, 1, \dots, N$ , are required just to find the current “right now” at timestep  $i\Delta t$ .

An extrapolation technique must therefore be used to predict the future currents based on the present and past currents. Given values of a bandlimited function  $f(t)$  at times  $(1 - N_{\text{samp}})\Delta t, (2 - N_{\text{samp}})\Delta t, \dots, 0$ , we create rules to extrapolate the values  $f(\Delta t), f(2\Delta t), \dots, f(N\Delta t)$  with the formula

$$f(j\Delta t) \approx \sum_{i=1-N_{\text{samp}}}^0 h_j^i f(i\Delta t). \quad (2.117)$$

The  $h_j^i$  are found by ensuring that the rule extrapolates sinusoids at multiples of a frequency  $\Delta\omega = \omega_0/N_\omega$  by solving the system of equations

$$\sum_{i=1-N_{\text{samp}}}^0 h_j^i \exp(\sqrt{-1}ik\Delta\omega\Delta t) = \exp(\sqrt{-1}jk\Delta\omega\Delta t) \quad (2.118)$$

for  $j = 0, 1, \dots, N$  and  $k = -N_\omega, \dots, N_\omega$  in a least squares sense.

With this extrapolation scheme, we can write all needed future currents in terms of past currents, which allows us to rewrite (2.116) as

$$\tilde{\mathbf{Z}}_0 \mathbf{I}_i = \mathbf{V}_i - \sum_{j=0}^{i-1} \tilde{\mathbf{Z}}_{i-j} \mathbf{I}_j, \quad (2.119)$$

where the  $\tilde{\mathbf{Z}}_k$ s are given by

$$\tilde{\mathbf{Z}}_k = \begin{cases} \mathbf{Z}_k + \sum_{p=1}^N h_p^{-k} \mathbf{Z}_{-p}, & 0 \leq k \leq N_{\text{samp}} - 1. \\ \mathbf{Z}_k, & k \geq N_{\text{samp}}. \end{cases} \quad (2.120)$$

Therefore, the capability to march on in time is recovered. The accuracy of this extrapolation is excellent as it is shown in [60].

## 2.4 Other Related Numerical Algorithms

A few more mathematical techniques are used in the remainder of this thesis to produce numerical results. In particular, both nonsingular and singular integrals must be computed. Also, for large problems, special numerical techniques must be employed to reduce the computational complexity of the standard MoM or MoT algorithms. Finally, to actually do the work proposed here, adaptive quadratures must be used, so that accuracy of element computation can be finely controlled. These techniques are discussed in this section.

### 2.4.1 Gaussian Quadrature for One Dimension

Consider the following integral:

$$\mathbf{I}f = \int_a^b f(x) dx. \quad (2.121)$$

In building a numerical quadrature formula, we assume the integral can be approximated by

$$\mathbf{I}f \approx \sum_{i=1}^N w_i f(x_i). \quad (2.122)$$

Numerical quadrature rules differ in the choice of weights  $w_i$  and the abscissas  $x_i$  that optimize the procedure for functions with different properties. Gaussian quadrature (specifically *Gauss-Legendre quadrature*) chooses the weights  $w_i$  and the abscissas  $x_i$  in such a way that the estimate is exact for polynomials up to degree  $2N - 1$ . (We choose order  $2N - 1$  since it is defined by exactly  $2N$  coefficients, and we have  $2N$  parameters at our disposal in the weights and nodes.) [28]

For instance, consider an integral of a polynomial of degree 3 over the interval  $[-1, 1]$ . Because of the symmetry of this problem, we denote the two nodes as  $x_{-1}$  and  $x_1$ , and the two weights as  $w_{-1}$  and  $w_1$ . Now, the polynomial can be written in general as

$$f(x) = ax^3 + bx^2 + cx + d. \quad (2.123)$$

Using our integration rule on (2.123), we must have

$$\begin{aligned} \int_{-1}^1 ax^3 + bx^2 + cx + d = & a(w_{-1}x_{-1}^3 + w_1x_1^3) + b(w_{-1}x_{-1}^2 + w_1x_1^2) \\ & + c(w_{-1}x_{-1} + w_1x_1) + d(w_{-1} + w_1). \end{aligned} \quad (2.124)$$

The closed-form result is

$$\int_{-1}^1 (ax^3 + bx^2 + cx + d) dx = \frac{2}{3}b + 2d. \quad (2.125)$$

The odd terms in (2.123) vanish on integration over our symmetric interval, so the closed-form result has only two terms. To eliminate all the terms associated with  $a$  and  $c$  in (2.124), we let  $w_{-1} = w_1$  and  $x_{-1} = -x_1$ . Thus (2.124) becomes

$$2w_1 (bx_1^2 + d) = \frac{2}{3}b + 2d. \quad (2.126)$$

Equating coefficients of  $b$  and  $d$  gives:

$$\frac{2}{3} = 2w_1x_1^2, \text{ and} \quad (2.127)$$

$$2 = 2w_1. \quad (2.128)$$

Solving these equations results in the two point integration rule for this interval:

$$w_{-1} = w_1 = 1 \quad (2.129)$$

$$x_1 = -x_{-1} = \sqrt{\frac{1}{3}}. \quad (2.130)$$

Thus with only two samples, this quadrature rule can exactly integrate a polynomial of degree 3.

In practice, high-order rules are developed by using orthogonal polynomials. (In this case, the orthogonal polynomials used are the Legendre polynomials of mathematical physics, hence Gauss-Legendre.) Tables of weights and samples of various orders can be found online and in many textbooks on numerical analysis [28].

### 2.4.2 Gaussian Quadrature for Triangles

Gaussian quadrature can be developed specifically for multidimensional integrals in a similar way. For a triangular region, consider the following integrand:

$$f(\xi_1, \xi_2) = a\xi_1^2 + b\xi_2^2 + c\xi_1\xi_2 + d\xi_1 + e\xi_2 + f. \quad (2.131)$$

Here  $\xi_1$  and  $\xi_2$  are the two linearly independent area coordinates of the dependent triumvirate  $(\xi_1, \xi_2, \xi_3)$  in the triangle. Note that  $\xi_1 + \xi_2 + \xi_3 = 1$ . Substituting (2.131) into (2.122) yields

$$\sum_{i=1}^N w_i f(\xi_{1i}, \xi_{2i}, \xi_{3i}) = A \left[ a \sum_{i=1}^N w_i \xi_{1i}^2 + b \sum_{i=1}^N w_i \xi_{2i}^2 + c \sum_{i=1}^N w_i \xi_{1i} \xi_{2i} + d \sum_{i=1}^N w_i \xi_{1i} + e \sum_{i=1}^N w_i \xi_{2i} + f \sum_{i=1}^N w_i \right] \quad (2.132)$$

where  $A$  is the area of the triangle. On the other hand, the analytic result takes the form:

$$\int_A f(\xi_1, \xi_2) = \frac{1}{6}aA + \frac{1}{6}bA + \frac{1}{12}cA + \frac{1}{3}dA + \frac{1}{3}eA + fA. \quad (2.133)$$

More specifically, for each term in (2.131), we have

$$\iint dA = A \quad (2.134)$$

$$\iint \xi_1 dA = \iint \xi_2 dA = \frac{1}{3}A \quad (2.135)$$

$$\iint \xi_1^2 dA = \iint \xi_2^2 dA = \frac{1}{6}A \quad (2.136)$$

$$\iint \xi_1 \xi_2 dA = \frac{1}{12}A. \quad (2.137)$$

By equating (2.132) with (2.133), we

$$1 = \sum_{i=1}^N w_i \tag{2.138}$$

$$\frac{1}{3} = \sum_{i=1}^N w_i \xi_{1i} = \sum_{i=1}^N w_i \xi_{2i} \tag{2.139}$$

$$\frac{1}{6} = \sum_{i=1}^N w_i \xi_{1i}^2 = \sum_{i=1}^N w_i \xi_{2i}^2 \tag{2.140}$$

$$\frac{1}{12} = \sum_{i=1}^N w_i \xi_{1i} \xi_{2i}. \tag{2.141}$$

We can solve at most four unknowns from these four equations. We apply triangular symmetry on the sample points and weights to produce one weight  $w$  and three sample points associated with it. These points are symmetrically located on the triangle, and must therefore have a coordinate pattern of the form  $(M, N, N)$ ,  $(N, M, N)$  and  $(N, N, M)$ . So the first three of the four equations above can be simplified to read

$$1 = 3w, \tag{2.142}$$

$$\frac{1}{3} = wM + 2wN, \text{ and} \tag{2.143}$$

$$\frac{1}{6} = wM^2 + 2wN^2. \tag{2.144}$$

$$\tag{2.145}$$

By solving these equations, we obtain the two coordinate unknowns and the weight as

$$w = \frac{1}{3}, \tag{2.146}$$

$$M = \frac{2}{3}, \text{ and} \tag{2.147}$$

$$N = \frac{1}{6}. \tag{2.148}$$

The three sample points are thus

$$(M, N, N) = \left( \frac{2}{3}, \frac{1}{6}, \frac{1}{6} \right), \quad (2.149)$$

$$(N, M, N) = \left( \frac{1}{6}, \frac{2}{3}, \frac{1}{6} \right), \text{ and} \quad (2.150)$$

$$(N, N, M) = \left( \frac{1}{6}, \frac{1}{6}, \frac{2}{3} \right). \quad (2.151)$$

Unlike one-dimensional cases, where orthogonal polynomials can be applied to simplify the process to get higher-order rules, higher-order rules in multi-dimensional cases rely on the numerical solutions of the non-linear equations. High-order rules to degree 20 on triangles can be found in the literature [15].

### 2.4.3 Duffy Transform

When the spatial testing function and the basis function are in the same surface element, the testing integral become singular since  $|\mathbf{r} - \mathbf{r}'|$  goes to 0. Several mathematical methods can be deployed to eliminate such singularities. The Duffy transform is the method used in our work [14].

Consider the integral of a function  $f(x, y)$  over an isosceles right triangle  $A$  with vertices at  $(0, 0)$ ,  $(0, 1)$  and  $(1, 1)$  as following:

$$\iint_A f(x, y) ds = \int_0^1 dx \int_0^x dy f(x, y). \quad (2.152)$$

We assume the function  $f(x, y)$  has the form,

$$f(x, y) = h(x, y) (x^2 + y^2)^{\frac{\alpha}{2}} \quad (2.153)$$

where  $h(x, y)$  is analytic in the region of integration. This makes the integral singular at the origin for  $\alpha < 0$ . To eliminate the singularity, we introduce the transformation

$$y = xu, \quad (2.154)$$

where  $u \in [0, 1]$ . Substituting (2.154) and (2.153) into (2.152), we find

$$\iint_A f(x, y) ds = \int_0^1 dx \int_0^1 du h(x, y) x^{1+\alpha} (1 + u^2)^{\frac{\alpha}{2}}. \quad (2.155)$$

The singularity (if it exists) now only exists on the  $x$  integral, and it has been reduced in order by one. This works for all of the integrals encountered in this work.

#### 2.4.4 Adaptive Integral Method

The adaptive integral method (AIM) is used to accelerate the solution of integral equations. Here, we use AIM to ensure that our gaze is not limited to electrically small problems. AIM accelerates computations by approximating continuous basis functions on a grid of point-like auxiliary basis functions located on uniformly spaced Cartesian grid nodes [9]. This configuration enables the use of the fast Fourier transform (FFT) to accelerate the computation of fields through convolution with a Green's function. We review AIM briefly here for completeness.

To begin, each Cartesian component of each basis function and the associated basis function divergence is expanded into a linear combination of auxiliary basis functions located at nodes of a Cartesian grid enclosing the object. Let basis function  $\ell$  have a component  $B_\ell(\mathbf{r})$ . Assuming the grid has the same spacing  $d$  in each of the three Cartesian directions, the nodes in the grid can be written in the form

$$\mathbf{u}_{mnp} = d(m\hat{\mathbf{x}} + n\hat{\mathbf{y}} + p\hat{\mathbf{z}}), \quad (2.156)$$

and the basis function can be expanded as

$$B_\ell(\mathbf{r}) = \sum_{m=-L}^L \sum_{n=-L}^L \sum_{p=-L}^L \Lambda_{mnp}^\ell \delta(\mathbf{r} - \mathbf{u}_{mnp}), \quad (2.157)$$

where  $\mathbf{u}_{mnp}$  is the closest grid point location to the centroid  $x_\ell\hat{\mathbf{x}} + y_\ell\hat{\mathbf{y}} + z_\ell\hat{\mathbf{z}}$  of the support  $S_\ell$  of  $B_\ell(\mathbf{r})$ , and  $L$  is an integer that determines how many grid points are used for the expansion (usually 1 or 2). The weights of the auxiliary basis functions are chosen to reproduce the moments of  $B_\ell$  by solving

$$\begin{aligned} \iiint_{S_\ell} (x - x_\ell)^{m'} (y - y_\ell)^{n'} (z - z_\ell)^{p'} B_\ell(\mathbf{r}) dx dy dz \\ = \sum_{m=-L}^L \sum_{n=-L}^L \sum_{p=-L}^L \Lambda_{mnp}^\ell (md)^{m'} (nd)^{n'} (pd)^{p'} \end{aligned} \quad (2.158)$$

where  $0 \leq m', n', p' \leq 2L + 1$ . The  $\Lambda_{mnp}^\ell$  are projection operators for each Cartesian basis function component (and for the basis function divergence) that can then be collected into a global projector  $\mathbf{\Lambda}$  that projects all of the basis function current components and the divergence onto the grid. (The exact layout of this matrix is rather flexible and need not concern us here.) This matrix is sparse because basis functions only project onto grid points in their immediate vicinity.

The purpose of all of this projection is that fields on a grid created by sources on a grid can be computed by convolution, and discrete convolutions can be computed efficiently using the FFT. The only difficulty beyond accounting thus encountered is that the auxiliary basis functions are an inaccurate representation of the sources in the near field. Thus we split the elements of the impedance kernel  $\mathbf{Z}_k$  for given time step  $k$  in (2.91) into a far field part and a near field correction:

$$\mathbf{Z}_k = \mathbf{Z}_k^{\text{near}} + \mathbf{Z}_k^{\text{far}}. \quad (2.159)$$

The far field part of any of these matrices,  $\mathbf{Z}_k^{\text{far}}$ , projects the basis functions onto the grid, computes the grid fields using the FFT, and then projects the resulting fields back to the patches to test them. Let some particular component of this operation at any time step separation be denoted by  $\mathbf{Z}^{\text{far}}$ , be it the influence of the  $y$ -directed portion of the current on the magnetic field  $z$ -component four time steps later, or the effect of the charge on the  $x$ -component of the electric field at the next time step. This matrix can be written as

$$\mathbf{Z}^{\text{far}} = \mathbf{\Lambda}^T \mathbf{G} \mathbf{\Lambda}, \quad (2.160)$$

where the rightmost factor  $\mathbf{\Lambda}$  represents projection onto the grid,  $\mathbf{G}$  computes the grid fields from the grid currents, and  $\mathbf{\Lambda}^T$  effects a projection back from the grid to the basis functions. The projection matrices are sparse, and the matrix  $\mathbf{G}$  represents a convolution and is therefore easily and rapidly multiplied by a vector. In the frequency domain, this is all there is to be said about AIM; the acceleration in matrix-vector multiplication is used in concert with an iterative solver to solve the problem fast.

In the time domain, the issue is a bit more complicated because the  $\mathbf{Z}_k$  are sparse in the original time marching formulation; in particular  $\mathbf{Z}_k$  has nonzero elements only where two patches interact with a  $k$ -time step delay. Because every pair of patches interacts with *some* time delay, a straightforward (non-AIM) implementation of MoT is  $O(N_s^2 N_t)$ , and the process implied above, which accounts for the invariance of space but not time, does not accelerate it.

Fortunately, the scattering problem is time-invariant and discretized into equal time steps, so that the temporal dimension can also be accelerated by FFT. This must be done carefully, however, as neglecting causality inflates the MoT process into one in which all  $N_t N_s$  unknowns are sought in a single, expensive, global solution operation. By grouping the  $\mathbf{Z}$  matrices into blocks as shown in Fig. 2.16, the MoT solution can be computed using four-dimensional Fourier transforms and by MoT [66]. In the figure, each block represents a convolution in time, and the elements of the blocks themselves represent three-dimensional spatial convolutions. Thus, each of the blocks highlighted in Fig. 2.16 can be computed using a four-dimensional FFT, and this process can be completed before the fields so computed are necessary for incorporation into the time stepping operation. For example, the first  $2 \times 2$  block multiplies only the currents at the first two time steps, and computes quantities only needed at the third and fourth time step. This procedure preserves time marching and can be shown to have a complexity of  $O(N_t N_s \log^2(N_t N_s))$ , fast enough to allow examination of electromagnetically larger problems.

#### 2.4.5 Adaptive Quadrature

Finally, the primary question examined in this work is how the accuracy of matrix element computation in the discretization of integral equations like Equations (2.53) and (2.54) affects the stability of the algorithm. The primary source of error in such element computations is, of course, the approximation afforded by numerical quadrature. (While geometric errors are also present, they are irrelevant to stability questions—after all, the object modeled by the algorithm *could* be an exact

$$\begin{bmatrix} Z_0 I_1 \\ Z_0 I_2 \\ Z_0 I_3 \\ Z_0 I_4 \\ Z_0 I_5 \\ Z_0 I_6 \\ Z_0 I_7 \\ Z_0 I_8 \\ Z_0 I_9 \\ Z_0 I_{10} \\ Z_0 I_{11} \\ Z_0 I_{12} \\ Z_0 I_{13} \\ Z_0 I_{14} \\ Z_0 I_{15} \\ Z_0 I_{16} \end{bmatrix} = \begin{bmatrix} V_1 \\ V_2 \\ V_3 \\ V_4 \\ V_5 \\ V_6 \\ V_7 \\ V_8 \\ V_9 \\ V_{10} \\ V_{11} \\ V_{12} \\ V_{13} \\ V_{14} \\ V_{15} \\ V_{16} \end{bmatrix} - \begin{bmatrix} 0 \\ \boxed{Z_1} & 0 \\ \boxed{Z_2} & \boxed{Z_1} & 0 \\ \boxed{Z_3} & \boxed{Z_2} & \boxed{Z_1} & 0 \\ Z_4 & Z_3 & Z_2 & Z_1 & 0 \\ Z_5 & Z_4 & Z_3 & Z_2 & \boxed{Z_1} & 0 \\ Z_6 & Z_5 & Z_4 & Z_3 & \boxed{Z_2} & \boxed{Z_1} & 0 \\ Z_7 & Z_6 & Z_5 & Z_4 & \boxed{Z_3} & \boxed{Z_2} & \boxed{Z_1} & 0 \\ Z_8 & Z_7 & Z_6 & Z_5 & Z_4 & Z_3 & Z_2 & Z_1 & 0 \\ Z_9 & Z_8 & Z_7 & Z_6 & Z_5 & Z_4 & Z_3 & Z_2 & \boxed{Z_1} & 0 \\ Z_{10} & Z_9 & Z_8 & Z_7 & Z_6 & Z_5 & Z_4 & Z_3 & \boxed{Z_2} & \boxed{Z_1} & 0 \\ Z_{11} & Z_{10} & Z_9 & Z_8 & Z_7 & Z_6 & Z_5 & Z_4 & \boxed{Z_3} & \boxed{Z_2} & \boxed{Z_1} & 0 \\ Z_{12} & Z_{11} & Z_{10} & Z_9 & Z_8 & Z_7 & Z_6 & Z_5 & \boxed{Z_4} & \boxed{Z_3} & \boxed{Z_2} & \boxed{Z_1} & 0 \\ Z_{13} & Z_{12} & Z_{11} & Z_{10} & Z_9 & Z_8 & Z_7 & Z_6 & \boxed{Z_5} & \boxed{Z_4} & \boxed{Z_3} & \boxed{Z_2} & \boxed{Z_1} & 0 \\ Z_{14} & Z_{13} & Z_{12} & Z_{11} & Z_{10} & Z_9 & Z_8 & Z_7 & \boxed{Z_6} & \boxed{Z_5} & \boxed{Z_4} & \boxed{Z_3} & \boxed{Z_2} & \boxed{Z_1} & 0 \\ Z_{15} & Z_{14} & Z_{13} & Z_{12} & Z_{11} & Z_{10} & Z_9 & Z_8 & \boxed{Z_7} & \boxed{Z_6} & \boxed{Z_5} & \boxed{Z_4} & \boxed{Z_3} & \boxed{Z_2} & \boxed{Z_1} & 0 \end{bmatrix} \cdot \begin{bmatrix} I_1 \\ I_2 \\ I_3 \\ I_4 \\ I_5 \\ I_6 \\ I_7 \\ I_8 \\ I_9 \\ I_{10} \\ I_{11} \\ I_{12} \\ I_{13} \\ I_{14} \\ I_{15} \\ I_{16} \end{bmatrix}$$

**Figure 2.16:** Structure of the time domain AIM operator.

description of a scatterer.) Initial attempts to control quadrature error by using rules of different orders led to confusing results because order is a poor proxy for accuracy. After all, low order integrations can, by sheer luck, return accurate integral results, and high order is not synonymous with high accuracy. We therefore use adaptive quadrature to allow more precise accuracy control of integration.

Adaptive quadrature works by prescribing a relative error goal, and approximating the desired integral as a sum over smaller and smaller intervals until the desired error is achieved [40]. More specifically, a numerical approximation  $Q[a, b]$  to the integral of  $f(x)$  over the interval  $[a, b]$  is computed first, followed by the approximation over two subintervals. An error estimate  $\epsilon$  thus presents itself [40]:

$$\epsilon = \frac{|(Q[a, \frac{a+b}{2}] + Q[\frac{a+b}{2}, b]) - Q[a, b]|}{|(Q[a, \frac{a+b}{2}] + Q[\frac{a+b}{2}, b])|}. \quad (2.161)$$

If the estimated error is larger than the input tolerance  $\tau$ , the intervals are subdivided again, and the process is repeated on each half. The subdivision continues until the error is less than  $\tau$  on every interval.

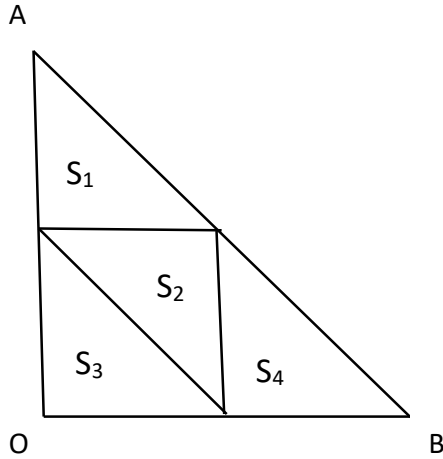


**Figure 2.17:** A triangle division scheme.

This process is not greatly affected by the dimension (or shape) of the integration domain; the same procedure can be used, though the number of subdivisions may change. For a 2-D case, Fig. 2.17 shows a triangle  $S$  defined by vertices  $A$ ,  $B$  and  $O$ , divided into four small triangles  $S_1$ ,  $S_2$ ,  $S_3$  and  $S_4$ , by the mid-point of each edge. To apply adaptive quadrature, a numerical approximation  $Q[S]$  to the surface integral of  $f(x, y)$  over the triangle  $S$  is computed first, followed by the approximation over the four sub triangles. An error estimate  $\epsilon$  can be computed as [40]:

$$\epsilon = \frac{\left| \sum_{i=1}^4 Q[S_i] - Q[S] \right|}{\left| \sum_{i=1}^4 Q[S_i] \right|}. \quad (2.162)$$

If it is larger than the input tolerance  $\tau$ , the triangles are subdivided again, and the process is repeated on each of them. The subdivision continues until the error is less than  $\tau$  on every triangle.

## Chapter 3

### TDIE STABILITY COMPUTATIONS FOR PEC SCATTERERS

In this chapter, numerical results are presented to elucidate the relation between integration accuracy and the stability of PEC scattering TDIE simulations. All scatterers simulated are perfect conductors, and the CFIE ( $\alpha = 0.5$ ) is used for all simulations, except open scatterers where the EFIE ( $\alpha = 1$ ) is required.

In all examples, the scatterer is illuminated by a incident wave given by

$$\mathbf{E}^{\text{inc}}(z, t) = \hat{\mathbf{x}} \exp\left[\frac{1}{2\sigma^2} \left(t - \frac{z}{c} - \tau\right)^2\right] \cos\left[2\pi f_0 \left(t - \frac{z}{c}\right)\right] \quad (3.1)$$

where  $f_0$  is a center frequency, and  $\tau$  is a delay. The temporal standard deviation  $\sigma$  is related to a nominal bandwidth  $f_{\text{bw}}$  by  $\sigma = 6/(2\pi f_{\text{bw}})$ .

For all the scatterers presented here, the bistatic radar cross-section (RCS) is computed for different frequencies and angles and compared to a frequency domain MoM code to compute errors. Bistatic RCS results were computed from 181 elevation angles between  $\theta = 0^\circ$  and  $\theta = 180^\circ$ . The azimuthal angle was set to  $\phi = 0^\circ$ . Occasionally, monostatic RCS results are used to relate frequency error.

The self integration rules described in Subsection 2.4.3 and [62] are used when a basis patch and a test patch overlap. The underlying basis and testing integration rules are the Dunavant rules described in [15]. Testing integration is always accomplished with a non-adaptive fifth-order Dunavant rule. Non-self basis integrations are done with one of two adaptive rules with error depending on their proximity. (The basic integration rules underlying the adaptive scheme are first-order Dunavant rules.) We define a distance  $d_{\text{near}}$  such that basis integrations are called *near* when their centroids are separated by less than this distance and *far* otherwise. In the examples presented

here that do not use AIM, we set this distance to  $0.4 \times \lambda_{\min}$ , where  $\lambda_{\min}$  corresponds to the shortest frequency of interest in the simulation. We call a simulation *stable* if all currents were less than  $0.001 \text{ fA/m}^2$  at the end of the simulation. Different choices of these parameters may lead to different numerical results. Yet it is of secondary importance here since the purpose of this research is the exposition of the relationship between the integral accuracy and the stability of TDIE solvers rather than obtaining the stability pattern of some specific geometry. Numerical results were obtained for different values of the error allowed by the adaptive integrator. Stability of different runs is indicated in a table, where shadow squares mark unstable computations and white squares mark stable ones.

### 3.1 Ogive

We first consider the conducting ogive shown in Fig. 3.1. The ogive axis is about 2m long, and its largest diameter is 0.4cm. It is meshed with 304 flat patches. We set  $\Delta t = 100\text{ps}$  and the number of time steps to  $N_t = 4000$ . For the incident wave, the nominal frequency band  $f_{\text{bw}}$  was chosen to be 300MHz, the central frequency  $f_0$  was 100MHz, and the delay  $\tau$  was 20ns. RCS results at 21 equally-spaced frequencies from 200MHz to 240MHz were computed. The orders of integration rules upon which the adaptive integrals are based for both near field and far field basis integrals are 1. All the testing integrations are calculated with a fifth-order Dunavant rule. All the basis integration rules are first-order rule. The spatial basis functions are the first-order GWP bases. For the BLIF method, the number of the past steps used for extrapolation was  $N_{\text{samp}} = 6$ , the APSWF width was  $N = 7$ , and the APSWF bandwidth was  $\omega_0 = 2\pi \times 160\text{MHz}$ .

Fig. 3.2 compares the current delivered at a particular point on the scatterer between CQ-BDF2 and BLIF for a stable simulation. The current is observed in the center a patch somewhere on the ogive. The relative error tolerance in the adaptive quadrature for both near field and far field integral are set to 0.3. Fig. 3.3 shows the late time current at the same observation point for an unstable simulation, with relative

error tolerance in the adaptive quadrature for both near field and far field integral being set to 2.0. These figures give an impression of the behavior of simulations that work versus those that go awry. To illustrate a more global picture and discuss accuracy more precisely, later we will compare the RCS results obtained after the end of the simulations to frequency domain result.

Fig. 3.4 shows the RCS results obtained for this problem by time domain and frequency domain codes. We generated the data for these figures with the relative error tolerance in the adaptive quadrature to 0.2 for both near field and far field integral to ensure accurate results. An excellent correspondence can be observed among these three curves.

Figs. 3.5 and 3.6 show the stability pattern for the CQ and BLIF methods, respectively. It can be observed in Fig. 3.5 that once the near field basis integral is “good enough” (less than 50% relative error), the accuracy requirement for the far field be almost ignored with proper near-far division. Fig. (3.6) shows the stability pattern for BLIF method.

### 3.2 NASA Almond

The NASA almond shown in Fig. 3.7 is about 25cm in its longest dimension and 3.3cm in its smallest. It is meshed with 264 flat patches. The time step length is taken as  $\Delta t = 10\text{ps}$ , and the number of time steps is set to  $N_t = 2500$ . The nominal bandwidth of the incident wave  $f_{\text{bw}} = 1\text{GHz}$ , centered about  $f_0 = 1.5\text{GHz}$ , and the delay  $\tau = 7.6\text{ns}$ . We computed the RCS at 21 equally spaced frequencies located from 1 to 2GHz. The near field integration threshold was taken to be 6cm. The spatial basis functions were chosen to be first-order GWP. The BLIF method set the number of the past steps to 6, the APSWF width to 7, and the APSWF frequency to 2.5GHz. The testing rule was set to fifth-order. The orders of the underlying integration rules for the adaptive integration method for both near field and far field basis integrals are 1.

Fig. 3.8 shows the RCS results obtained for this problem by three different simulations methods representing both the time domain and the frequency domain.

In the time domain codes, the relative error tolerance in the adaptive quadrature is 20% for both near field and far field integrals. The difference between the time domain results and frequency domain results in Fig. 3.7(d) is less than 0.2 dB, which verifies our time domain results.

Figs. 3.9 and 3.10 show the stability patterns realized for CQ and BLIF methods, respectively. Again, Fig. 3.9 demonstrates that for CQ once the near field accuracy is high enough (around 70%), the accuracy requirements for the far field integration can be far less strict.

### 3.3 Tank

Next we simulate electromagnetic scattering from a tank model. The model, shown in Fig. 3.11, is 8.02m long including the gun barrel, 2.57m wide, and 1.80m high. It is meshed with 2078 patches supporting a total of 10268 first-order GWP bases. To accelerate the computation, AIM is used for this example. Moreover, on this problem, we examine the stability of CQ for larger time steps and simpler integration rules. Because of the need for extrapolation, the BLIF method is limited to small time steps and accurate results, but CQ can return more approximate results faster. We demonstrate this ability here; though not shown, the CQ method can stably return results for the parameters used for the BLIF simulation.

In any case, the incident wave for both examples is the same, with nominal frequency band  $f_{\text{bw}} = 40\text{MHz}$ , central frequency  $f_0 = 120\text{MHz}$ , and incident time delay  $0.2\mu\text{s}$ . The time step length  $\Delta t$  for both methods was chosen as 400 ps and the number of total time steps was  $N_t=1100$ . The near field integration threshold was  $d = 0.4\text{m}$ . First-order integration rules were used in the adaptive process for the basis function integrations, and testing integration rule is set to fifth-order. The AIM grid size was 0.2m.

Fig. 3.12 shows the comparison of the RCS results obtained by the different methods. RCS results were obtained at 21 frequencies located from 100MHz to 140MHz with equal intervals. In the time domain codes, we set the relative error tolerance in the

adaptive quadrature to 0.2 for both near field and far field integrals to generate these particular figures. The results from the BLIF method show excellent correspondence with less than 0.02 dB error seen in in Fig. 3.12(d). The RCS results from CQ have a slightly greater discrepancy with the frequency domain results, but this is to be expected from this less accurate method.

Fig. 3.13 shows the stability pattern for CQ. Fig. 3.10 shows the stability pattern for BLIF method. This figures also illustrate the relative unimportance of far field integration on accuracy and stability. Because AIM relies crucially on an approximation that is difficult to control, there is no guarantee that better accuracy in the computation of basis function integrations in general will preserve the behavior of the method. The fact that the stability is not apparently adversely affected by the fast method lends further credence to the primacy of near field computations in stability and accuracy determination.

### 3.4 Sphere

Since all of the objects presented to this point were all meshed with flat patches, the next object studied here is a sphere of 1.0m radius. It was meshed into 128 spherical triangular patches. The incident wave is of 40MHz nominal frequency band, 120MHz center frequency, and time delay to the origin of  $0.2\mu s$ . The spatial bases were first-order GWP basis functions. We set the near field integration threshold to 0.86m. The testing rule was set to fifth-order, and the adaptive rules were built on one-point integrations. The temporal discretization is consist of total 5000 time steps of 100ps each. The BLIF method parameters were  $N_{\text{past}} = 5$ ,  $N = 6$ , and  $f_0 = 200\text{MHz}$ .

Fig. 3.15 shows the RCS results at 21 frequencies located from 100 MHz to 140 MHz with 2 MHz increment. The relative error tolerance in the adaptive quadrature was 0.2 for both near field and far field integral. The figure compares our time domain simulation results to the Mie series result rather than an MoM result since for this scatterer analytical results can be computed.

Fig. 3.16 shows the stability pattern for the CQ method. Fig. 3.17 shows the

stability results for the BLIF method. Both time domain methods have a similar pattern. This result thus indicates that a more strict near field integral accuracy is required to accomplish stability. The clarity of this result may be due to the curvilinear patches, which necessitate numerical (rather than analytical) treatment at every step in the formulation.

### 3.5 Flat Square

The next object studied here is a flat square plate of 1.5m sides. It was meshed into 200 flat right-triangular patches. The incident wave is of 100MHz nominal frequency band, 150MHz center frequency and time delay to the origin of  $0.076\mu\text{s}$ . The spatial bases were first-order GWP basis functions, and the near field integration threshold was 0.6 m. The testing rule was fifth-order, and the adaptive rules were built on one-point integrations. The temporal dimension was discretized into total 1500 time steps of 100 ps each. The remaining BLIF method parameters were  $N_{\text{past}} = 5$ ,  $N = 6$ , and  $f_0 = 250\text{MHz}$ .

Fig. 3.18 shows the RCS results at 21 frequencies located from 100 MHz to 200 MHz with 5 MHz increment. The relative error tolerance in the adaptive quadrature was 0.2 for both near field and far field integral.

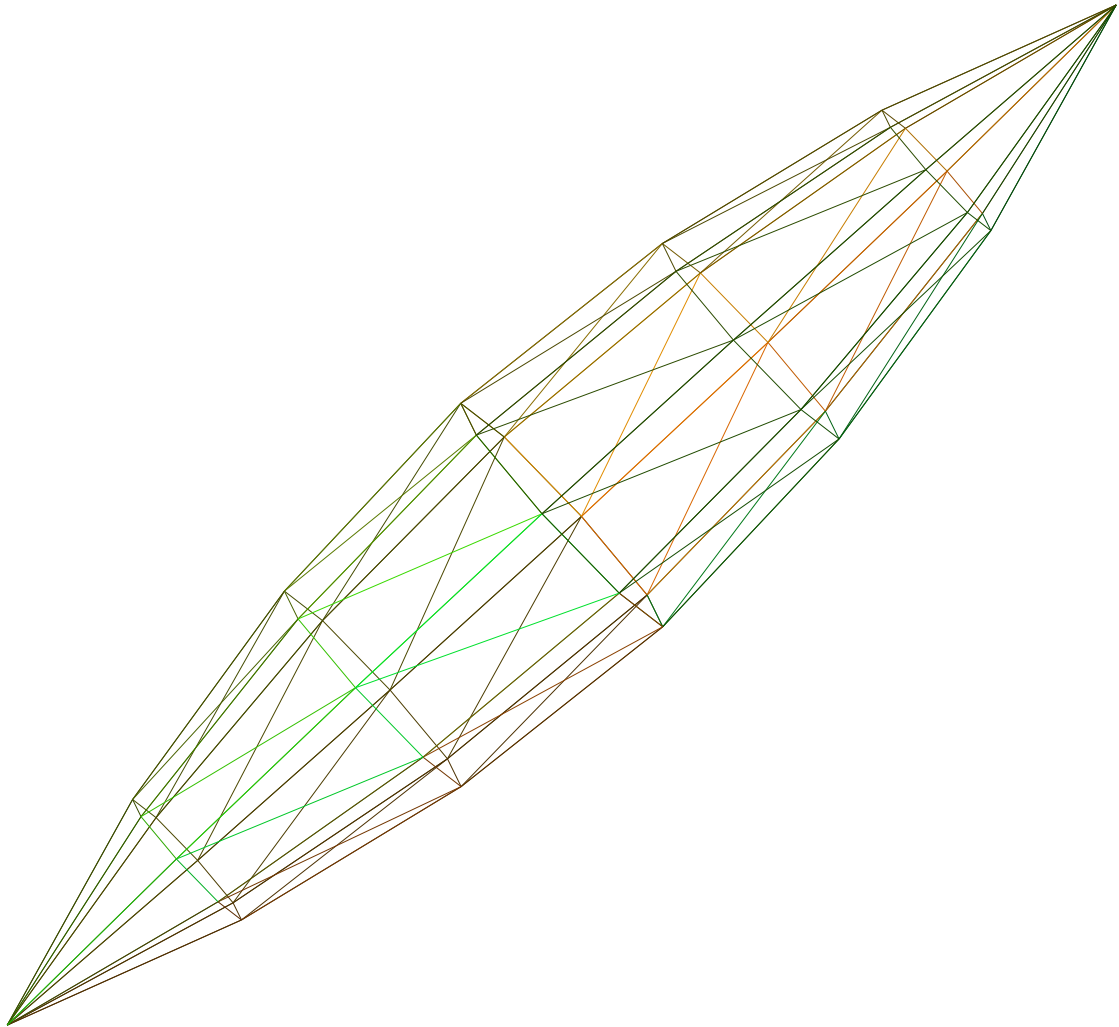


**Figure 3.1:** A perfectly conducting ogive.

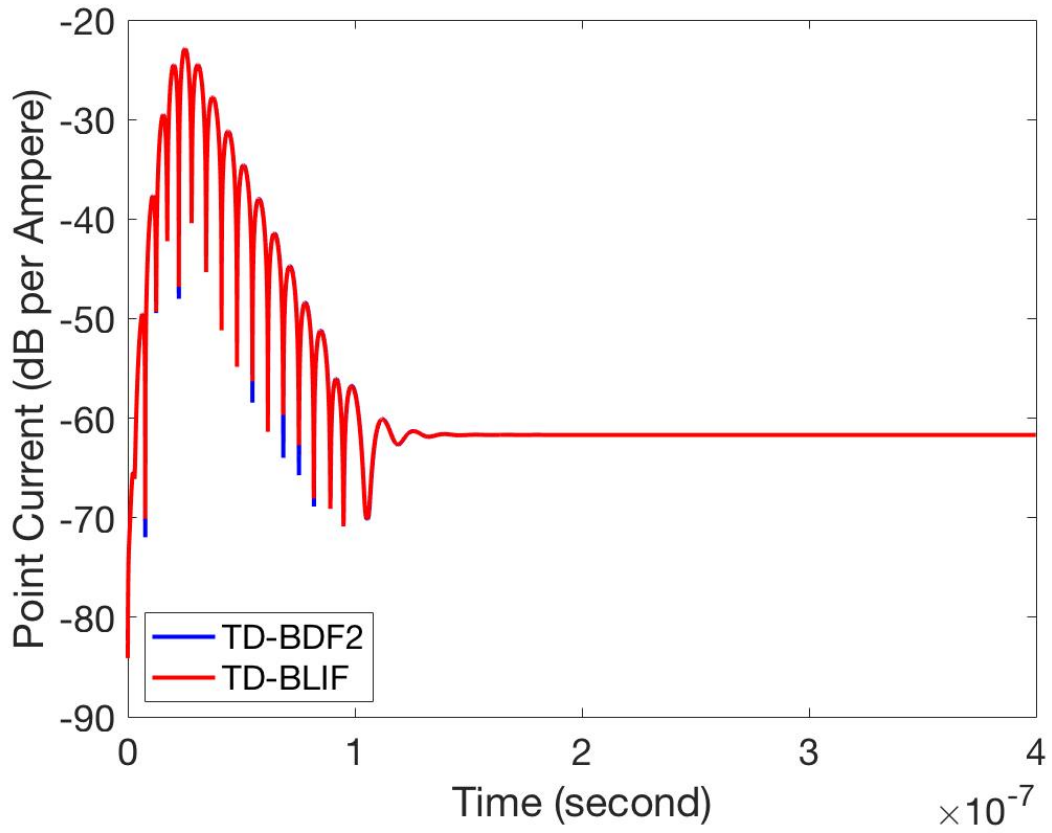


**Figure 3.2:** Late time current behavior of a stable simulation.

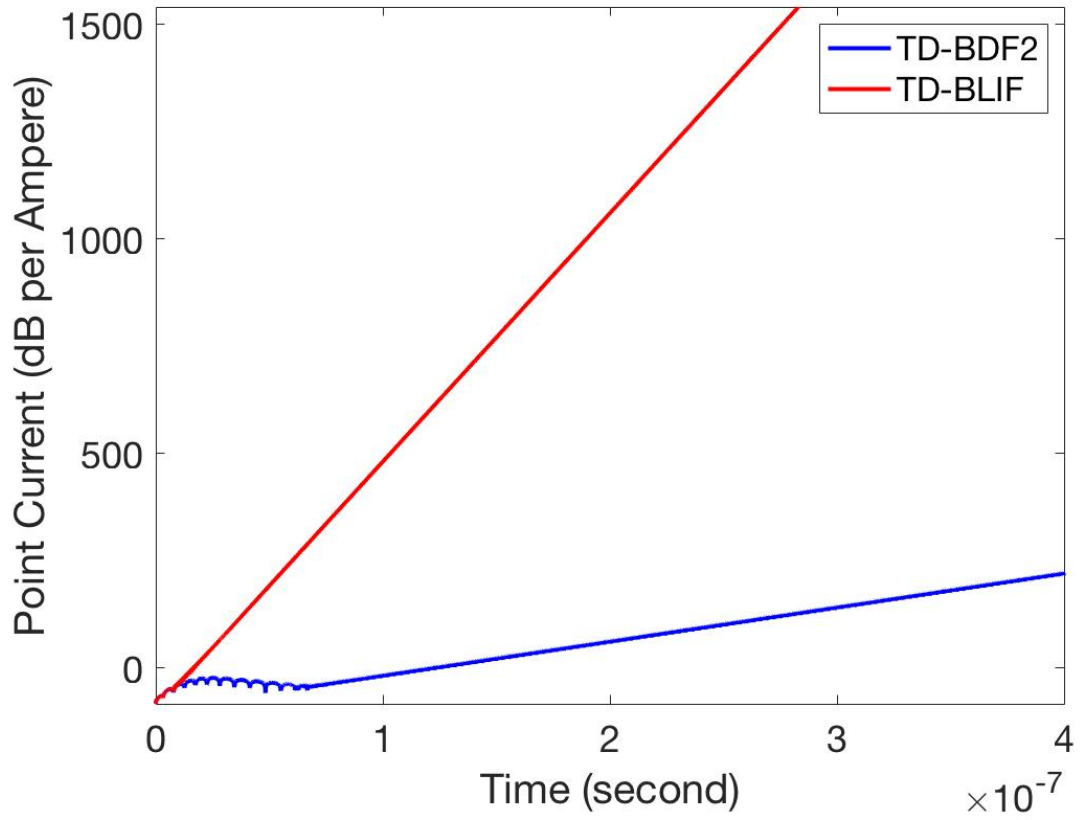


**Figure 3.3:** Late time current behavior of an unstable simulation.

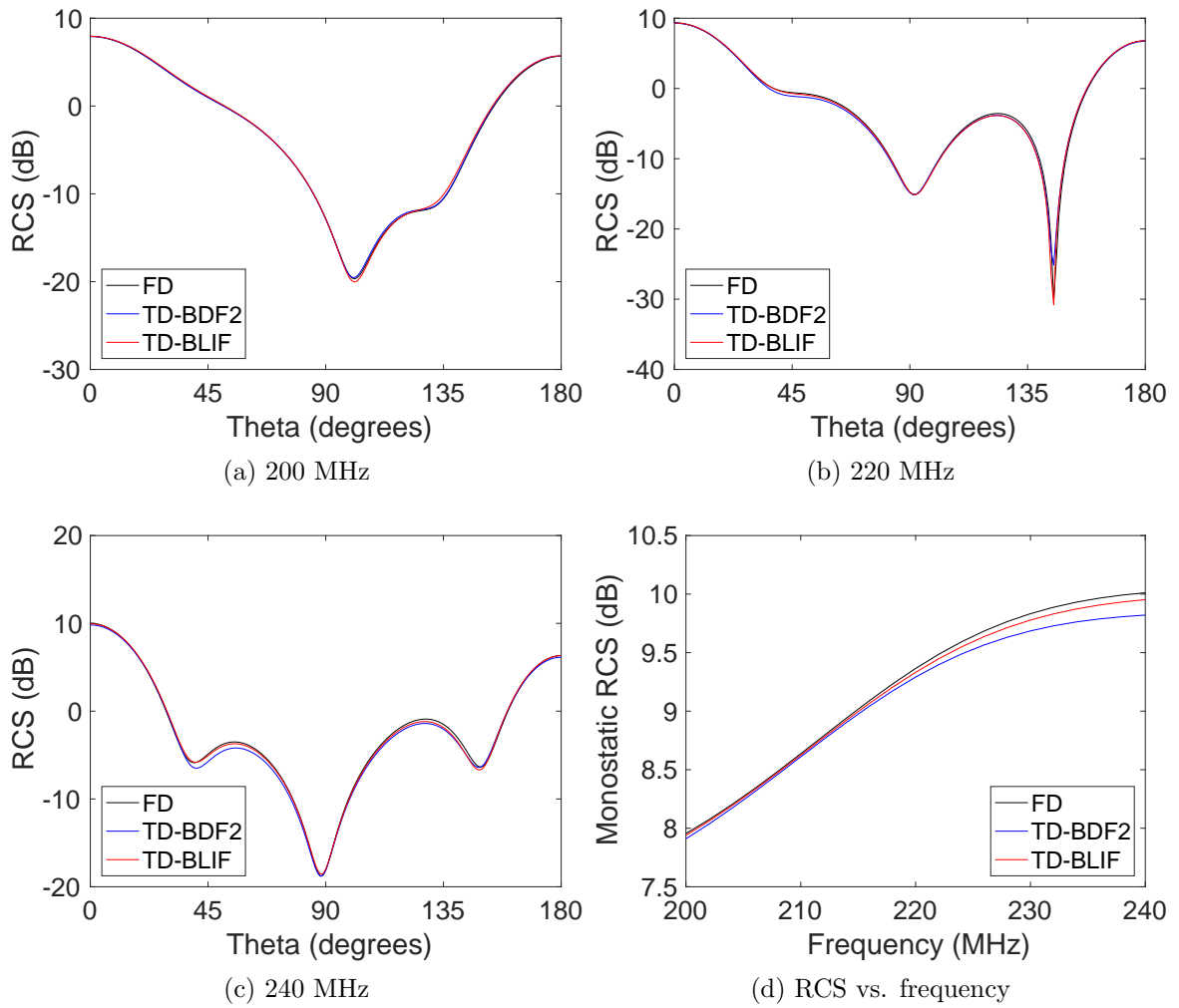


**Figure 3.4:** Bistatic RCS of the ogive computed at (a) 200MHz, (b) 220MHz, and (c) 240MHz, and (d) the monostatic RCS between 200 and 240 MHz.

		Far Field									
		10%	20%	30%	40%	50%	60%	70%	80%	150%	200%
Near Field	10%										
	20%										
	30%										
	40%										
	50%										
	60%										
	70%										
	100%										
	150%										
	200%										

**Figure 3.5:** Stability of the simulation versus integration accuracy for a perfect conducting ogive for CQ.

		Far Field									
		10%	20%	30%	40%	50%	60%	70%	80%	150%	200%
Near Field	10%										
	20%										
	30%										
	40%										
	50%										
	60%										
	70%										
	100%										
	150%										
	200%										

**Figure 3.6:** Stability of the simulation versus integration accuracy for a perfect conduction ogive for BLIF.

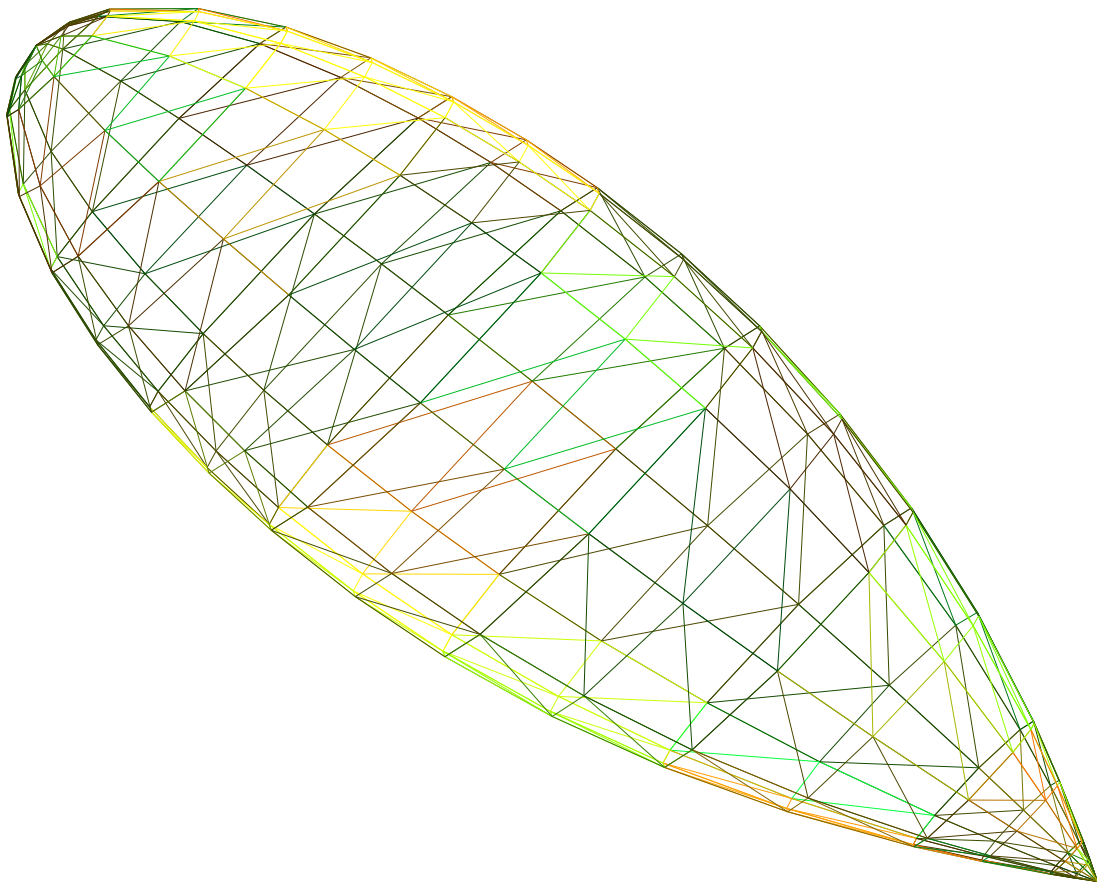


**Figure 3.7:** A NASA almond.

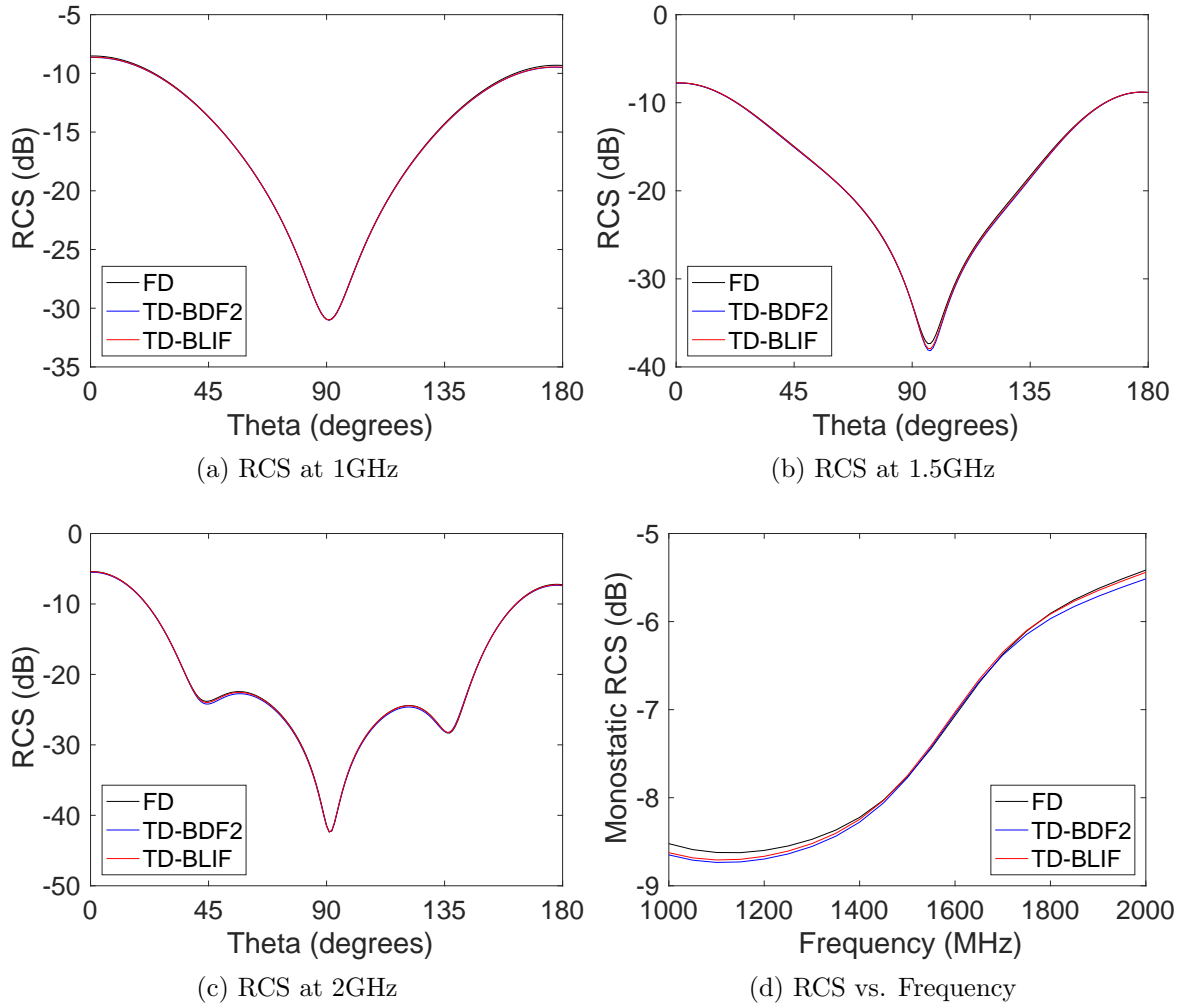


**Figure 3.8:** Comparison of RCS results. Subfigures (a), (b) and (c) show the bistatic RCS results at the lowest frequency, center frequency, and highest frequency in the range. Subfigure (d) shows the monostatic RCS obtained at elevation angle  $\theta = 0$ .

		Far Field									
		10%	20%	30%	40%	50%	60%	70%	80%	150%	200%
Near Field	10%										
	20%										
	30%										
	40%										
	50%										
	60%										
	70%										
	100%										
	150%										
	200%										

**Figure 3.9:** Stability of the simulation versus integration accuracy for a perfect conducting NASA almond for CQ.

		Far Field									
		10%	20%	30%	40%	50%	60%	70%	80%	150%	200%
Near Field	10%										
	20%										
	30%										
	40%										
	50%										
	60%										
	70%										
	100%										
	150%										
	200%										

**Figure 3.10:** Stability of the simulation versus integration accuracy for a perfect conducting NASA almond for BLIF.

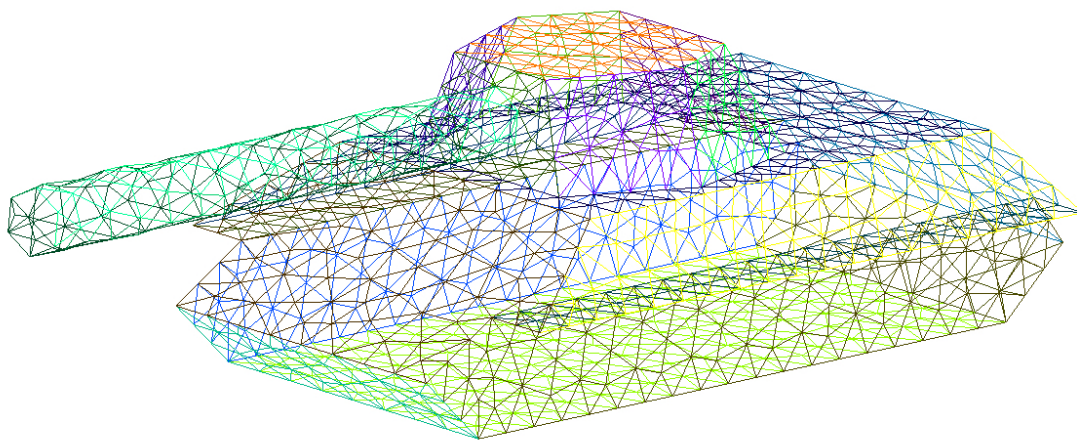


**Figure 3.11:** A perfectly conducting scatterer approximating a tank.

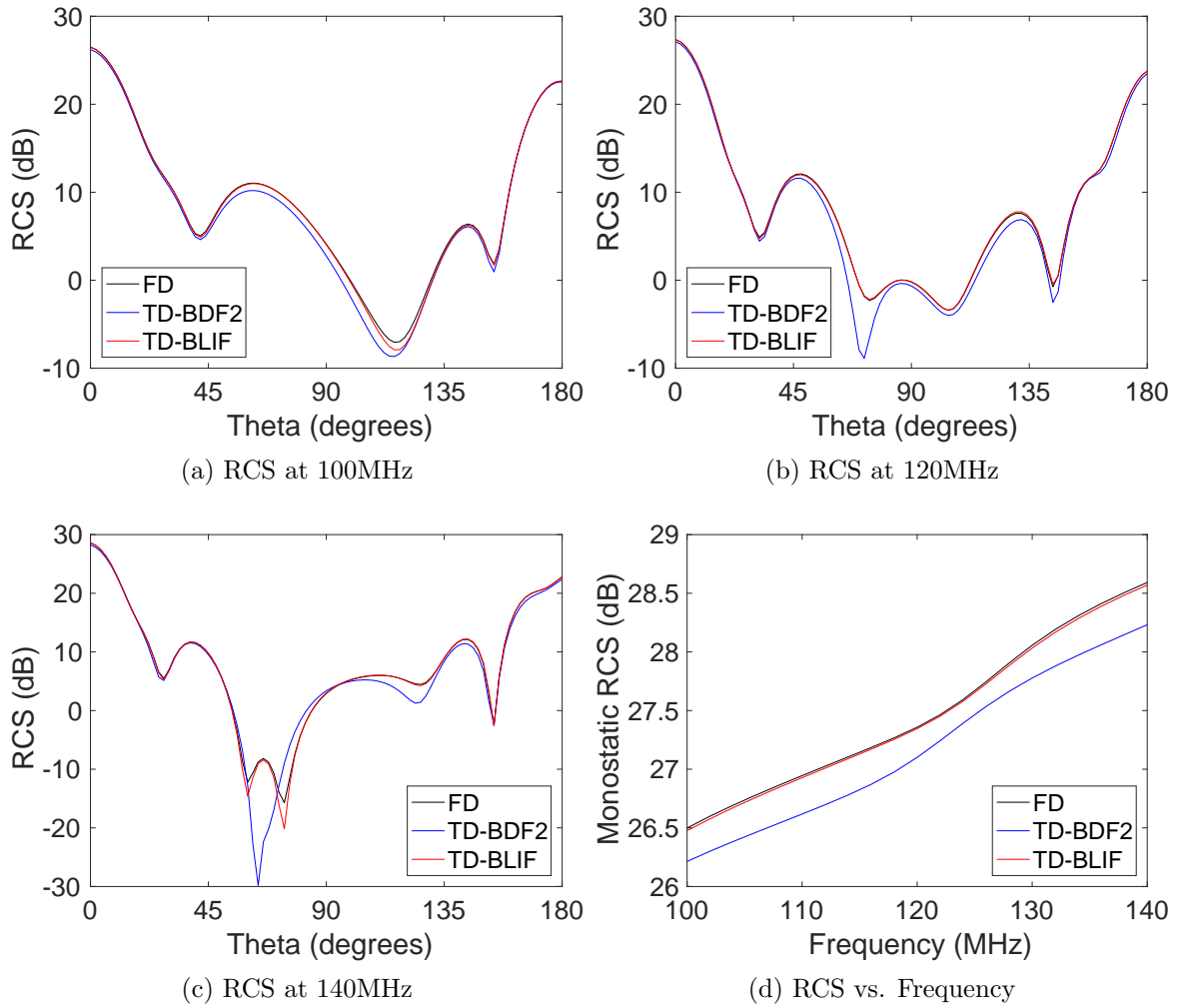


**Figure 3.12:** Bistatic RCS of the tank computed at (a) 100MHz, (b) 120MHz, and (c) 140MHz, and (d) the monostatic RCS between 200 and 240 MHz.

		Far Field									
		10%	20%	30%	40%	50%	60%	70%	80%	150%	200%
Near Field	10%										
	20%										
	30%										
	40%										
	50%										
	60%										
	70%										
	80%										
	150%										
	200%										

**Figure 3.13:** Stability of the simulation versus integration accuracy for a perfect conducting tank for CQ.

		Far Field									
		10%	20%	30%	40%	50%	60%	70%	80%	150%	200%
Near Field	10%										
	20%										
	30%										
	40%										
	50%										
	60%										
	70%										
	100%										
	150%										
	200%										

**Figure 3.14:** Stability of the simulation versus integration accuracy for a perfect conducting tank for BLIF.

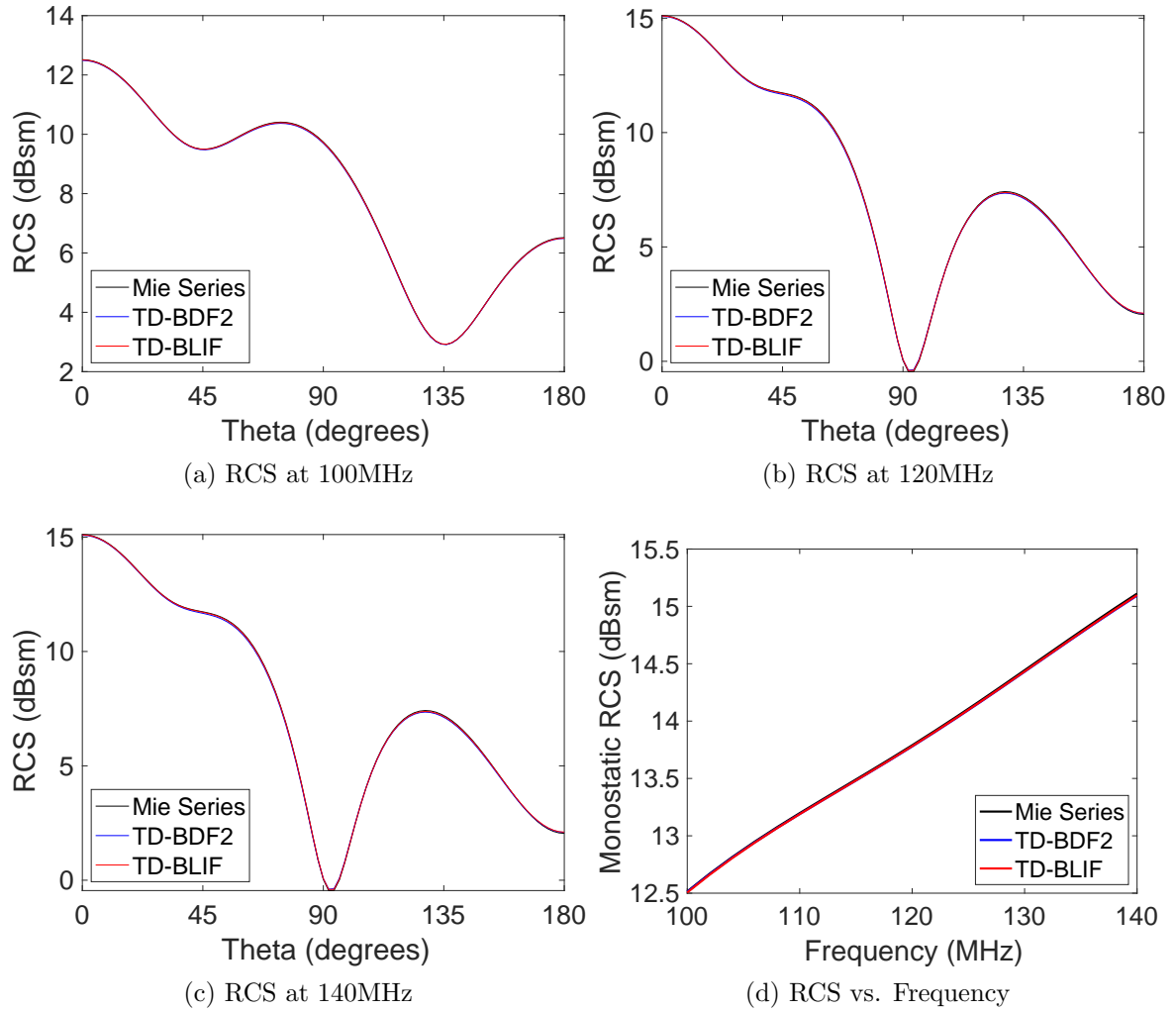


**Figure 3.15:** Comparison of RCS results of a sphere. The bistatic RCS results at start point, middle point and the end point of the frequency range are shown in (a), (b) and (c). The monostatic RCS vs. frequency at elevation angle  $\theta = 0$  is shown in (d).

		Far Field									
		10%	20%	30%	40%	50%	60%	70%	80%	150%	200%
Near Field	10%										
	20%										
	30%										
	40%										
	50%										
	60%										
	70%										
	100%										
	150%										
	200%										

**Figure 3.16:** Stability of the simulation versus integration accuracy for a perfect conducting sphere for CQ.

		Far Field									
		10%	20%	30%	40%	50%	60%	70%	80%	150%	200%
Near Field	10%										
	20%										
	30%										
	40%										
	50%										
	60%										
	70%										
	100%										
	150%										
	200%										

**Figure 3.17:** Stability of the simulation versus integration accuracy for a perfect conducting sphere for BLIF.

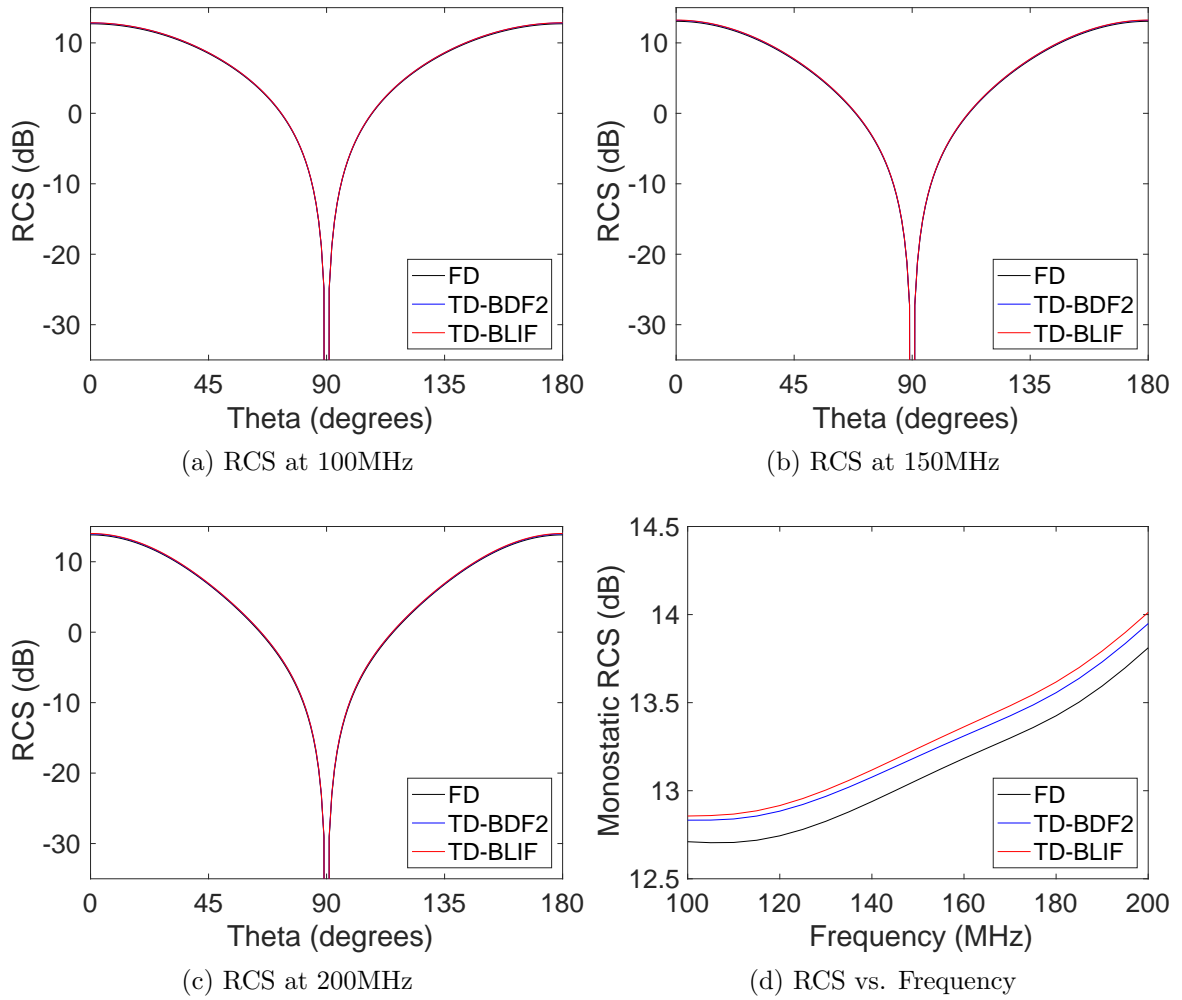


**Figure 3.18:** Comparison of RCS results. The bistatic RCS results at start point, middle point and the end point of the frequency range are shown in (a), (b) and (c). The monostatic RCS vs. frequency at elevation angle  $\theta = 0$  is shown in (d).

		Far Field									
		10%	20%	30%	40%	50%	60%	70%	80%	150%	200%
Near Field	10%										
	20%										
	30%										
	40%										
	50%										
	60%										
	70%										
	80%										
	150%										
	200%										

**Figure 3.19:** Stability of the simulation versus integration accuracy for a perfect conducting square for CQ.

Fig. 3.20 shows the stability pattern for the BLIF method.

		Far Field									
		10%	20%	30%	40%	50%	60%	70%	80%	150%	200%
Near Field	10%										
	20%										
	30%										
	40%										
	50%										
	60%										
	70%										
	100%										
	150%										
	200%										

**Figure 3.20:** Stability of the simulation versus integration accuracy for a perfect conducting square for BLIF.

Fig. 3.19 shows the stability pattern for CQ. Due to the open nature of the structure and its attendant EFIE, stability is more difficult to achieve for this problem. Both time domain methods require a more strict near field integral accuracy to accomplish the feat, but neither fails in a manner rendering TDIE solution impossible or even particularly difficult.

## Chapter 4

### TDIE STABILITY COMPUTATIONS FOR DIELECTRIC SCATTERERS

In this section, numerical results are presented to demonstrate the impact of integral accuracy on the stability of the TDIE implementations for dielectric scatterers. Ultimately, the results will demonstrate qualitative similarity but quantitative difference from those in the last chapter.

All the scatters are illuminated by a Gaussian pulse of the same form given by (3.1). For all the scatters, two kinds of radar cross-section (RCS) are computed for different frequencies and angles as the results presented here. Bistatic RCS results for different frequencies were computed from 181 elevation angles between  $\theta = 0^\circ$  and  $\theta = 180^\circ$ . The azimuthal angle was set to  $\phi = 0^\circ$ . Monostatic RCS results were computed for different frequencies.

For the integral where a basis patch and a test patch overlap, the self integration rules described in Subsection 2.4.3 are used. The underlying basis and testing integration rules are the Dunavant rules described in [15]. We define a distance  $d_{\text{near}}$  such that basis integrations are called *near* when their centroids are separated by less than this distance and *far* otherwise. In all examples presented here, this distance was set to  $0.4\lambda_{\text{min}}$ , where  $\lambda_{\text{min}}$  corresponds to the shortest wavelength of interest in the simulation. Non-self basis integrations are done with one of those two adaptive rules with error depending on their proximity. Underlying the adaptive scheme, the basic integration rules are very low order Dunavant rules. A simulation is called stable if all currents were less than  $0.001 \text{ fA/m}^2$  at the end of the simulation. Numerical results were obtained for different values of the error allowed by the adaptive integrator. Stability of different runs is indicated in a table as last chapter.

## 4.1 Ogive

The first example examined is a dielectric ogive with relative permittivity  $\epsilon_r = 4.0$  and relative permeability  $\mu_r = 1.0$ , as shown in Fig. 3.1. The ogive axis is about 2m long and its largest diameter is 0.4cm. It is meshed with 304 flat patches. For the incident wave, the nominal frequency band  $f_{\text{bw}}$  was chosen to be 300MHz, the center frequency  $f_0$  was 100MHz, and the delay  $\tau$  was  $20\mu\text{s}$ . RCS results at 21 equally-spaced frequencies from 200MHz to 240MHz were computed. The spatial basis functions are the zeroth-order GWP bases commonly known as Rao-Wilton-Glisson, or RWG, bases [44]. We set the total number of time steps  $N_t$  to 4000 and the length of each time step  $\Delta t$  to 100ps for CQ and 30ps for BLIF. (Recall that BLIF always needs a small time step because of the extrapolation.) For the BLIF method, the number of the past steps used for extrapolation was  $N_{\text{samp}} = 6$ , the APSWF width was  $N = 7$ , and the APSWF bandwidth was  $\omega_0 = 2\pi \times 200\text{MHz}$ . The testing rule was set to fifth-order, and the adaptive rules were set to first-order.

Figs. 4.1 shows the stability pattern for the CQ method. These figures show that once the relative error of near field basis integral is lower than 80%, the accuracy requirement for the far field can be almost ignored with proper near-far division. Fig. 4.2 shows the stability pattern for BLIF method. BLIF has a better stability

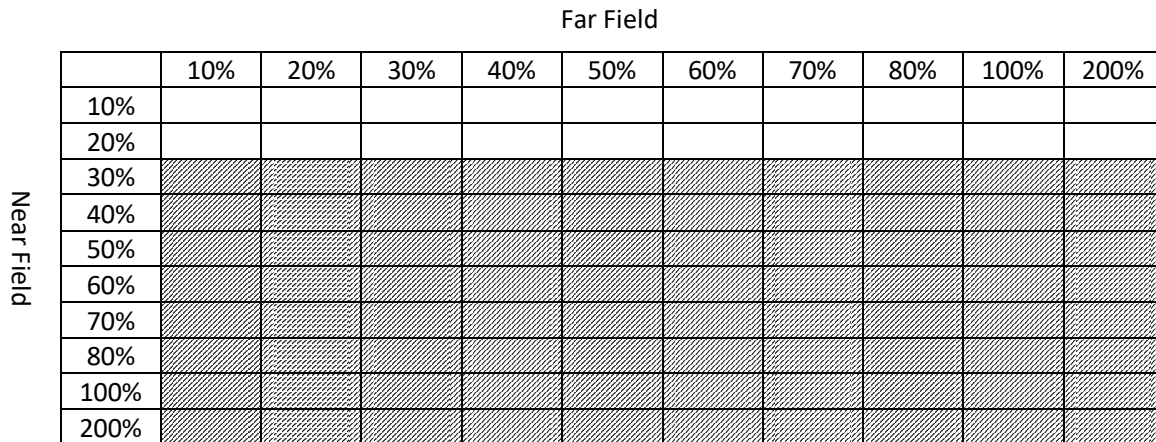


**Figure 4.1:** Stability of the simulation versus integration accuracy for a dielectric ogive for CQ.

pattern for this dielectric ogive compared with the conducting ogive of the last chapter that may be due to the much smaller time step length. It also indicates that the far field integral accuracy is less important than the near field accuracy, as expected.

		Far Field									
		10%	20%	30%	40%	50%	60%	70%	80%	100%	200%
Near Field	10%										
	20%										
	30%										
	40%										
	50%										
	60%										
	70%										
	80%										
	100%										
	200%										

**Figure 4.2:** Stability of the simulation versus integration accuracy for a dielectric ogive for BLIF.

Fig 4.3 shows the comparison of the RCS results obtained for this problem by the two time domain methods and the frequency domain method. The time domain RCS data for these figures was obtained with the relative error tolerance in the adaptive quadrature to 0.2 for both near field and far field integral to ensure accurate results. An excellent correspondence can be observed among these three curves.

## 4.2 Dielectric Sphere

Due to the fact that the ogive is meshed with flat patches, the next example is a sphere meshed by perfect spherical patches. The sphere is of 1.0m radius. The sphere is a dielectric with  $\epsilon = 2.0$  and  $\mu = 1.0$  It was meshed into 128 perfect spherical triangular patches. The incident wave is of 40MHz nominal frequency band, 120MHz center frequency, and time delay to the origin of  $0.2\mu s$ . The choice of the spatial basis was also different from the previous cases. We used first-order basis functions instead of zeroth-order basis functions to increase the difficulty of maintaining stability. The near field integration threshold was set to 0.86m. Testing integration is accomplished with a

non-adaptive fifth-order rule. The adaptive rules were built on one-point integrations. The temporal discretization is consist of total 800 time steps of 250ps each for both CQ and BLIF. The BLIF method parameters were  $N_{\text{past}} = 5$ ,  $N = 6$ , and  $f_0 = 200\text{MHz}$ .

Fig. 4.4 shows the RCS results at 21 frequencies located from 100 MHz to 140 MHz with 2MHz increment. The relative error tolerance in the adaptive quadrature was 0.2 for both near field and far field integral. The figure compares our time domain simulation results to the Mie series result, since analytical results can be computed for spheres. Due to the long time step size, the discrepancy tends to be larger when the frequency goes higher for both methods.

Fig. 4.5 shows the stability pattern for the CQ method. Fig. 4.6 shows the stability results for the BLIF method. We take a more strict standard to make sure all the RCS data from the “stable” simulations has no more than 20% relative error compared with the Mie series result. The result from CQ shows that the relative importance of near field integral accuracy to accomplish stability. The results from BLIF show the difficulty in achieving stability in dielectric computations. Yet with proper accuracy control, it can be rendered stable, even given the much larger time step length compared with the case of conducting sphere presented in the last chapter.

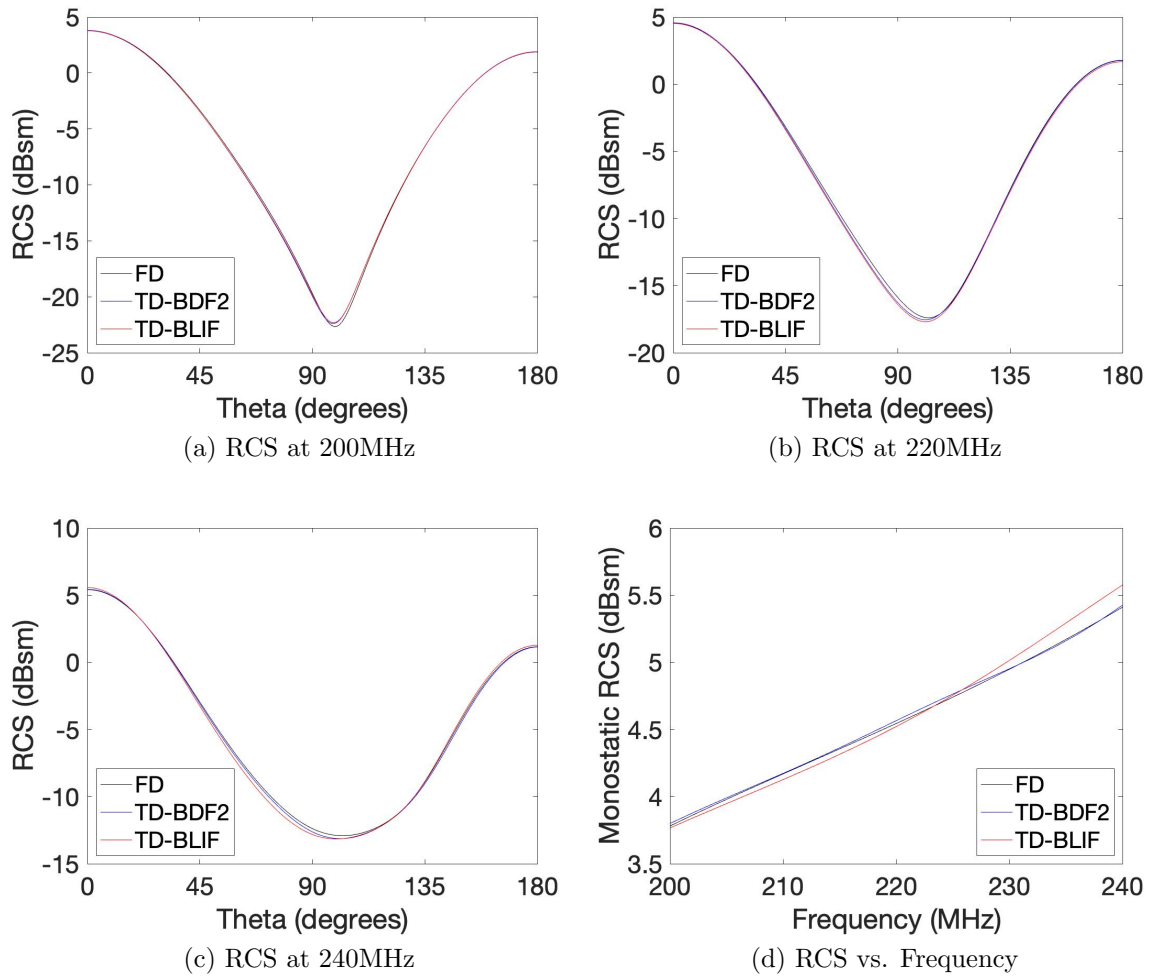
### 4.3 Dielectric Sphere with Conductor Core

The next example is a system of two concentric spheres. The inner sphere is of 0.5m radius. It was meshed into 72 perfect spherical triangular patches. The outer sphere is of 1.0m radius and was meshed into 128 perfect spherical triangular patches. The inner sphere is a perfect conductor and the outer sphere is a dielectric with  $\epsilon = 4.0$  and  $\mu = 1.0$ . The incident wave is of 40MHz nominal frequency band, 120MHz center frequency, and time delay to the origin of  $0.2\mu\text{s}$ . The spatial basis used first-order basis functions. The near field integration threshold was set to 0.86m. The testing rule was set to fifth-order, and the adaptive rules were built on one-point integrations. The

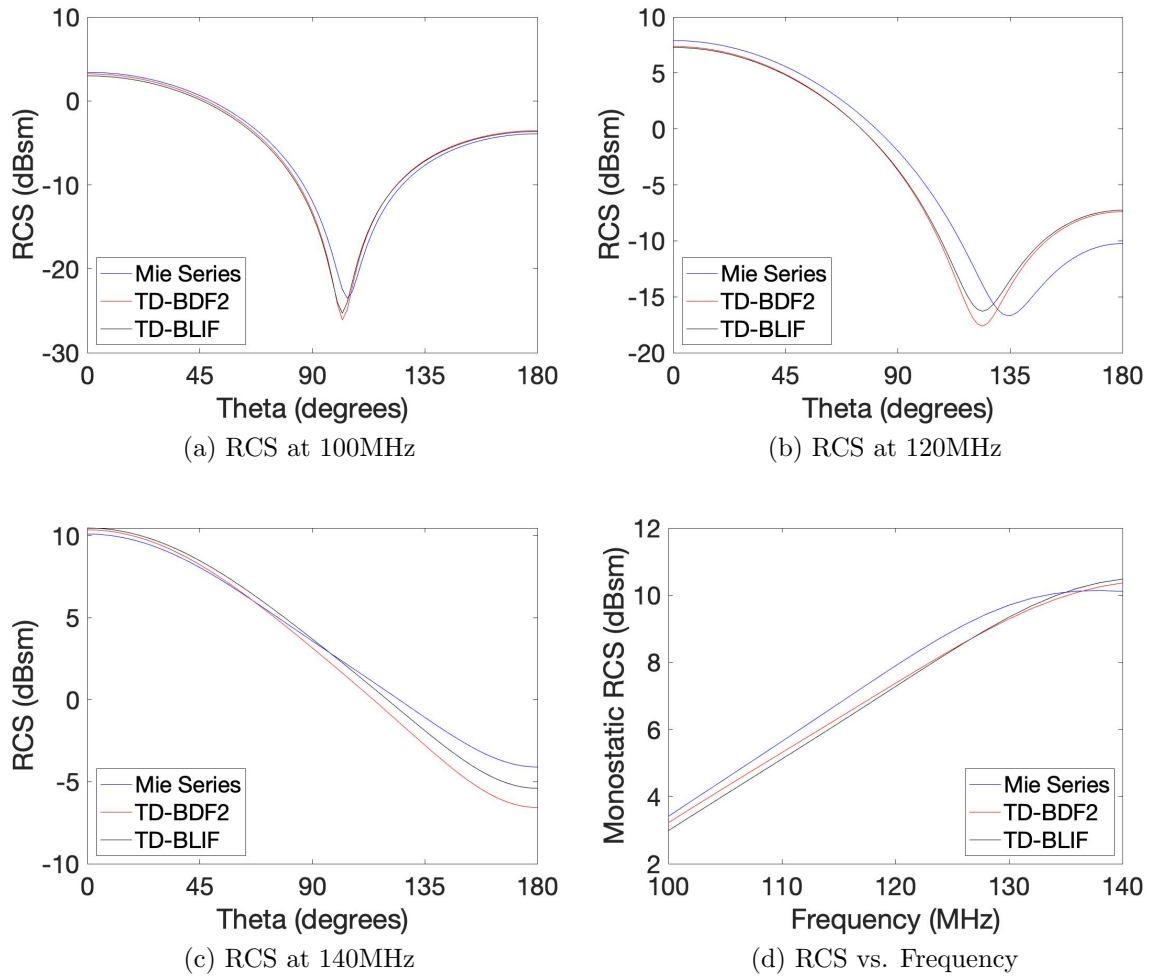
temporal discretization is consist of total 1400 time steps of 250ps each. The BLIF method parameters were  $N_{\text{past}} = 5$ ,  $N = 6$ , and  $f_0 = 200\text{MHz}$ .

Fig. 4.7 shows the RCS results at 41 frequencies located from 100 MHz to 140 MHz with 1 MHz increment. The relative error tolerance in the adaptive quadrature was 0.2 for both near field and far field integrals. The figure compares our time domain simulation results to the Mie series result. Both methods yielded very good results compared with the analytic solution. The BLIF method produced a more accurate result, especially in the low frequency range. Because the time step length is relatively long, the discrepancy in the high frequency range tends to be larger.

Fig. 4.8 shows the stability pattern for the CQ method. Fig. 4.9 shows the stability results for the BLIF method. Compared with the last case, the stability criterion here is stricter due to the more complicated interactions necessary to model this composite structure. Still, the results confirm that a more strict integral accuracy eventually ensures stability, and that the integration error tolerance needed for stability is not outrageously small.



**Figure 4.3:** Comparison of RCS results for a dielectric ogive. The bistatic RCS results at start point, middle point and the end point of the frequency range are shown in (a), (b) and (c). The monostatic RCS vs. frequency at elevation angle  $\theta = 0$  is shown in (d).



**Figure 4.4:** Comparison of RCS results of a dielectric sphere. The bistatic RCS results at start point, middle point and the end point of the frequency range are shown in (a), (b) and (c). The monostatic RCS vs. frequency at elevation angle  $\theta = 0$  is shown in (d).

		Far Field									
		10%	20%	30%	40%	50%	60%	70%	80%	150%	200%
Near Field	10%										
	20%										
	30%										
	40%										
	50%										
	60%										
	70%										
	100%										
	150%										
	200%										

**Figure 4.5:** Stability of the simulation versus integration accuracy for a homogeneous dielectric sphere for CQ.

		Far Tolerance								
		10%	20%	30%	40%	50%	60%	70%	100%	200%
Near Tolerance	10%									
	20%									
	30%									
	40%									
	50%									
	60%									
	70%									
	100%									
	200%									

**Figure 4.6:** Stability of the simulation versus integration accuracy for a homogeneous dielectric sphere for BLIF.

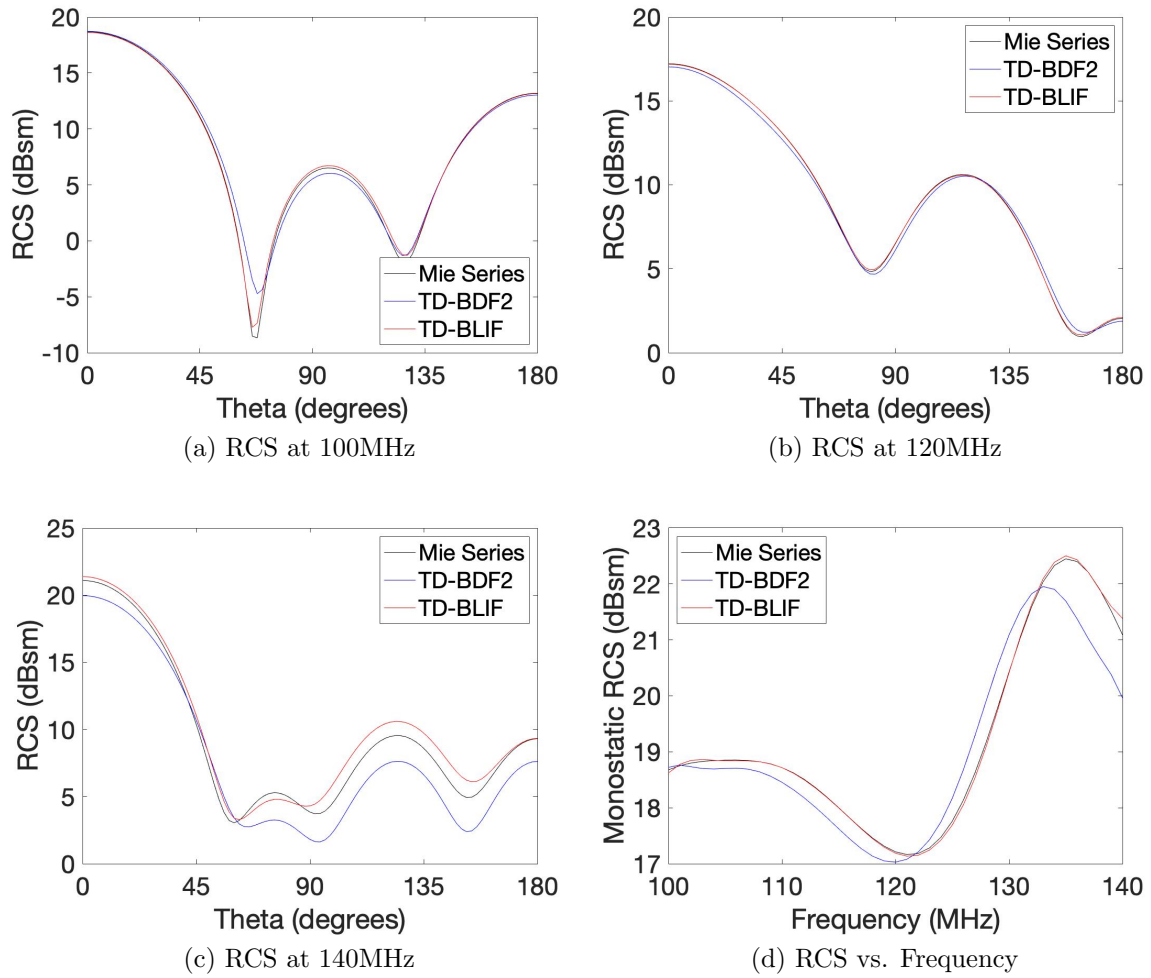


**Figure 4.7:** Comparison of RCS results of a dielectric sphere with a conductor core. The bistatic RCS results at start point, middle point and the end point of the frequency range are shown in (a), (b) and (c). The monostatic RCS vs. frequency at elevation angle  $\theta = 0$  is shown in (d).

		Far Field									
		10%	20%	30%	40%	50%	60%	70%	80%	150%	200%
Near Field	10%										
	20%										
	30%										
	40%										
	50%										
	60%										
	70%										
	80%										
	150%										
	200%										

**Figure 4.8:** Stability of the simulation versus integration accuracy for a dielectric sphere with a perfect conducting core for CQ.

		Far Tolerance								
		10%	20%	30%	40%	50%	60%	70%	100%	200%
Near Tolerance	10%									
	20%									
	30%									
	40%									
	50%									
	60%									
	70%									
	100%									
	200%									

**Figure 4.9:** Stability of the simulation versus integration accuracy for a dielectric sphere with a perfect conducting core for BLIF.

## Chapter 5

### CONCLUSION

This dissertation examined the relationship between the numerical integral accuracy and the stability of TDIEs. Two totally different TDIE solution methods, CQ and BLIF, were used to simulate different kinds of objects, including both perfectly conducting objects and dielectric objects. For conducting objects, both open and closed structures were simulated. For large conducting objects, AIM was used to accelerate the computations. To introduce proper accuracy control, an adaptive quadrature technique was applied to the nonsingular basis function integrations. Under these conditions, stability can be achieved with integration rules in the cases where they previously failed [61].

The results of this experiment demonstrate that the inaccuracy of naive spatial integral computations may affect the stability of TDIE codes. The results show that higher accuracy improves stability, and that the concern is more profound in the near field than in the far field. That said, integral accuracy should not be conflated with integral order. Earlier versions of this work ran the same experiment with Gaussian integration rules of different orders, and resulted in nearly inexplicable stability charts.

In short, kernel element computation plays a key role governing the stability of TDIEs. More attention should be paid to this seemingly trivial detail in published work. This work will soon be extended to determine how integration accuracy affects other types of scattering computations, with similar results anticipated.

## BIBLIOGRAPHY

- [1] A. Anees and L. Angermann. Time domain finite element methods for maxwell's equations in three dimensions. In *2018 International Applied Computational Electromagnetics Society Symposium (ACES)*, 2018.
- [2] C. A. Balanis. *Advanced Engineering Electromagnetics*. Wiley: Second Edition, 2012.
- [3] C. L. Bennett. *A technique for computing approximate electromagnetic impulse response of conducting bodies*. PhD thesis, Purdue University, 1968.
- [4] C. L. Bennett and J. DeLorenzo. Short pulse response of radar targets. In *1969 Antennas and Propagation Society International Symposium*, 1969.
- [5] C. L. Bennett and H. Mieras. Transient scattering from conducting cylinders. *Radio Science*, 16(6):1231–1239, 1981.
- [6] C. L. Bennett and G. F. Ross. Time-domain electromagnetics and its applications. *Proceedings of the IEEE*, 66(3):299–318, 1978.
- [7] C. L. Bennett and W. L. Weeks. Transient scattering from conducting cylinders. *IEEE Transactions on Antennas and Propagation*, 18(5):627–633, 1970.
- [8] C. L. Bennett and W. L. Weeks. Shooting and bouncing rays: Calculating the rcs of an arbitrarily shaped cavity. *IEEE Transactions on Antennas and Propagation*, 37(2):194–205, 1989.
- [9] E. Bleszynski, M. Bleszynski, and T. Jaroszewicz. AIM: Adaptive integral method for solving large scale electromagnetic scattering and radiation problems. *Radio Science*, 31(5):1225–1251, 1996.
- [10] J. W. Brown and R. V. Churchill. *Complex Variables and Applications: Ninth Edition*. McGraw-Hill Education, 2014.
- [11] Y.-S. Chung, T. K. Sarkar, and B. H. Jung. Solution of a time-domain magnetic-field integral equation for arbitrarily closed conducting bodies using an unconditionally stable methodology. *Microwave and Optical Technology Letters*, 35(6):493–499, 2002.

- [12] G. G. Dahlquist. A special stability problem for linear multistep methods. *BIT Numerical Mathematics*, 3(1):27–43, 1963.
- [13] P. J. Davies. On the stability of time-marching schemes for the general surface electric-field integral equation. *IEEE Transactions on Antennas and Propagation*, AP-44(11):1467–1473, 1996.
- [14] M. G. Duffy. Quadrature over a pyramid or cube of integrands with a singularity at a vertex. *SIAM Journal on Numerical Analysis*, 19(6):1260–1262, 1982.
- [15] D. A. Dunavant. High degree efficient symmetrical Gaussian quadrature rules for the triangle. *International Journal for Numerical Methods in Engineering*, 21:1129–1148, 1985.
- [16] A.A. Ergin, B. Shanker, and E. Michielssen. The plane-wave time-domain algorithm for the fast analysis of transient wave phenomena. *IEEE Antennas and Propagation Magazine*, 41(4):39–52, 1999.
- [17] S. D. Gedney. *Introduction to the Finite-Difference Time-Domain (FDTD) Method for Electromagnetics*. Morgan & Claypool Publishers: First Edition, 2011.
- [18] W. C. Gibson. *The Method of Moments in Electromagnetics*. Chapman and Hall/CRC: Second Edition, 2014.
- [19] R. D. Graglia, D. R. Wilton, and A. F. Peterson. Higher order interpolatory vector bases for computational electromagnetics. *IEEE Transactions on Antennas and Propagation*, 45(3):329–342, 1997.
- [20] T. Ha-Duong. On retarded boundary integral equations and their discretization. In *Topics in Computational Wave Propagation: Direct and Inverse Problems*, pages 301–336. Springer-Verlag, Berlin, 2003.
- [21] R. F. Harrington. *Field Computation by Moment Methods*. New York, Macmillan, 1968.
- [22] Einar Hille. *Analytic Function Theory, Volume I*. American Mathematical Society: Second Edition, 2012.
- [23] A. Hrennikoff. Solution of problems of elasticity by the framework method. *Journal of applied mechanics*, 8(4):302–307, 1941.
- [24] C. Durix J. C. Bolomey and D. Lesselier. Time domain integral equation approach for inhomogeneous and dispersive slab problems. *IEEE Transactions on Antennas and Propagation*, 26(5):244–248, 1979.
- [25] Jian-Ming Jin. *The Finite Element Method in Electromagnetics*. Wiley-IEEE Press: Third Edition, 2014.

- [26] J. B. Keller. Geometrical theory of diffraction. *Journal of the Optical Society of America*, 52(2):116–130, 1962.
- [27] E. M. Kennaugh and W. L. Weeks. Transient and impulse response approximation. *Proceedings of the IEEE*, 53(8):893–901, 1965.
- [28] David Kincaid and Ward Cheney. *Numerical Analysis: Mathematics of Scientific Computing*. American Mathematical Society, 2002.
- [29] J. Knab. Interpolation of band-limited functions using the approximate prolate series. *IEEE Transactions on Information Theory*, 25(6):717–720, 1979.
- [30] B. P. Lathi. *Linear Signals and Systems, Second Edition*. Oxford University Press, 2004.
- [31] J. Li, P. Monk, and D. S. Weile. Time domain integral equation methods in computational electromagnetism. In A. Bermúdez de Castro and A. Valli, editors, *Computational electromagnetism*. Springer International Publishing, 2014.
- [32] G. Manara, A. Monorchio, and R. Reggiannini. A space-time discretization criterion for a stable time-marching solution of the electric field integral equation. *IEEE Transactions on Antennas and Propagation*, AP-45(3):527–532, 1997.
- [33] E. K. Miller and J. A. Landt. Direct time-domain techniques for transient radiation and scattering from wires. *Proceedings of the IEEE*, 68(11):1396–1423, 1980.
- [34] P. Monk and E. Süli. Error estimates for yee’s method on non-uniform grids. *IEEE Transactions on Magnetism*, 30(5):3200–3203, 1994.
- [35] T. Namiki. 3-d ADI-FDTD method-unconditionally stable time-domain algorithm for solving full vector Maxwell’s equations. *IEEE Transactions on Microwave Theory and Techniques*, 48(10):1743–1748, 2000.
- [36] A. V. Oppenheim and R. W. Schaffer. *Discrete-time signal processing*. Prentice-Hall, Inc, 1989.
- [37] A. F. Peterson, S. L. Ray, and R. Mitra. *Computational Methods for Electromagnetics*. IEEE Press, 1997.
- [38] H. C. Pocklington. Electrical oscillations in wires. *Proceedings of the Cambridge Philosophical Society*, 9:324–333, 1897.
- [39] A. J. Pray, N. V. Nair, and B. Shanker. Stability properties of the time domain electric field integral equation using a separable approximation for the convolution with the retarded potential. *IEEE Transactions on Antennas and Propagation*, 60(8):3772–3781, 2012.

- [40] W. H. Press, S. A. Teukolsky, W. T. Vetterling, and B. P. Flannery. *Numerical Recipes: The Art of Scientific Computing*. Cambridge University Press, 2007.
- [41] M. M. Rao, T. K. Sarkar, R. S. Adve, T. Anjali, and J. F. Callejon. Extrapolation of electromagnetic responses from conducting objects in time and frequency domains. *IEEE Transactions on Microwave Theory and Techniques*, 47(10):1964–1974, 1999.
- [42] S. M. Rao and T. K. Sarkar. An alternative version of the time-domain electric field integral equation for arbitrarily shaped conductors. *IEEE Transactions on Antennas and Propagation*, AP-41(6):831–834, 1993.
- [43] S. M. Rao and D. R. Wilton. Transient scattering by conducting surfaces of arbitrary shape. *IEEE Transactions on Antennas and Propagation*, AP-39(1):56–61, 1991.
- [44] S. M. Rao, D. R. Wilton, and A. W. Glisson. Electromagnetic scattering by surfaces of arbitrary shape. *IEEE Transactions on Antennas and Propagation*, AP-30(5):409–418, 1982.
- [45] J. Rheinstejn. Backscatter from spheres: A short pulse view. *IEEE Transactions on Antennas and Propagation*, Ap-16(5):89–97, 1968.
- [46] A. E. Ruehli. Equivalent circuit models for three-dimensional multiconductor systems. *IEEE Transactions on Microwave Theory and Techniques*, 22(3):216–221, 1974.
- [47] T. Rylander and Bibdeson A. Stable fem-fdtd hybrid method for maxwell’s equations. *Computer Physics Communications*, 125(1):75–82, 2000.
- [48] B. P. Rynne. Stability and convergence of time marching methods in scattering problems. *IMA Journal of Applied Mathematics*, 35(3):297–310, 1985.
- [49] B. P. Rynne. Instabilities in time marching methods for scattering problems. *Electromagnetics*, 6(2):129–144, 1986.
- [50] A. Sadigh and E. Arvas. Treating the instabilities in marching-on-in-time method from a different perspective. *IEEE Transactions on Antennas and Propagation*, AP-41(12):1695–1702, 1993.
- [51] E. Sayre and R. Harrington. Transient response of straight wire scatterers and antennas. In *1968 Antennas and Propagation Society International Symposium*, 1968.
- [52] J.-C. Nedelec T. Abboud and J. Volakis. Stable solution of the retarded potential equations. In *17th Annual Review of Progress in Applied Computational Electromagnetics*, 2001.

- [53] N. V. Kantartzis T. D. Tsiboukis. *Higher-order FDTD Schemes for Waveguides and Antenna Structures*. Morgan & Claypool Publishers: First Edition, 2006.
- [54] A. G. Tijhuis. Toward a stable marching-on-in-time method for two dimensional electromagnetic scattering problems. *Radio Science*, 19(5):1311–1317, 1984.
- [55] P. Ufimtsev. Approximate computation of the diffraction of plane electromagnetic waves at certain metal bodies (part i and ii). *Soviet physics: Technical physics*, 27:1708–1718, 1957.
- [56] D. A. Vechinski and S. M. Rao. A stable procedure to calculate the transient scattering by conducting surfaces of arbitrary shape. *IEEE Transactions on Antennas and Propagation*, AP-40(6):661–665, 1992.
- [57] S. P. Walker, M. J. Bluck, and I. Chatzis. The stability of integral equation time-domain scattering computations for three-dimensional scattering; similarities and differences between electrodynamic and elastodynamic computations. *International Journal of Numerical Modelling: Electronic Networks, Devices and Fields*, 15(5-6):459–474, 2002.
- [58] X. B. Wang and D. S. Weile. Implicit runge-kutta methods for the discretization of time domain integral equations. *IEEE Transactions on Antennas and Propagation*, AP-59(12):4651–4664, 2011.
- [59] X. B. Wang, R. A. Wildman, D. S. Weile, and P. Monk. A finite difference delay modeling approach to the discretization of the time domain integral equations of electromagnetics. *IEEE Transactions on Antennas and Propagation*, 56(8):2442–2452, 2008.
- [60] D. S. Weile, G. Pisharody, N.-W. Chen, B. Shanker, and E. Michielssen. A novel scheme for the solution of the time-domain integral equations of electromagnetics. *IEEE Transactions on Antennas and Propagation*, 51(1):283–295, 2004.
- [61] D. S. Weile, I. Uluer, J. Li, and D. A. Hopkins. Integration rules and experimental evidences for the stability of time domain integral equations. In *2017 International Applied Computational Electromagnetics Society Symposium (ACES)*, 2017.
- [62] D. S. Weile and X. B. Wang. Strong singularity reduction for curved patches for the integral equations of electromagnetics. *IEEE Antennas and Wireless Propagation Letters*, 8(1):1370–1373, 2009.
- [63] V. Weston. Pulse return from a sphere. *IRE Transactions on Antennas and Propagation*, 7(5):43–51, 1968.
- [64] R. S. Chen Y. Shi, M. Y. Xia and E. Michielssen. Stable electric field tdie solvers via quasi-exact evaluation of mot matrix elements. *IEEE Antennas and Propagation Magazine*, 59(2):574–585, 2011.

- [65] K. Yee. Numerical solution of initial boundary value problems involving maxwell's equations in isotropic media. *IEEE Transactions on Antennas and Propagation*, 14(3):302–307, 1966.
- [66] A. E. Yilmaz, D. S. Weile, J. Jin, and E. Michielssen. Fast analysis of transient scattering in lossy media. *IEEE Antennas and Wireless Propagation Letters*, 1(1):14–17, 2002.
- [67] A. C. Yucel and A. A. Ergin. Exact evaluation of retarded-time potential integrals for the rwg bases. *IEEE Antennas and Propagation Magazine*, 54(5):1496–1502, 2011.